THÈSE

En vue de l'obtention du

DOCTORAT DE L'UNIVERSITÉ DE TOULOUSE

Délivré par :

Institut National Polytechnique de Toulouse (INP Toulouse)

Discipline ou spécialité :

Génie Électrique

Présentée et soutenue par :

M. LUIGI FERRARO
le mercredi 3 mai 2017

Titre :

Design and control of inductive power transfer system for electric vehicle charging

---

Ecole doctorale :

Génie Electrique, Electronique, Télécommunications (GEET)

Unité de recherche :

Laboratoire Plasma et Conversion d'Energie (LAPLACE)

Directeur(s) de Thèse :

M. STEPHANE CAUX
M. DIEGO IANNUZZI

Rapporteurs :

M. GIORGIO SULLIGOI, UNIVERSITA DEGLI STUDI DI TRIESTE
M. GIUSEPPE TOMASSO, UNIVERSITA DEGLI STUDI DI CASSINO

Membre(s) du jury :

Mme ANNUNZIATA SANSEVERINO, UNIVERSITA DEGLI STUDI DI CASSINO, Président
M. DIEGO IANNUZZI, UNIV. DEGLI STUDI DI NAPOLI FEDERICO II, Membre
M. FILIPPO MENOLASCINA, UNIVERSITE EDIMBOURGH, Membre
M. LUIGI PIEGARI, POLITECNICO DE MILAN, Membre
M. STEPHANE CAUX, INP TOULOUSE, Membre

Università degli Studi di Napoli Federico II

Ph.D. THESIS in

Information Technology and Electrical Engineering

Design and Control of Inductive power Transfer System for Electric Vehicle Charging

Luigi Ferraro

Tutor: Prof. Diego Iannuzzi
Prof. Stephane Caux

XXIX Ciclo

Scuola Politecnica e delle Scienze di Base
Dipartimento di Ingegneria Elettrica e Tecnologie dell'Informazione
Université de Toulouse, LAPLACE, CNRS, INPT, UPS, France

INDEX

CHAPTER 1

SURVEY OF INDUCTION POWER TRANSFER

CHAPTER 2

PROPOSED INDUCTION POWER TRANSFER SYSTEM

CHAPTER 3

VALIDATION OF MATHEMATICAL MODEL

CHAPTER 4

CONTROL SYSTEM DESIGN

References

CHAPTER 5

IPT - Transfert de Puissance par Induction

Chapitre 1 (p1-36)

1.1 Introduction

Le transfert de puissance par induction (IPT-Inductive Power Transfert) est un système privilégié pour des transferts de puissance sans contact. Basé sur les lois d'Ampère et Faraday, le principe du transfert de puissance passe par la création d'un champ magnétique entre deux inducteurs proches. La densité de puissance, et du champ magnétique dépend de l'amplitude du courant parcourant le circuit principal (Supply-Primary- Emetteur), la fem induite aux bornes de la charge (Load-Secondary- Récepteur) dépend également de la fréquence de variation de ces courants. En 1891, déjà, Nikola Tesla a mis en pratique ce principe (Fig. 1-1) en ajoutant le principe de résonnance, mais le développement industriel a attendu la fin du 20e siècle avec l'accroissement des besoins, l'amélioration des matériaux et la meilleure utilisation de l'électronique de puissance commandée par de meilleurs interrupteurs électroniques.

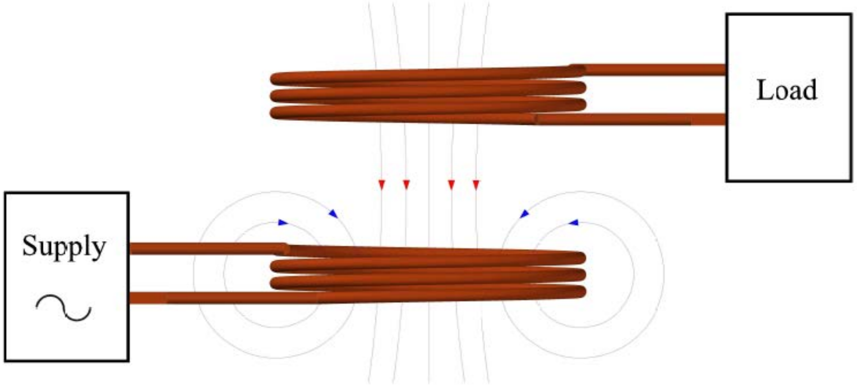

Fig. 1-1: Système IPT élémentaire

Ce dispositif présente des inductances mutuelles plus grandes que les inductances et un couplage magnétique 'faible' du fait de la largeur d'entrefer. La Fig. 1-2 présente l'ensemble du système de transfert par induction, pour lequel de gauche à droite nous trouvons les lignes d'alimentation par le réseau suivi d'un redresseur puis d'un convertisseur DC/AC permettant de contrôler l'amplitude et la fréquence des courants alimentant le circuit magnétique des deux bobines couplées. Du côté de la charge nous trouvons un convertisseur DC/DC pouvant contrôler les courants dans la charge.

L'alimentation produit donc des courants sinusoïdaux de haute fréquence [10-40] kHz, les deux inducteurs constituent un système de transformateur inductif couplé dépendant de la distance de l'entrefer et nous le verrons plus tard des désalignements entre les deux (face à face non idéal). Les inducteurs ne sont pas forcément identiques et leur forme et leur composition jouent sur l'efficacité du transfert ceci sera étudié par la suite. La charge étant une charge 'continue' un convertisseur DC/DC sera étudié pour obtenir la régulation de tension et le contrôle des courants de la charge.

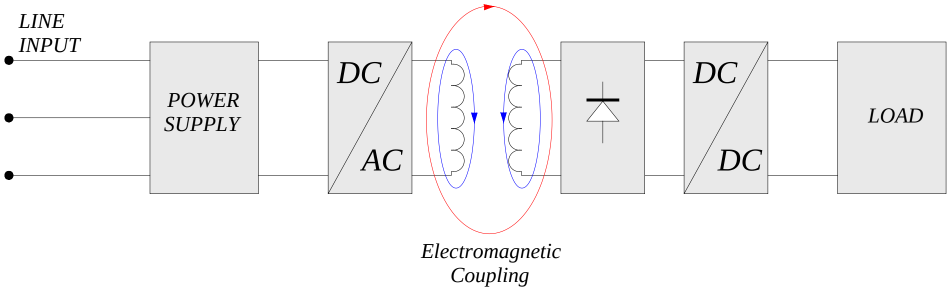

Fig. 1-2: Schéma fonctionnel d'un système IPT

L'ensemble de la conception et l'établissement du modèle électromagnétique choisi pour les inducteurs, la définition des convertisseurs et leurs circuits de compensation/résonnance, ainsi que les fonctions de transfert pour le pilotage de l'ensemble sont l'objet de cette thèse. L'objectif ici est d'obtenir un système de rechargement par induction (IPT) dynamique pour Véhicule Electrique (EV). Le design de la forme et des dimensions des inducteurs sera donc étudié en prenant en compte les contraintes d'embarquabilité dans le véhicule et de préservation de la santé humaine alentour (norme : The International Committee on Electromagnetic Safety (ICES) The International Commission on Non-ionizing Radiation Protection (ICNIRP)).

Sur la figure de principe suivante Fig. 1-3, nous pouvons considérer sous la route, une succession de circuits d'inducteurs 'primaires' et à bord du véhicule le système secondaire et la batterie à recharger. L'architecture sous la route peut être, soit un convertisseur multi niveau triphasé (MMC), soit une autre architecture d'électronique de puissance, l'alimentation peut se faire morceau par morceau successivement, par un simple système de détection du passage du véhicule. La difficulté ici est de gérer le fait que le véhicule passe à une certaine vitesse au-dessus des inducteurs primaires, et peut être sujet à des variations de hauteur (différentes gammes de véhicules) et/ou de mauvais alignement dans le plan sagittal et/ou latéral du véhicule en mouvement.

L'objectif final étant d'améliorer l'autonomie des véhicules électriques en rechargeant en cours de déplacement et donc en limitant les temps d'arrêt pour recharger la batterie.

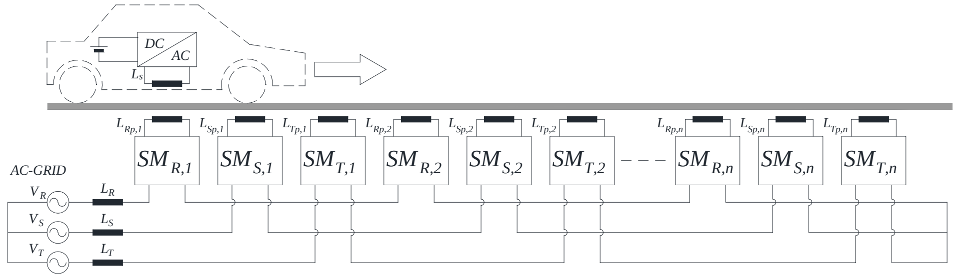

Fig. 1-3: Architecture MMC pour l'IPT dynamique, utilisant un circuit primaire monophasé

1.2 Technologies et choix liés à l'application

En fonction de l'application visée (guidage de véhicules (AGV), chauffage par induction (heat), recharge statique (dock) ou ici recharge dynamique), le circuit magnétique peut être en I, E, H voire en S ou autres. Après une étude bibliographique et l'étude spécifique pour cette application de recharge dynamique dans un véhicule (tenant compte également de norme électrique et de sécurité de santé humaine), nous avons choisi une structure primaire et secondaire particulière et vérifié d'une part par simulation le comportement électromagnétique et d'autre part obtenu une identification des paramètres inhérents pour l'étude et le contrôle de l'ensemble.

La forme des bobines primaire et secondaire influence le coefficient de couplage magnétique d'une part, et la répartition spatiale 3D du transfert du champ magnétique d'autre part. Nous chercherons ici, un fort coefficient pour un transfert de puissance plus efficace (bon facteur de qualité à la résonnance) et une répartition 'homogène' du champ car le secondaire (le véhicule) se déplacera dans ce champ créé.

Nous avons donc établie les équations correspondant à ce transfert électromagnétique (Ampère, Maxwell, Faraday) reliant les facteurs de puissance et de qualité aux diverses inductances et fréquence de fonctionnement.

Nous avons également à partir de la littérature, isolé des structures de convertisseur permettant le contrôle du courant et/ou tension au primaire et secondaire du système IPT tenant compte des structures de compensation (capacités série et/ou parallèle) requise au circuit primaire et secondaire. Les formules seront utilisées selon la structure et valeurs des inductances que nous développerons spécifiquement pour ce travail.

1.3 Structure magnétique

Les deux inducteurs doivent donc être relativement plats, compatibles entre eux pour un bon transfert de puissance à la même fréquence, et insensibles aux variations d'alignement voire de l'impédance de la charge tout en fonctionnant avec un entrefer relativement important (200mm).

Nous pouvons lister des circuits Circulaires Non Polarisés (trop sensible au centrage), des solénoïdes Polarisés (trop longs), des structures en Double D (DD) monté jointe ou en Quadrature (DDQ) des Bipolaires 'entrelacés'(BP) etc. Après l'analyse des formes de la distribution spatiale de la densité de puissance et le facteur de qualité de ces PAD nous avons retenu l'association des structures DD au primaire et BP au secondaire présentant une zone d'échange trois plus grande que les autres (à dimension identique) et une moindre sensibilité aux désalignements.

La conception à partir de barres de Ferrite (type N87 forme I taille 93mm x 28mm x 16mm), des fils de Litz (section 6,36mm^2, 810x0.1mm de résistance négligeable) pour mieux concentrer les flux magnétiques et minimiser les pertes lors du transfert de puissance (meilleur facteur de qualité Qi), nous a permis d'obtenir une construction d'inducteur comme ci-après en restant avec des courant de l'ordre de 23A et un entrefer de l'ordre de 200mm. La structure double D polarisée Fig. 1-4 (DD Pad), combine les avantages des structures 'circulaires' et celles à 'concentration', ne présentant notamment pas de flux nul au milieu de la structure magnétique (coil_{1A}-coil_{1B}=L_1 équivalent) et une bonne robustesse aux désalignements (faible variation d'une grande partie des paramètres caractéristiques).

Une structure carrée 'Pad Bipolaire' est choisie également pour mieux recevoir le transfert de puissance malgré les variations possible de positionnement du véhicule en x, y, z. Cependant ici cela implique l'utilisation de deux convertisseurs sur chacun des circuits magnétiques (Coil_2-L_2 et Coil_3-L_3) puis d'additionner les courants induits pour alimenter la charge.

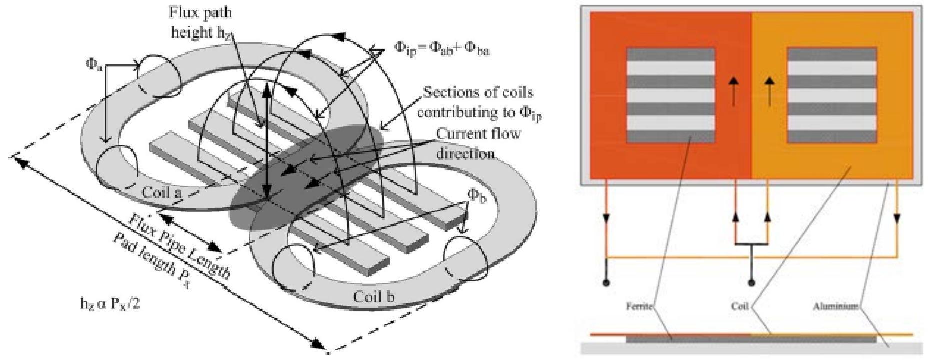

Fig. 1-4: DD pad

Nous avons également établi les structures de compensation avec des capacités accordées au primaire et au secondaire (circuit LCL série au primaire et secondaire - SS compensation). Pour obtenir l'ensemble de la structure suivante présentant de bonne propriété de maintien des tensions et d'insensibilité aux paramètres de la charge ainsi qu'aux désalignements et variations d'entre fer jouant peu sur les inductances et mutuelles.

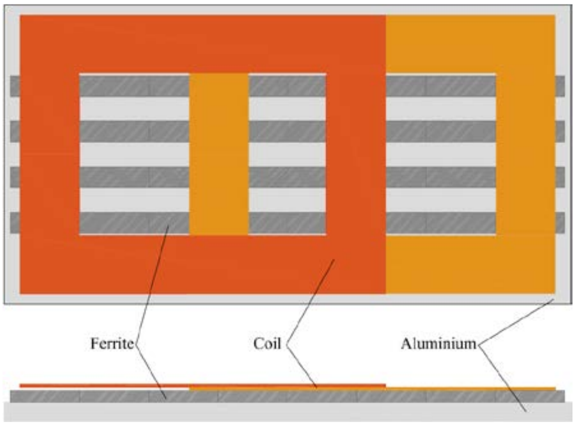

Fig. 1-5: BP pad

Chaiptre 2 (p37-74)

2.1 Système IPT retenu

L’alimentation principale est un redresseur suivi d’un pont en H et une capacité de sortie afin de produire des courants alternatifs carrés, cette source de courant (400 V) alimente un convertisseur résonant, le convertisseur DC/AC permet de créer le champs magnétique dans le premier circuit dans la route (5 à 50 kHz) en accord avec le circuit de compensation résonnant pour un maximum de transfert de puissance, le couplage électromagnétique permet le transfert de puissance sur les 2 parties en parallèle sous le châssis du véhicule, la puissance collectée permet la charge DC de la batterie à bord. Plutôt qu’une séparation primaire/route – secondaire/véhicule, une décomposition AC - DC s’impose.

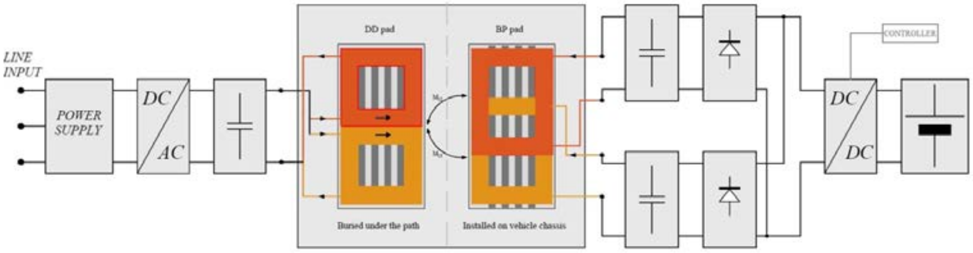

Fig. 2-1: Diagramme de blocs, de a DD (Double D primaire PAD) BP (Bipolar secondaire) PADs

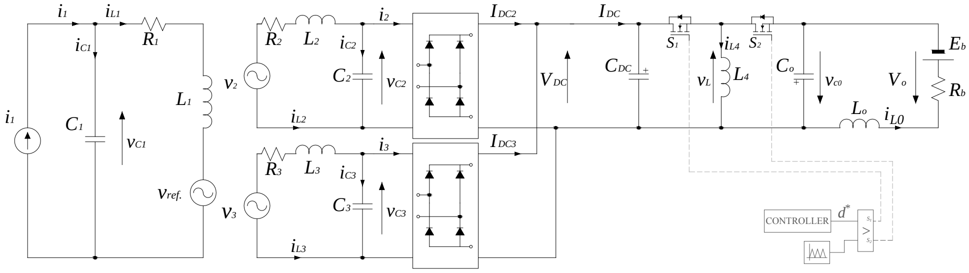

Fig. 2-2: Circuit équivalent IPT

2.2 Modélisation et Analyse

A l'aide des logiciels de calcul par élément fini Flux-FEM3D, et de simulation PSIM, nous avons modélisé, calculé puis extrait les caractéristiques électromagnétiques en fonction des dimensions et formes des inducteurs et établi le circuit électrique équivalent. Nous avons également validé les performances en fonction de la fréquence d'utilisation, les désalignements en x (+/-186, +/-140, +/-93, +/-46mm), y (+/-106, +/-80, +/-53, +/-26mm), z (150, 200, 250mm) et l'amplitude des courants.

L'analyse des différents tableaux de résultats et courbes 3D, nous montre les variations sur les valeurs des inductances propres L_1, L_2, L_3 et mutuelles et le coefficient de couplage k.

Sur notre structure, des variations peuvent se retrouver sur les inductances propres mais pour les mutuelles des effets croisés et des symétries vont nous aider à contrôler l'ensemble.

Le calcul de la capacité de compensation C_1 est fait d'une part avec les paramètres du primaire, d'autre part la capacité de compensation du secondaire C_2, avec ceux du secondaire à la fréquence de 20 kHz.

La source primaire est maintenant considérée comme une source de courant alternatif (I_1) de fréquence 20 kHz (AC side), le convertisseur DC/DC (DC side) fonctionnera avec un découpage de 1 kHz et un pilotage du rapport cyclique que nous développerons par la suite. Les deux bobines secondaires et leur circuit de compensation sont en parallèle pour que leur tension de sortie ($V_{c2}=V_{c3}=V_{dc}$) attaque après les deux redresseurs (non commandés ici) le convertisseur DC/DC qui alimente la charge DC (i_{DC}).

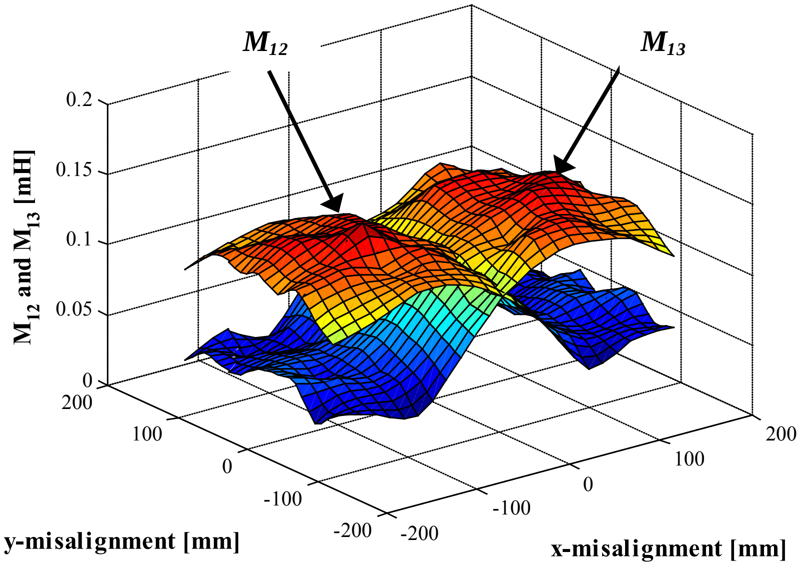

Fig. 2-3: Comparaison entre M_{12} and M_{13}

Après avoir défini les caractéristiques électromagnétiques, les dimensions et donc les valeurs des paramètres électriques équivalents, en identifiant les différentes boucles de tension et nœuds de courant, en séparant la partie AC de la partie DC, nous avons établi un modèle d'état (dimension 6 au primaire – AC et dimension 4 au secondaire – DC) afin de permettre l'étude des différentes fonctions de transfert sous Matlab entre les différentes variables courant/tension entrée/sortie etc.

$$\begin{cases} M_{13}\ddot{i}_{L1} + M_{23}\ddot{i}_{L2} + R_3\dot{i}_{L3} + L_3\ddot{i}_{L3} + \dfrac{i_{L2}}{C_{23}} + \dfrac{i_{L3}}{C_{23}} + \dfrac{i'_{DC}}{C_{23}} = 0 \\ M_{12}\ddot{i}_{L1} + R_2\dot{i}_{L2} + L_2\ddot{i}_{L2} + M_{32}\ddot{i}_{L3} + \dfrac{i_{L2}}{C_{23}} + \dfrac{i_{L3}}{C_{23}} + \dfrac{i'_{DC}}{C_{23}} = 0 \\ -R_1\dot{i}_{L1} - L_1\ddot{i}_{L1} - M_{21}\ddot{i}_{L2} - M_{31}\ddot{i}_{L3} - \dfrac{i_{L1}}{C_1} + \dfrac{i_1}{C_1} = 0 \end{cases} \qquad (2.1)$$

$$x = \begin{bmatrix} \dot{i}_{L1} \\ \ddot{i}_{L1} \\ \dot{i}_{L2} \\ \ddot{i}_{L2} \\ \dot{i}_{L3} \\ \ddot{i}_{L3} \end{bmatrix} \tag{2.2}$$

$$\begin{cases} I_{DC} + \hat{i}_{DC} - C_{DC}\dfrac{d\hat{v}_{DC}}{dt} + I_{L4}d + \hat{i}_{L4}D + I_{L4}D = 0 \\ L_4\dfrac{d\hat{i}_{L4}}{dt} - \hat{d}\cdot V_{DC} - D\cdot\hat{v}_{C2} + \hat{v}_{C0} - \hat{d}\cdot V_{C0} - D\cdot\hat{v}_{C0} - D\cdot V_{DC} - D\cdot V_{C0} + V_{C0} = 0 \\ L_0\dfrac{d\hat{i}_{L0}}{dt} - \hat{v}_{C0} + R_b\hat{i}_{L0} - V_{C0} + E_b + R_b I_{L0} = 0 \\ C_0\dfrac{d\hat{v}_{C0}}{dt} + \hat{i}_{L0} - \hat{i}_{L4} - \hat{i}_{L4}\cdot D + \hat{d}\cdot I_{L4} + I_{L4} - I_{L4}\cdot D + I_{L0} = 0 \end{cases} \tag{2.3}$$

$$\hat{x} = \begin{bmatrix} \hat{v}_{dc} \\ \hat{v}_{co} \\ \hat{i}_{L4} \\ \hat{i}_{Lo} \end{bmatrix} \tag{2.4}$$

Chapitre 3 (p75-86)

3.1 Simulations de l'ensemble du système IPT

Ceci pour également vérifier la stabilité a posteriori du système et sa sensibilité aux variations d'alignements et de fréquence. Comme présenté sur les diagrammes de Bode des figures suivantes. L'étude FEM3D permet l'identification de l'ensemble des paramètres donnés à la fois à la simulation circuit (PSIM) et pour les fonctions utilisées par Matlab (respectivement points * et courbes continues). Pour le rapport cyclique fixe D=0,6, I_{DC} entre 5 et 30A, fréquence entre 14 et 26 kHz et désalignement comme précédemment, nous analysons les résultats. En cas de désalignement, seule la partie AC est affectée et si les fréquences restent inférieures à la fréquence de résonnance les effets pourront être négligés.

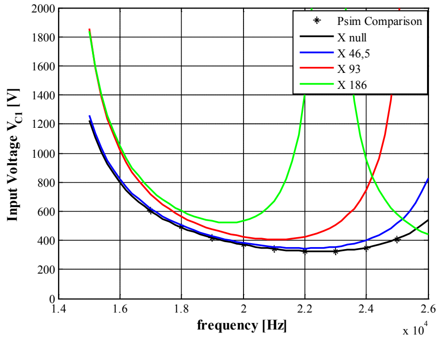

Fig. 3-1: Tension d'entrée V_{C1}

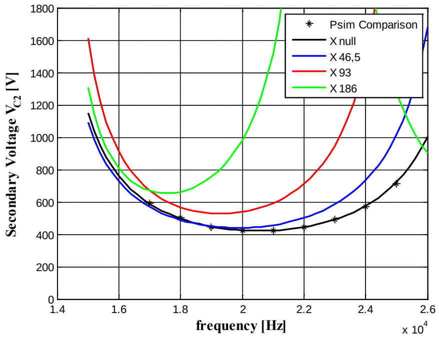

Fig. 3-2: Tension secondaire V_{C2}

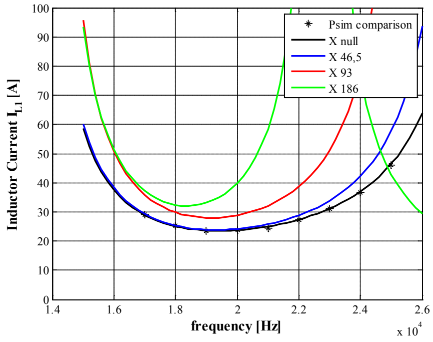

Fig. 3-3: Courant d'inducteur I_{L1}

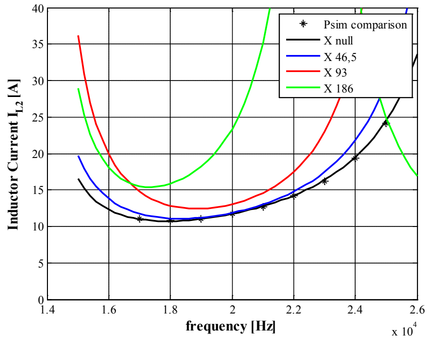

Fig. 3-4: Courant d'inducteur I_{L2}

Chapitre 4 (p87-111)

4.1 Modèle et recharge contrôlée de la batterie

Après une étude bibliographique sur les différents types et caractéristiques de batterie pour les véhicules électriques ainsi que sur les types de cycles/chargeurs possibles, nous avons considérés une batterie type Li-Ion (E_b=360V, 25A) dont le cycle de recharge est conseillé en deux phases. Une phase à courant constant Io (CC) pour laquelle la tension batterie s'accroit puis une phase à tension constante Vo (CV) pour compléter la recharge (20% restant environ jusqu'à obtenir 97%).

Le convertisseur DC/DC buck/boost peut donc gérer une tension Vo plus ou moins grande par rapport à V_{dc} (dimensionné pour rester autour d'un rapport cyclique D de 0.5) et contrôler le courant par contrôle des switchs (S1,S2). Deux boucles de courant sont nécessaire, l'une sur I_o, l'autre sur I_{L4}.

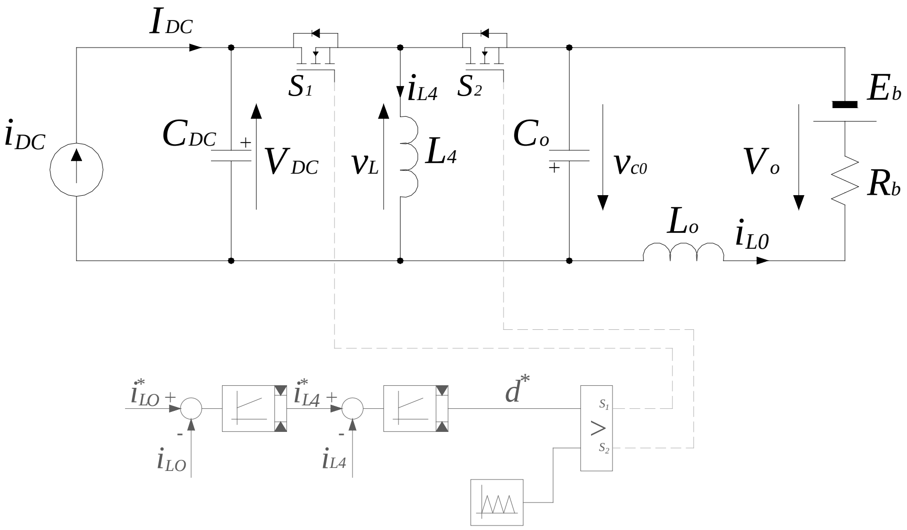

Fig. 4-1: Buck-boost circuit et contrôle PI en cascade

4.2 Synthèse du système IPT complet

L'étude d'un simple correcteur PI est basée sur le schéma bloc suivant ayant également permis d'étudier le point de fonctionnement assurant une bonne marge de phase du système et une bande passante suffisante. Une synthèse par la méthode de Ziegler-Nichols nous a permis d'obtenir rapidement les premiers résultats en boucle fermée, deux régulateurs en cascade sont nécessaire pour maintenir les performances en courant et en tension.

Nous avons identifié certaines conditions en lien avec les possibles désalignements pour maintenir la stabilité du transfert de puissance ne remettant pas en cause les conditions de l'application visée.

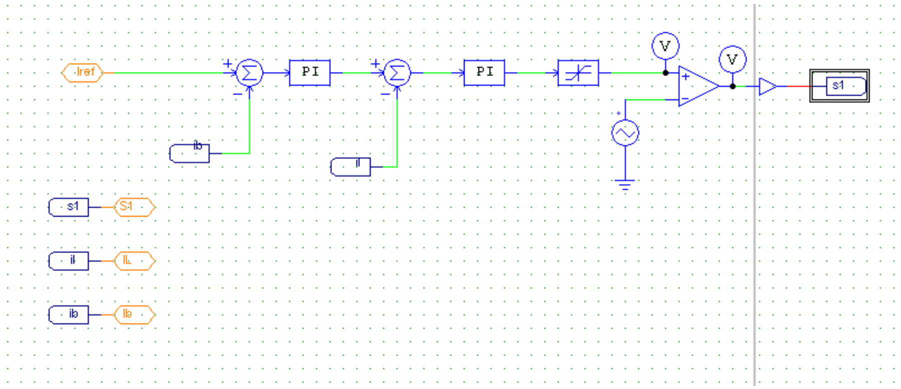

Fig. 4-2: PSIM Control circuit

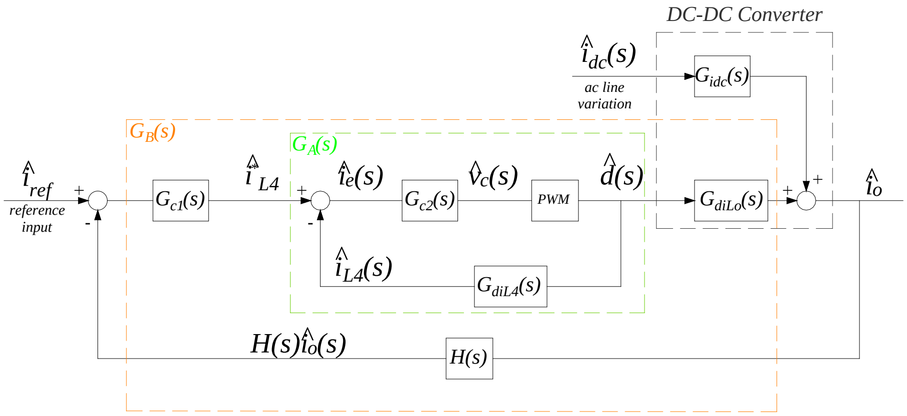

Fig. 4-3: Schéma blocs petit signal du système DC contrôlé

4.3 Résultats du contrôle complet

Ci-après nous retrouvons l'ensemble des parties modélisées sous PSIM correspondant à l'ensemble du système IPT à contrôler pour une bonne charge de la batterie dans ce dispositif de recharge par induction dynamique.

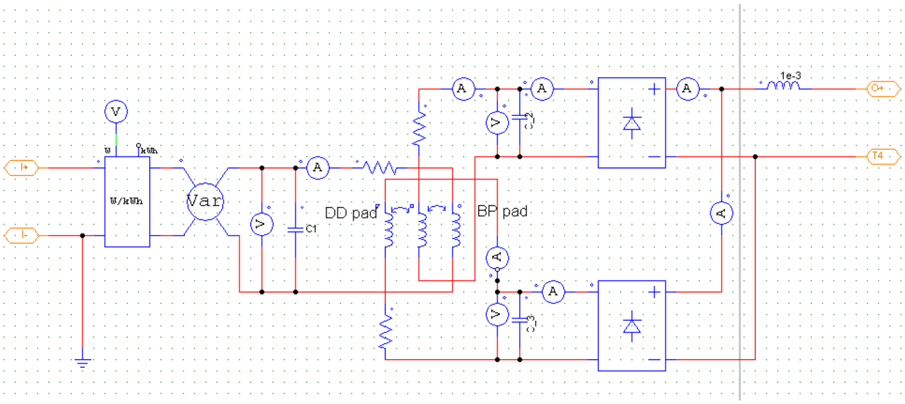

Fig. 4-4: PSIM Coupler circuit

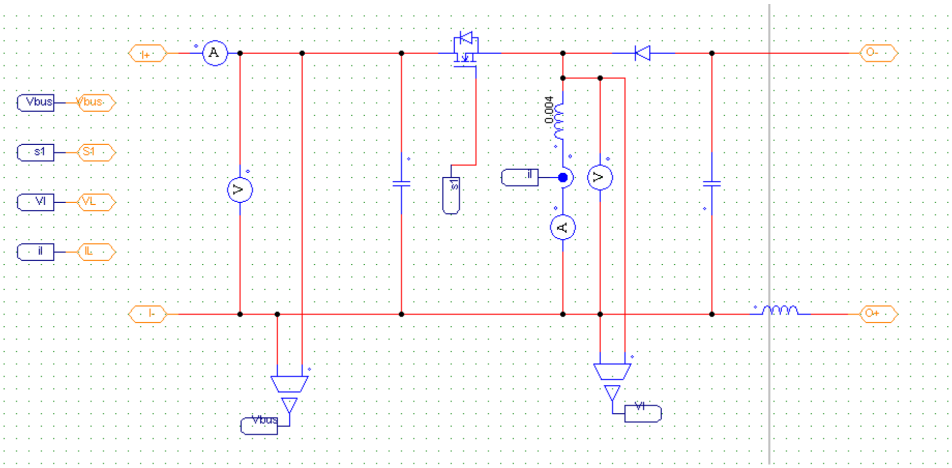

Fig. 4-5: PSIM Buck Boost circuit

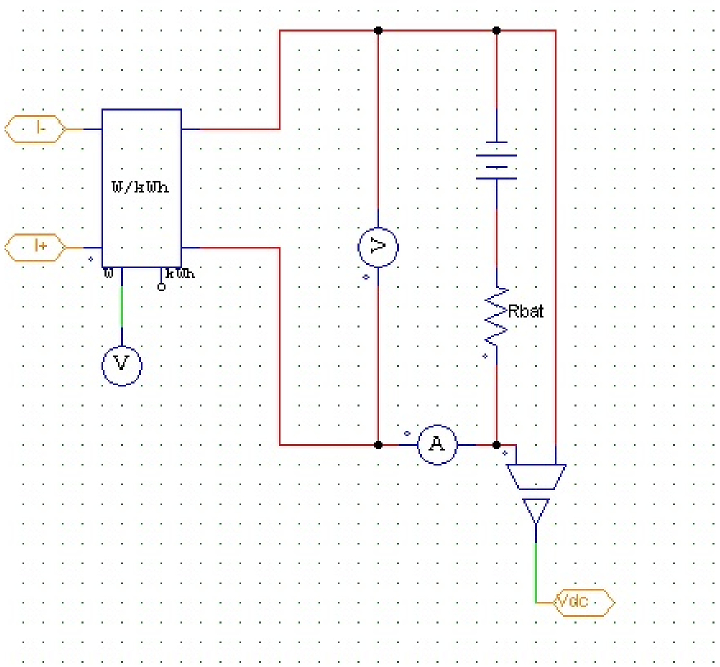

Fig. 4-6: PSIM Battery circuit

L'étude a été faite pour différents cas d'usage (valeurs différentes de I_o cf cas 2 des figures ci-après), différents désalignements etc. Par exemple, pour un découpage à 1 kHz,: V_{dc} entre [250-400]V, V_o de 360V donnant le rapport cyclique D entre 0.41 et 0.53 nous obtenons :

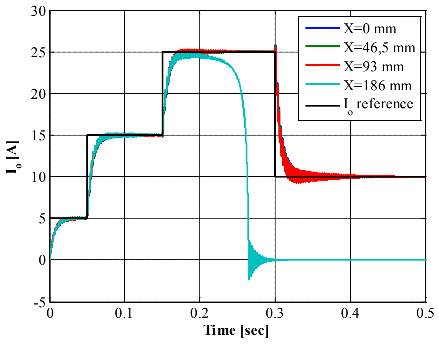

Fig. 4-7: Courant de sortie cas 2

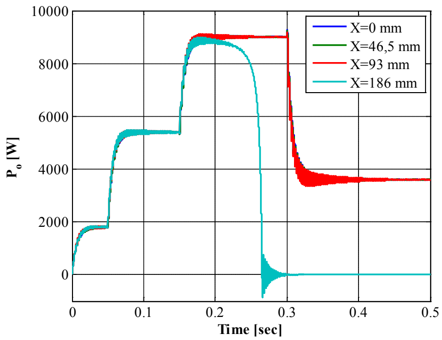

Fig. 4-8: Puissance de sortie cas 2

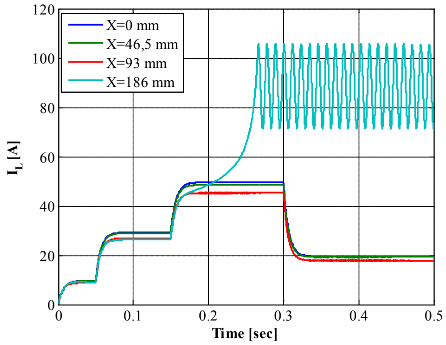

Fig. 4-9: Courant inducteur L4 case 2

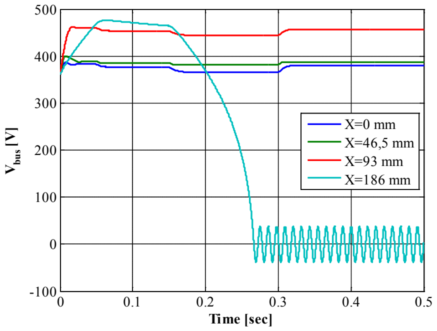

Fig. 4-10: Tension du bus DC case 2

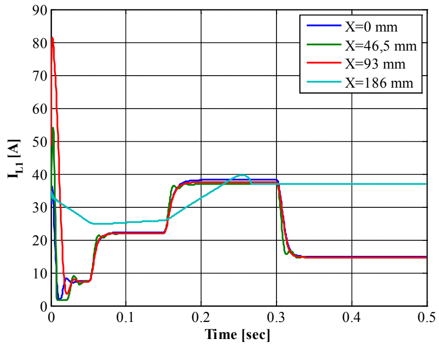

Fig. 4-11: Courant inducteur L1 case 2

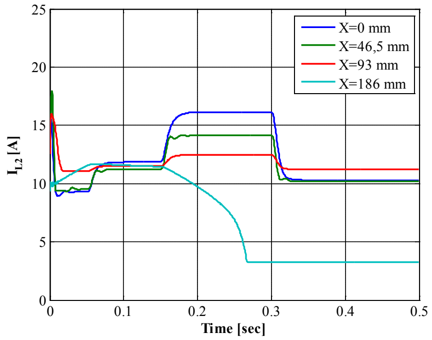

Fig. 4-12: Courant inducteur L2 case 2

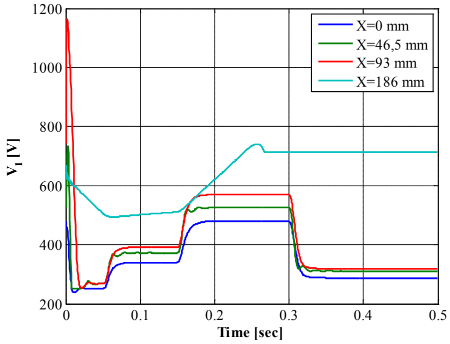

Fig. 4-13: Tension d'entrée cas 2

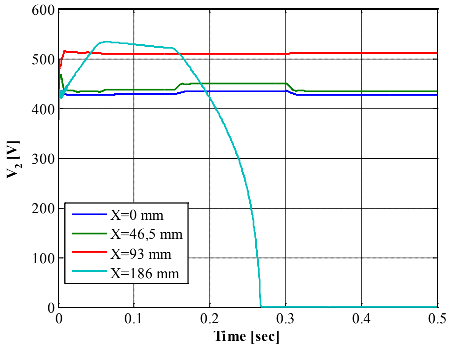

Fig. 4-14: Tension secondaire cas 2

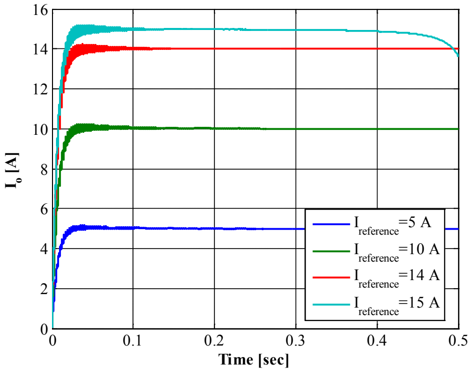

Fig. 4-15: Courant de sortie avec un désalignement x=186 mm

Un courant I_{ref} de plus de 14 A rend instable le contrôle, cela correspond à une limitation à un maximum de 5 kW. Cependant le comportement est efficace et correct même pour des désalignements en x de 93mm (moitié du dimensionnement choisi, 193 mm rend également instable mais ceci est 'normal' du fait que le véhicule n'est plus du tout au-dessus de l'inducteur primaire). L'étude est également faite sur les désalignements selon l'axe y.

Chapitre 5 (p112-113)

Conclusions générales : La thèse a montré la faisabilité d'un système de recharge par induction pour la recharge de la batterie d'un véhicule électrique en mouvement. Pour cela une étude bibliographique a permis d'isoler le dispositif adapté pour un bon transfert de puissance. Le design des inducteurs et l'extraction des paramètres ont permis de caractériser le comportement électrique de l'ensemble. L'exploitation des expressions mathématiques des parties alternatives, continues, et le coupleur ont permis l'analyse des Bodes en fonction des désalignements possibles. Une simulation complète PSIM, complétée par la synthèse d'un contrôleur du convertisseur de charge de la batterie montre les conditions de fonctionnement dans certaines limites principalement liées aux dimensions imposées par les dimensions du châssis et donc les désalignements à respecter.

Chapter 1

Survey of Induction Power Transfer

1.1 Introduction

1.1.1 Overview of Inductive Power Transfer System

Inductive Power Transfer IPT is the most widespread methods of wireless power transfer. IPT is applicable to many power levels and gap distances. Almost all wireless power transfer techniques use near field electromagnetics induction. Ampere's circuital law and Faraday's law of induction are the two principles on which is based the IPT systems. Ampere's law states that a magnetic field is produced around a conductor carrying electric current with a strength proportional to the current, whereas the Faraday's law states that an alternating magnetic field can induce an electromotive force in a conductor that is proportional to the magnetic field's strength and its rate of change. The first use of wireless power transfer has been possible thanks to Nikola Tesla around 1891. He invented the Tesla Coil, an electrical resonant transformer circuit, used to conduct innovative experiments among which the transmission of electrical energy without wires. Although the principle of function is at the base of modern solution, the diffusion of IPT system has been possible only at the end of 20th century because of component limitations at the time.

Fig. 1-1 illustrates how work an elementary IPT system. In the simplest form, an IPT system consists of two physically detached coils. When an alternated current flow in the first coil, called transmitter coil, a magnetic field is produced.

If the second coil, called receiver coil, is placed in close proximity with the transmitter, the alternating magnetic field will induce an electromotive force in the receiver's coil. A current will flow in the load if it is connected to the receiver coil. In these circumstances the power is transferred by induction from one coil to another without physical contact much like in a transformer but, unlike this latter, it has a low value of magnetic coupling. These system, in fact, have a leakage inductance higher than they magnetic inductance and therefore they are called loosely coupled system. Such power transfer is clean, unaffected by chemicals or dirt.

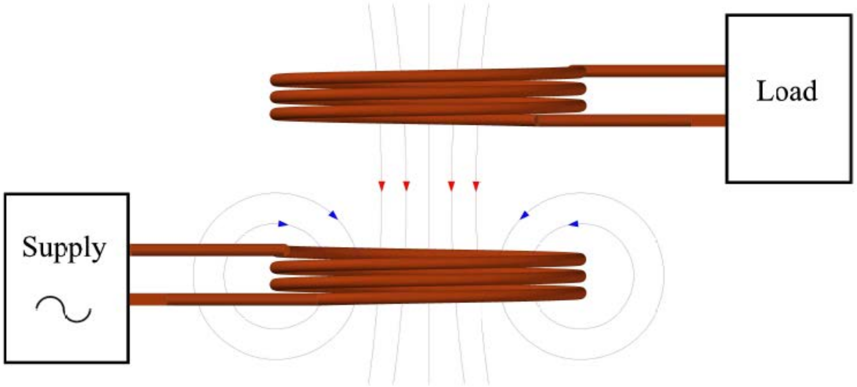

Fig. 1-1: Elementary IPT system

The Fig. 1-2 shows the block diagram of a typical IPT system. It can be noted that the system is splitted into two electric subsystems, magnetically coupled and supplied by means of high frequency power converter.

An IPT system comprises three main components: a power supply, almost two coupled coils, a rectifier and DC/DC converter. The power supply produce a sinusoidal current, with a usually frequency of 10-40 kHz, that flows in the transmitter coil. The power flows to the second subsystem by means of inductive link constituted by the two coupled coils. The two coils are not necessarily identical, they could have different dimensions and shapes. The rectifier may be required to transform the high frequency ac voltage into dc voltage if the load to be powered is a dc load. Moreover, an additional DC/DC converter can be required to provide a regulated input dc voltage to the load.

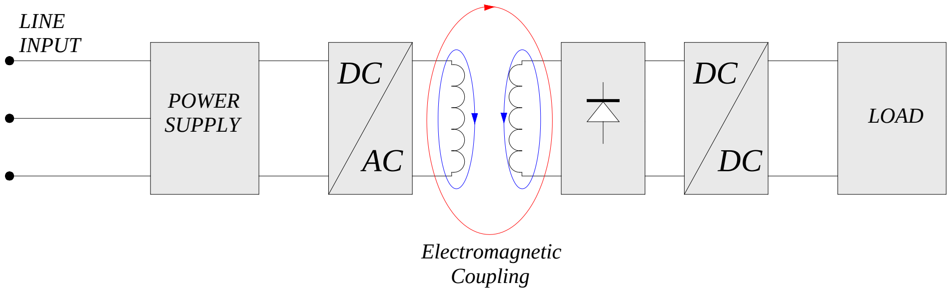

Fig. 1-2: Block diagram of a typical IPT system

1.1.2 Aims and Objectives of thesis

The aim of this thesis is design an IPT system, applied to the refill of batteries on board of the Electric Vehicles EV. The work has been done following the below objectives:

- Overview of the current state of EV's IPT technologies;
- Choose of a proper topology of system;
- Design of magnetic structure;
- Modelling of the system;
- Control of the system;

1.2 Induction Power Transfer Technology

1.2.1 Introduction

Due to oil rarefaction and gas emission restrictions, there is a growing interest all over the world for introducing electrical propulsion for ground transportation. Hybrid electrical vehicles are a first step for this energy transition, changing oil consumption in internal combustion engine to clean electric consumption in full electric vehicle. Nowadays hybrid and full electric vehicles suffer for some main drawback: their autonomy, the high initial cost (essentially battery costs), an excessive charging time not comparable to that of conventional vehicles and absence of a wide network of charging station. This project takes advantage of future trends on road architecture evolution including in the road possible induction and charging stations (ever existing in metro and tram systems). The vehicle autonomy can be extended reloading the battery during the trip. This concept has been referred to as dynamic charging, move and charge or roadway powered EVs. Dynamic charge can mitigate the high initial cost of plug in EVs by allowing to undersize the battery on board vehicle and could reduce the cost, the weight and fuel consumption of the vehicle. In addition, dynamic charging can provide a very effective utilization of the installed infrastructure, since a large number of vehicles use the same road segments that can be dynamic charge enabled. This is challenging and a complete design and model of the induction system should be established and local and global control made.

In this thesis, a complete study is presented from the road and truck inductors design. Parameter identification is achieved using electromagnetic flux software, thus equivalent electric circuit is deduced and also parameters variations are studied due to possible misalignment in case of such mobile devices more particular than reloading systems at fixed dock. At last, a state-space formulation is obtained representing the current, voltage and Induction Power Transfer behavior for analysis and control purposes.

1.2.2 Current Application and Technologies

The IPT technology is not based on recent concepts. The first person that has introduced the concept of wireless power transfer was Nikola Tesla around 1891 beginning from the Ampere and Faraday laws. He invented his famous Tesla coil. The system contains two loosely coupled and tuned resonant circuits: a primary and a secondary. Periodic spark gap discharges were used to short out the primary resonant circuit and initiate the power transfer. Tesla’s experiments demonstrate the majority of modern IPT design concept: a resonant circuit has needed to enhance the power transfer; a resonant converter has needed to supply the primary coil. The IPT was considered to be not viable for some time and against a background of unbelief it was not until the end of twentieth century that real commercial IPT system appeared.

An IPT system involves the coupling of two or more coils. When an alternated current flow in the first coil if the other coils are placed in close proximity with the first, the alternating magnetic field will induce an electromotive force in each coil. Such power transfer is without physical contact, clean, unaffected by chemicals or dirty and has the capacity to revolutionize many manufacturing processes. IPT finds application in factory automation, for instrumentation and electronic systems, in biomedical implants, in security systems, harsh environments and a lot of other applications where its unique features can be exploited. In fact, early commercial IPT systems found applications in car assembly plants where tolerance to paint and welding fumes was highly prized and also in transcutaneous medical devices while the dynamic powering of vehicles on monorails has spread to floor mounted automatic guided vehicles (AGV). Although the developments in this technology began with industrial applications, recently have shifted to designs that can meet the challenge of powering electric vehicles under both stationary and dynamic conditions.

In all such IPT systems thus far, energy has been coupled from a primary to a secondary across an air gap of significant but small proportions that stays relatively constant, even in the presence of movement. In manufacturing application, one primary circuit was able to drive a multitude of secondary circuits. Track guidance systems allow vehicles without drivers to move along a current carrying conductor. The inductive method has the advantage that it is not sensitive to oil, dirty, tire abrasion etc. Thus, their use has gained acceptance in harbors and industrial plants. Reference frequency and current as well as lateral separation and height from guide conductor can be selected from a large scope of variants. This type of systems are called automated guide vehicle. An AGV is a driverless transport system used for horizontal movement of material. They are most often used in industrial application to move materials around a manufacturing facility or warehouse. AGVs are employed in nearly every industry, including, pulp, paper, metals, newspaper and general manufacturing. The first AGV was brought to market in the 1950s and it was simply a tow truck that followed a wire in floor instead of a rail. The use of AGVs has grown enormously since their introduction. The primary coil on a monorail has the form of an elongated loop that is loosely coupled to a pickup coil on a vehicle and may transfer 1-10 kW of power across a 4-10 mm gap. With an AGV, the air gap may be 10-20 mm, and there may be a possible misalignment of similar magnitude.

An IPT system for the charging of the vehicles may be considered as an evolution of IPT system used in industrial application for the movement of products within an establishment. Differently of the AVG systems, for the EV charging of IPT systems, the trend is to use two concentrated coils, called pad, one buried in the roadway and the other mounted on the chassis of the vehicle.

1.2.3 Fundamental Principles of the IPTS

Modeling the IPT system is crucial in designing wireless power transfer system for EVs. Simplicity and the accuracy of the model are important. The modeling methodology needs to provide guide lines in the selection of system performance indices and design parameters.

A power supply takes power from a utility and energizes a primary loop or track to which pickup coils may be magnetically attached. In Fig. 1-3, is shown a typical scheme.

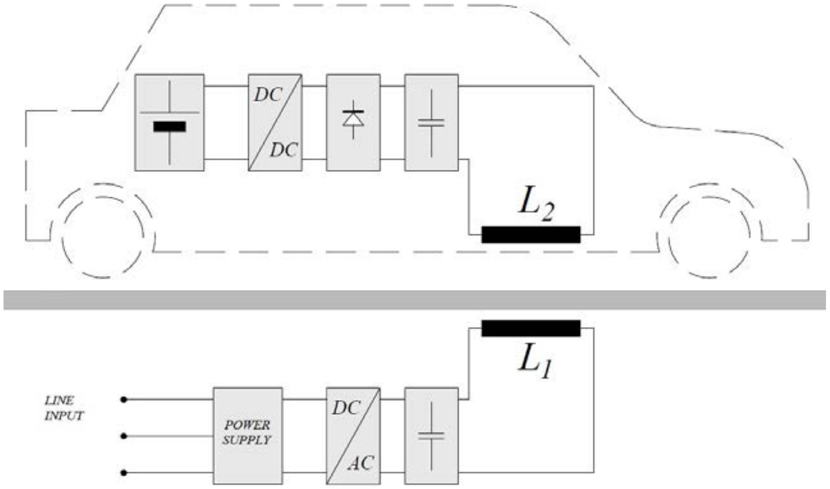

Fig. 1-3: Block diagram of a typical IPT system

In the simplest case, an IPT pickup consists of a coil of wire in close proximity to the track wires positioned to capture magnetic flux around the track conductor. Conceptually, this is similar to a transformer, although with a much lower magnetic coupling. As in transformer design, magnetic material such as ferrite is used to direct the magnetic flux and improve the coupling between the track and any pickups.

The IPTs are governed by Ampere’s law and Faraday’s law among four Maxwell equations, as shown in Fig. 1-4.

It can briefly explain as follows:

1) time varying magnetic flux is generated from the ac current of a power supply rail in accordance with Ampere’s law;
2) voltage is induced from the pickup coil, coupled with the power supply rail, in accordance with Faraday’s law;
3) power is wirelessly delivered through magnetic coupling, where capacitor banks are used to nullify inductive reactance.

The governing equations of IPTS for sinusoidal magnetic field, voltage and current are approximated as follows:

$$\nabla \times \mathbf{H} = \mathbf{J} \tag{1.1}$$

$$\nabla \times \mathbf{E} = -j\omega\mathbf{B} \tag{1.2}$$

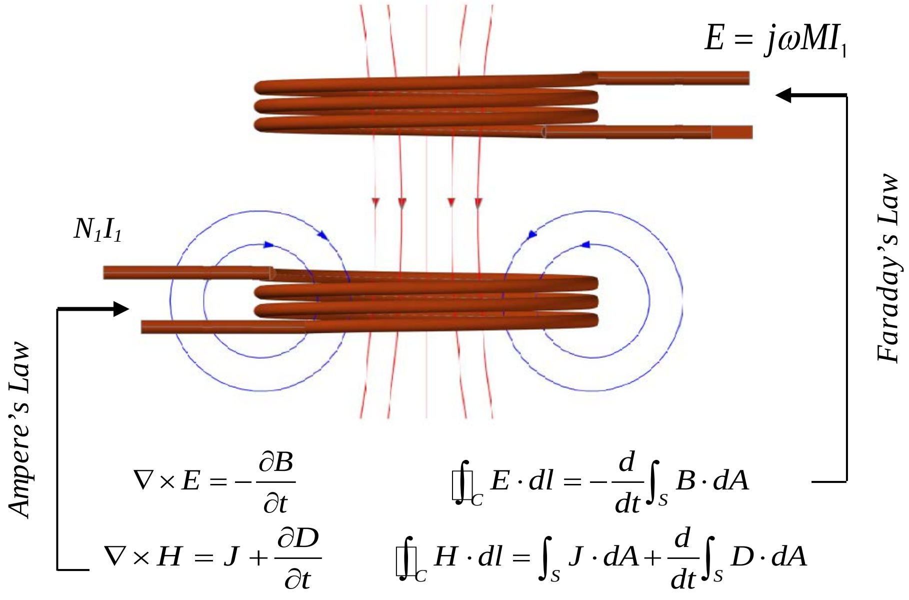

Fig. 1-4: Maxwell equations

In the development of a complex technology such as this it became impossible design and work with a circuit constructed of wire, ferrite, air gaps and electronics components so an electrical equivalent circuit had to invented as shown in Fig. 1-5.

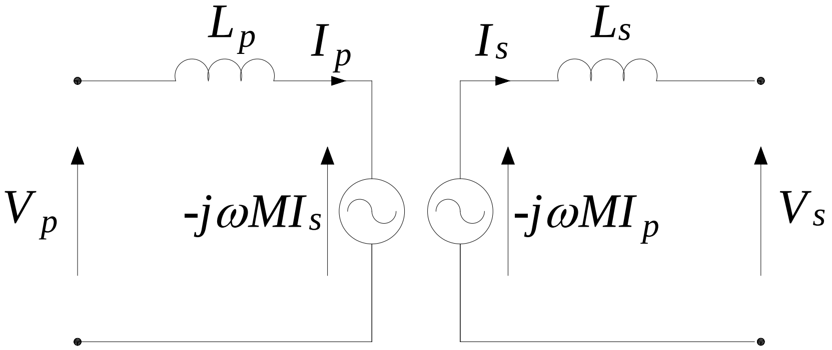

Fig. 1-5:Equivalent coupling circuit

The performance of an IPT pickup is primarily determined from two parameters 0: the open voltage circuit voltage induced in the pickup coil at frequency ω due to primary track current I_1, $V_{oc} = j\omega MI_1$ and its short circuit current $I_{sc} = MI_1/L_2$ which is the maximum current from V_{oc} limited by the impedance of the pickup coil inductance ωL_2. Here, M is the mutual inductance between the track and the pickup coil. From the first principles, the product of these two parameters is the maximum VA rating for the pickup called S_u and give a measure of how good the power coupling of any magnetic system is for a particular driving condition.

$$S_u = V_{oc} I_{sc} = \omega I_1^2 \frac{M^2}{L_2} \tag{1.3}$$

without compensation, the maximum power that can be drawn from a pickup is generally not sufficient. In order to improve the available power, the pickup inductor is compensated with capacitors such that it resonates at or near the frequency of the track.

The ac tuning causes a resonant current to flow in the tuned L_2C_2 circuit, which is boosted by Q_2, while the voltage V_c across the capacitor is similarly boosted by the circuit Q_2. Here, Q_2 is the tuned quality factor of a secondary system, which is determinate by the output load or controlled by controlling the output voltage current.

Thus, for the parallel tuned regulator, this tuning enables the output voltage seen by the regulator to be increased in proportion to the circuit's resonant *Q*, while for a series tuned pickup, the output current is boosted by *Q*. In either case, the maximum power that the system can transfer into a load is thereby improved by Q_2 resulting in

$$P_{out} = S_u Q_2 = \omega I_1^2 \frac{M^2}{L_2} Q_2 \tag{1.4}$$

This power equation is valid for all manner of IPT systems but some minor adjustments may occur in track based systems driven from a current source when the inductance L_1 can be very large. Pickups in track systems are usually in a close relationship with the track and can partially enclose the track inductor giving high k values (where $k = M \big/ \sqrt{L_1 L_2}$ is the magnetic coupling factor) that are not achievable with floor mounted system such as AGVs or moving robots. Nonetheless, regardless of the value of k the analysis can proceed in the same way. The magnetic coupling coefficient is a very important parameter determining the performance of IPT system. In fact, the output power of an IPT system can be easily quantified as a function of the magnetic coupling coefficient k by means of the following relation:

$$P_{out} = \omega I_1^2 \frac{M^2}{L_2} Q_2 = \omega L_1 I_1 \cdot I_1 \frac{M^2}{L_1 L_2} Q_2 = V_1 I_1 \cdot k^2 \cdot Q_2 \tag{1.5}$$

In this form, the power transfer can be seen as the input VA multiplied by the magnetic coupling factor k^2, multiplied by the electrical quality factor of the loaded secondary circuit Q_2 and is not dependent on ω that is now included in the voltage at the input of L_1.

Following (1.5), the power transferred by an IPT system can be improved by increasing any of ω, M, I_1 or Q_2. There are, however, advantages and disadvantages with all of these possibilities. Increasing the power by increasing the frequency is something of an illusion and may not bring about the benefits expected. The system is clearly frequency sensitive but it is not a simple dependency as it appears here. Increasing the mutual coupling is without doubt the best solution as it involves making the magnetics better and as this is a magnetic coupling it is really the ideal approach, but there are limits in terms of magnetic coupler size and volume of material that must be considered for each application. Increasing the excitation current is a forced solution that usually leads to a lower efficiency. It will give more power, but it puts more stress on all the components in the process. Increasing Q_2 of the secondary electrical circuit is a good solution but as described below this increases the VA of the secondary and narrows its bandwidth (much in the same sense as tuning a radio receiver). It cannot be carried to excess or the system becomes too difficult to tune and keep on tune over time (because of aging effects of capacitors) or in uncontrolled environments (where the presence of materials or movement can shift the inductance value).

1.2.4 Components of an IPT System

A simple IPT system is shown in Fig. 1-3.

It comprises of the following:

1) a power supply that takes electric power from a utility or a battery;
2) an elongate track that is driven by the power supply whereby current in the track causes a magnetic field that follows the track;
3) pickups on or along the track that intercept some of the magnetic field and convert that intercepted field to controlled electricity;
4) electrical loads that may be driven by that electricity.

All of these aspects are important but some are essentially self-evident. There are a very large number of power supply circuits that may be used in an IPT system but all of them achieve the same outputs with different output frequency, efficiency, and reliability. However, modern IPT supplies generally

favor current controlled supplies with unity power factor and with a controlled frequency [2]. The frequency must be system wide but other attributes will vary with cost and availability. The track usually uses high frequency Litz wire to support the magnetic field.

A significant effort in the design of IPT systems is to increase k by improving the magnetic designs.

1.2.5 IPT Power Supply

A DC-AC inverter is a common solution to generate a high frequency track current for an IPT system. Often a front-end low frequency mains power is rectified into a DC power source and then inverted to the required high frequency AC track current. Energy storage element, such as large DC capacitor, are used to link the rectifier and the inverter. IPT power supplies may be voltage sourced or current sourced, and may be a full bridge or half bridge configuration. Fig. 1-6 shows circuits for voltage sourced inverters for both full bridge or half bridge and Fig. 1-7 shows circuit for current sourced inverters again for both full bridge and half bridge. It should be noted that no one circuit is fundamentally better or worse than any other circuit and there is a lot of designer choice but that said some of the circuits do have some features that are particularly attractive.

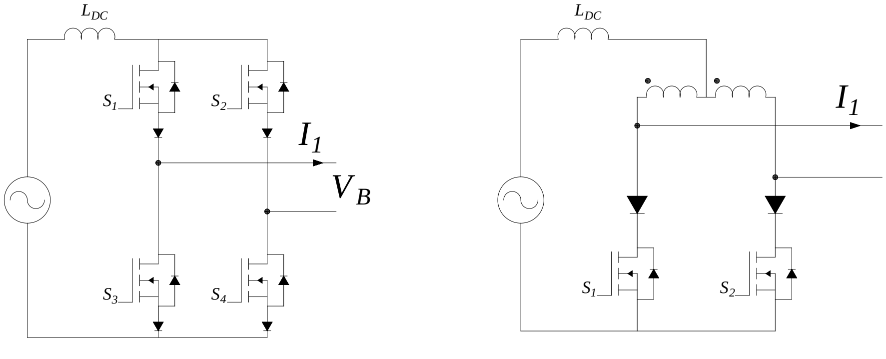

(a) (b)

Fig. 1-6: Voltage source inverters: (a) full bridge, (b) half bridge

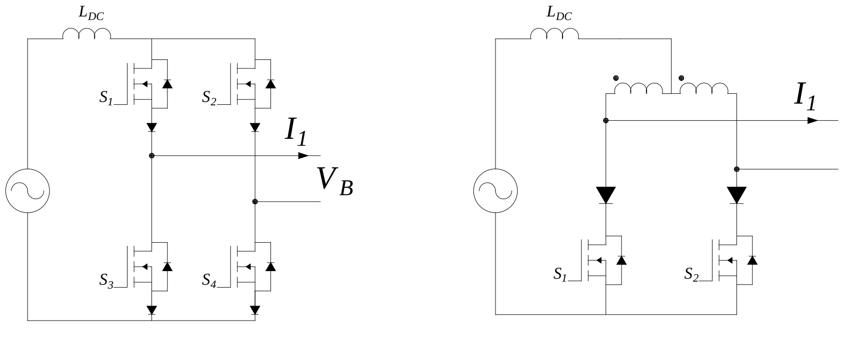

(a) (b)

Fig. 1-7: Current source inverters: (a) full bridge, (b) half bridge

When used in an IPT system the track requires a constant current along its full length so that pickups at any point along the track operate under their design conditions. In principle, this may be achieved using one of the circuits in Fig.

1-8 where Fig. 1-8 (a) is parallel tuned and can operate with an inverter supplying an output voltage and virtually no other control, while Fig. 1-8 (b) is series tuned and the inverter itself must supply all of the output current and will need some form of controller.

At this point there is a major difference between these alternatives: for a track current of 100 A say the inverter of Fig. 1-8 (a) only has to supply the real load current which is typically a lot less than the 100 A while the inverter of Fig. 1-8 (b) must supply the whole of the 100 A meaning that there is always 100 A in the switches of the inverter and this circuit is therefore likely to be less efficient especially on lighter loads. Today there is another option – shown in Fig. 1-8 (c).

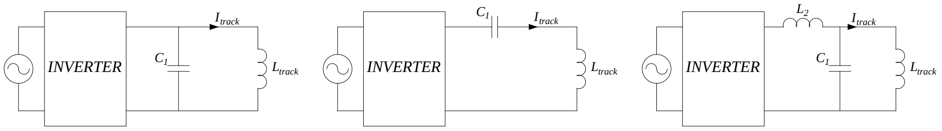

(a) (b) (c)

Fig. 1-8: Fixed frequency supplies: (a) parallel tuned; (b) series tuned; (c) LCL compensation using extra inductor

Here an impedance converting network (an ICN) called here an LCL-T circuit is placed between the inverter and the parallel tuned load of Fig. 1-8 (a) to give a constant current in the track provided that the inverter outputs a constant voltage. So Fig. 1-8 (a) and Fig. 1-8 (c) give the same current in the track but the difference is that the power factor of the inverter current in Fig. 1-8 (a) may be poor so that the inverter will have to work harder whereas the power factor with Fig. 1-8 (c) is perfect and the inverter sees a resistive load with perfect tuning.

Modern industrial IPT power supplies have a level of performance that would have seemed impossible 3-5 years ago. Today power supplies are modular so that the economy of scale can be brought to larger units. An attractive solution is to supply the IPT system by means of a Modular Multilevel Converter MMC. Its basic architecture is shown in Fig. 1-9.

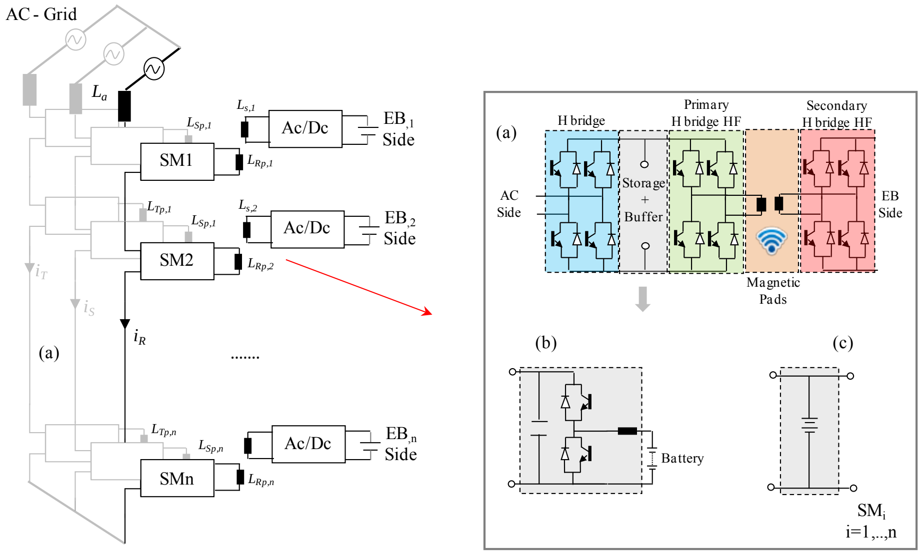

Fig. 1-9: a) Modular Multilevel Converter architecture; b) structure of a sub-module

Usually, each converter leg includes freely chosen number *n* of identical sub-modules. The main advantages, that make very attractive this circuit topology, are: a modular structure able to be adapted to different voltage and power levels; a redundant operation that performs high availability values and robust failure management (i.e. a sub-module can be short-circuited, while the corresponding leg can still operate with one voltage level less, but without any further restriction).

Obviously, the converter architecture should be adopted to the used primary pad. Using this topology of converter to dynamic charge, when the primary pad is single-phase, the architecture is shown in Fig. 1-10. Once, the path is defined and also its length is established, then the primary pads are buried sequentially along the path by leaving a proper gap among them. Each primary coil pad is fed by a single sub-module of the. Moreover, the pads order must be as reported in Fig. 1-10 (e.g. $L_{Rp,i}$, $L_{Sp,i}$, $L_{Tp,i}$, with $i=1,\ldots,n$). by detecting the vehicle position versus path [3], only the pads covered by the vehicle are energized. The total number of primary pads must be multiple of three, in order to have the same number of sub-module for each leg phase.

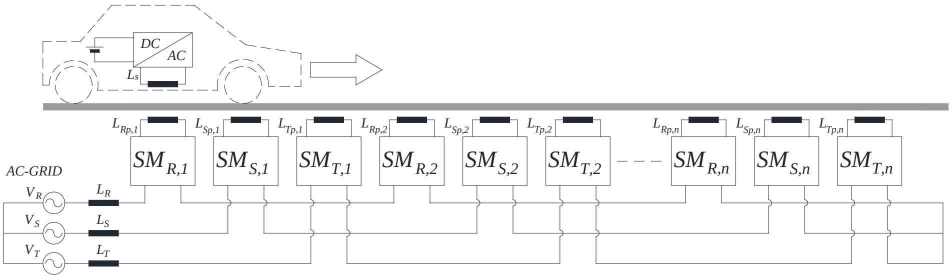

Fig. 1-10: MMC architecture for dynamic IPT using single-phase primary pad

Furthermore, if the primary pad is a tripolar pad, the converter architecture is shown in Fig. 1-11. The tripolar pads are buried sequentially along the path by leaving a proper gap among them. Each pad consists of three coils fed by three subsequent sub-modules of the same phase leg. Thus, the series of three primary tripolar pads are fed by three different phases. The total number of primary pads must be multiple of three, in order to evenly the load of each phase.

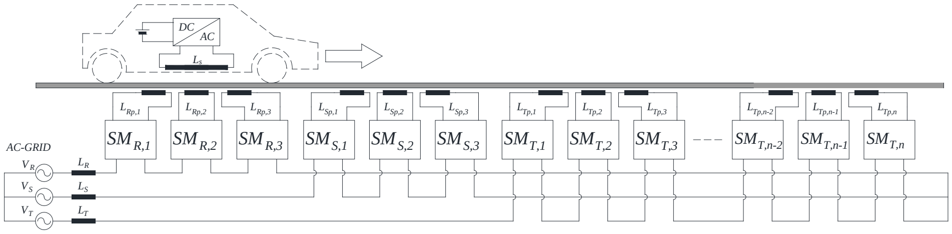

Fig. 1-11: MMC architecture for dynamic IPT using three-phase primary pad

1.2.6 Pickup Regulator

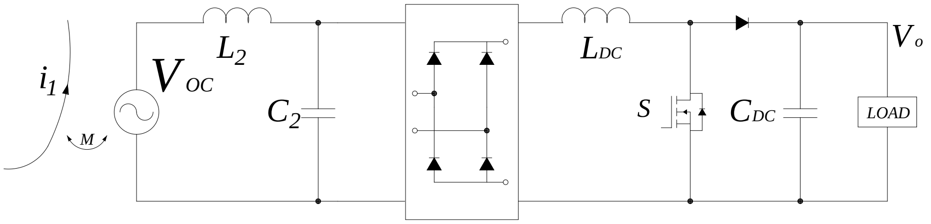

Fig. 1-12:Pickup equivalent circuit

In order to refill the battery mounted on board of the electric vehicle, it is necessary convert the alternating AC current to the direct DC current by means of a rectifier converter [4]. The output voltage of the secondary pad depends from several factors, among which the coupling factor has a strong impact. Obtain a proper value of the output voltage may be difficult in consideration of the different airgap, misalignments, so it is indispensable have a system of the control. A possible solution to control the power flow, can be achieved using the switch mode controller by using an DC/DC converter. The output charge current of the pick-up may be determine operating on the DC/DC converter. A possible DC/DC converter, in particular a buck boost converter, is propose in the following Fig. 1-13:

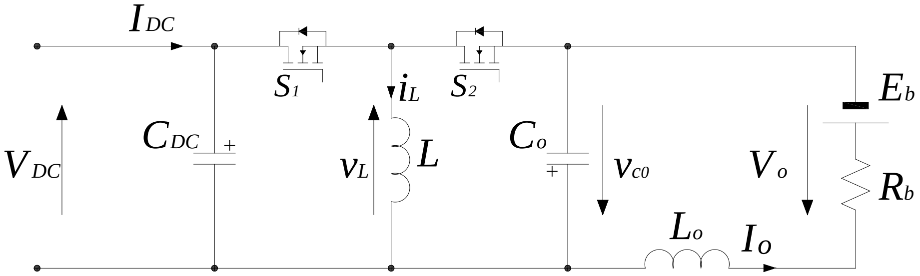

Fig. 1-13: Buck boost converter

Using this converter, the voltage output or the current output may be kept equal to the reference value, independently to the value’s voltage input.

1.2.7 Control Strategies

The power supply and primary controller normally control both the frequency and the primary current to achieve maximum power transfer capability. Both fixed and variable frequency controllers can be used. Power flow regulation is also required because of variations in load and other system parameters.

1) *Power flow regulation*: one common approach to achieve power flow regulation is detune the system by shifting the operational frequency of the power supply. This approach is not suitable for many multiple pickup applications where the load condition on each pickup can be different. Here, detuning the power supply affects all the secondary pickups so that some pickups may be unable to deliver the necessary power. An alternative approach is to use a switched mode controller within the secondary pickup for power flow control. Using this approach, each pickup can be controlled separately or even decoupled completely from the primary. However, the disadvantages are increased switching losses and a higher cost of the secondary pickups.

2) *Fixed frequency control*: with fixed frequency, controlled applications, variations in load and coupling between the primary and secondary will cause a phase shift in the load impedance. If this phase shift is significant, then the power supply must have a higher VA rating for the same power transfer.

3) *Variable frequency control*: most variable frequency controllers operate at the primary ringing frequency. However, the operational frequency will shift away from the load and the degree of coupling between the primary and secondary. This results in a loss of power transfer capability if the frequency shift is too large and may also result in a loss of frequency stability and controllability because of the onset of bifurcation with increasing load, where more than one primary was phase angle frequency exists.

1.2.8 Magnetic Structures

IPT systems use two or more magnetic couplers to transfer power from one frame of reference to another. The most important factor in an IPT system is the magnetic coupling coefficient k and techniques that increase k lead directly to systems that can transfer power more efficiently than others.

In function of type of application, the magnetic structure may be different. In factory automation FA, IPT systems are chosen for their tolerance of dirt in welding bays and paint shops; in Clean Factory Automation (CFA) situations, IPT systems are chosen for their cleanliness and residue free applications. Pickups in these and other factory applications were widely named according to the letter of the Latin alphabet that they most closely resembled for example I, E, and H but other shapes were also suggested, for example an asymmetrical S pickup is difficult to mount but gives almost twice the available power as a symmetrical E pickup for the same material cost [5]. A feature of all of these pickups was that they operated with relatively small air-gaps, and good coupling factors at high efficiency. As the technology and its applications developed these ideal operating conditions, however, became more stressed. Floor mounted systems, generally use two wires 100 mm apart buried under 10 mm of concrete, each with a current of 125 A at 20 kHz. In their primitive form, they used a flat E pickup to achieve coupling factors within 50% of those attainable with a monorail. In monorail applications, the tines on the E and H pickups could encircle the track to 270° whereas floor mounted pickups could not encircle even to 180° giving a low output but they could sense the wire position under the concrete floor and use this information to navigate around the factory. Also, in a new innovation, extra coils could be added to the flat E ferrite converting it into a quadrature pick up where both the power profile and the tolerance to misalignment are enormously improved [reference]. The floor mounted pickups do, however, have the whole track energized all the time and as this may be as long as 300 m it does create a large area in the factory closed to personnel.

Overhead monorails have a track 3,4 m high and this makes them inherently safe but not usable for EVs.

In construction, couplers are fragile and means must be found to protect the coils from damage. The protection usually entails packaging the coils in soft plastics or rubber materials that add significantly to the bulk of the pickup without adding to its function. IPT systems for charging EV batteries, can be seen as an extension of the technology for industrial floor mounted systems and are gaining attention for their convenience of use.

The systems are however quite different as they do not use a track (elongate) but use two wireless pads one on the underside of the vehicle and the other on or under the road surface immediately under the vehicle. With FA system, the misalignments and their air-gaps are small but in the EV application they can be large.

The biggest difficulty of all is that unlike FA, people are, however, commonly near to EV charging equipment and the emission from the vehicle must be contained below international standards [6], [7]. The pads are magnetically coupled to each other.

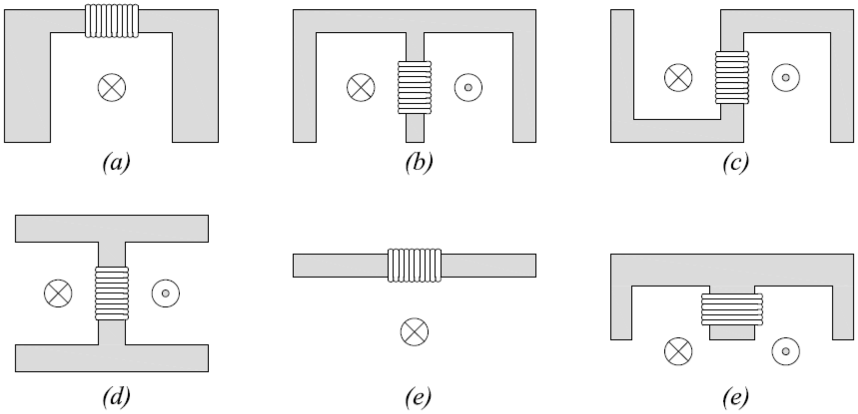

(a) *(b)* *(c)*

(d) *(e)* *(e)*

Fig. 1-14: Factory automation IPT system: the core are called U, E, S, H, I and Flat E corresponding to (a), (b), (c), (d), (e), (f) respectively.

This wireless power transfer uses inductive coupling under resonance with coils or multiples of coils with high native quality factor (Q_L). The coupling is a geometrical property of the magnetic and electrical circuits: better pads achieve coupling depending on their design and a poor design can never be adequately compensated but leads inexorably to a poor IPT system. Early commercial designs were developed in the 90's and have been improved over the past 20 years. As noted before this inductive coupling is a strongly coupled magnetic resonance.

For efficient charging with minimal field leakage the car must be parked or positioned so that the two pads are in relatively close proximity to each other. Under these conditions a recognition system allows the two pads to communicate with each other such that ultimately the pad on the ground is fired up and energy is transferred from the ground pad to the on-vehicle pad and thence to the battery. When the battery is charged, the system disconnects and both the ground pad and the vehicle pad are shut down.

Wireless EV charging via IPT can only occur if several conditions are met simultaneously:

- The pads must be compatible with each other;
- The pads must operate at the same nominal frequency;

- The position of the car must have the on-vehicle pad within the relative x, y, z, error that is allowable for this pad pair;

- The communications protocol must be compatible between the two pads;

- The power ratings and connections of the two pads must be designed to be compatible and at similar rating.

Traditional, practical couplers for EV systems are either circular in shape with a coil in the form of a flat Archimedean spiral placed in magnetic material or shaped like a solenoid using a cylindrical spiral with a magnetic material through the middle of the coil. Such systems have evolved from essentially track based designs to concentrated couplers. In the early system, the essential problem that limited was the unavailability of modern materials. Without ferrite and Litz wire, the pickups are too heavy and without modern power electronics the frequency are too low rather than 20 kHz or higher. In consequence, while the concepts and designs were well thought out, the tolerance for parking or moving is highly constrained, and the cost was too high.

Power pads need to fulfil several requirements to enable practical application on an EV. The pads should be as thin as possible for ground clearance and fitting, operate with a large air gap, be lightweight to minimize vehicle energy requirements and have good tolerance to misalignments to allow easier parking. Designs using pot cores [reference], U cores or E cores are unsuitable for EVs due to excessive thickness or fragility since large pieces of ferrite are required. These topologies are also necessarily sensitive to horizontal misalignment because the coupling surfaces are relative small compared to the size of the pad. The lumped magnetic pad designs used in single point charging applications are generally categorized based on their ability to generate or couple only the parallel, perpendicular or both components of flux entering or leaving the pad surface. A non-polarized pad design ideally generates and couples a flux pattern that is symmetric around the center of the pad, but the term is still used for the pad designs where the fields are directionally symmetric around the pad center though the strength of the field might be different along different angles around the center. On the other hand, a polarized pad generates and couples a flux pattern in which the flux flows dominantly along one dimension of the pad only, in example, either length or width of the pad.

1.2.9 Circular Non-Polarized Pads

For medium and high power, single point charging application using lumped primary and secondary pad designs, the proposed system that utilizes the non-polarized perpendicular flux generation approach consists of an identical circular pad primary and secondary. This pads, derived from pot cores, are designed to generate a single sided flux pattern [8]. Therefore, these pad designs have a coil structure followed by a ferrite structure and an aluminum back plate structure on one side to facilitate a low reluctance flux path while reducing the leakage flux in the back of the pad, with the other side facing on the second pad in the system. As shown in Fig. 1-15, the circular pad consists of a single coil and generates a flux that is symmetric around its center, which also explains a ferrite structure symmetric around the center of the pad.

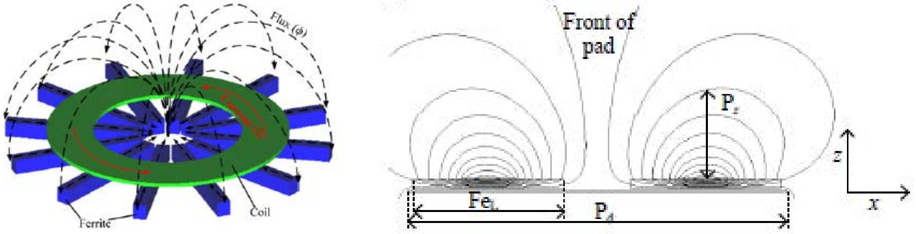

Fig. 1-15: Circular pad

This circular coil adopts ferrite bars instead of ferrite plates to have a compact structure, low weight and low EMF. These are important characteristics because at present EV and PHEV manufacturers are interested in smaller vehicles with low ground clearances giving air-gaps between the primary and secondary pads. In Fig. 1-16, has shown a view of a circular type coil proposed by a team research of Auckland University. It has six main components. The aluminum ring and backing plate add robustness and provide shielding around the pad to leakage flux.

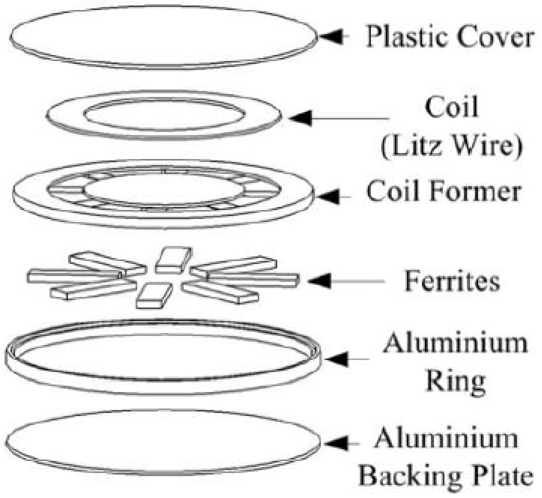

Fig. 1-16: Circular type coil using ferrite bars

In [8], [9], has shown that the ideal coil diameter of a circular pad is 57% of the pad diameter that includes an aluminum ring. The relationship between the size of a pad and its ability to throw flux to a secondary pad placed above it has been explained using the concept of fundamental flux path height [10]. As reported in [8] the fundamental flux path height (Pd) is proportional to half of the ferrite length which is only one quarter of the pad diameter (Pd/4). Therefore, such pads are suitable for stationary charge system and have values of k about 0,17 at height almost four times lower than the pad diameter. This means it is necessary to use pads with excessive diameter.

Unlimited EV range can be realized with dynamic charging system however the receiver on the EV must work equally well with both stationary and moving transmitter pads. Circular pads are not suitable for dynamic charging as they have a null in their power profiles when horizontally offset by 38% of the pad diameter [8]. The null occurs within the pad diameter so even if transmitter pads are touching along the highway, it is not possible to obtain a smooth power profile.

1.2.10 Solenoid Polarized Pads

In order to obtain a desirable coupling coefficient whit air gaps in the range of 150-250 mm, the diameter of a circular pad needs to be increased significantly

[10], [11]. The polarized couplers have a defined north and south pole created by wrapping a flat coil around a flat ferrite structure, as showed in Fig. 1-17.

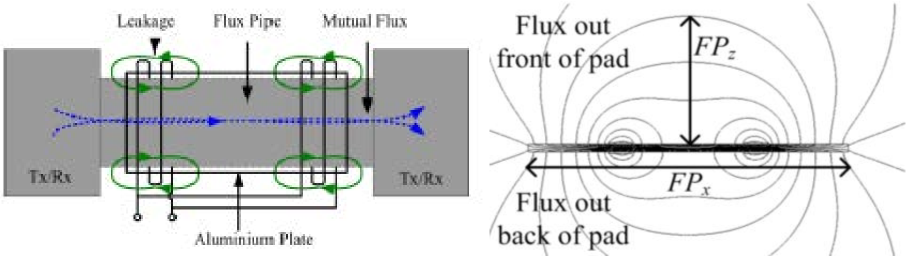

Fig. 1-17: Polarized solenoidal pad

These couplers consist of a rectangular ferrite bar with coil wound along its length. As such these pads are essentially flattened solenoids. Two coils are required to create a polarized flux and are connected magnetically in series and electrically in parallel, to lower the inductance seen by the power supply. The distance between the end north and south poles and the size of the poles are each carefully designed based on application. In this type of pad the field is much higher than that of the non-polarized pad. without any added aluminum or chopper shielding the field is naturally produced on both sides of the pad. To avoid the rear flux, may be used an aluminum or copper sheet covering the entire back structure, so that only one side of the end poles is exposed to help direct the flux towards the other magnetic pad resulting in essentially single sided fields but there is a significant drop in the quality factor Q. The loss lowers the system efficiency below what is practically desirable for an EV charging system.

1.2.11 Double D Polarized Pads

The double D pad, showed in Fig. 1-18 [11], is a pad that combines the advantages of both the circular and flux pipe designs and eliminates the unwanted rear flux paths.

The coils are connected magnetically in series and electrically in parallel. Coplanar coils are placed on top of ferrite strips. The ferrite channels the main flux behind the coils and forces the flux to radiate on one side so there is no MMF produced that can drive the flux out of the back. This allows aluminum shielding to be placed underneath with little impact on quality factor Q, creating a single sided flux pad with a path height proportional to half of the pad length.

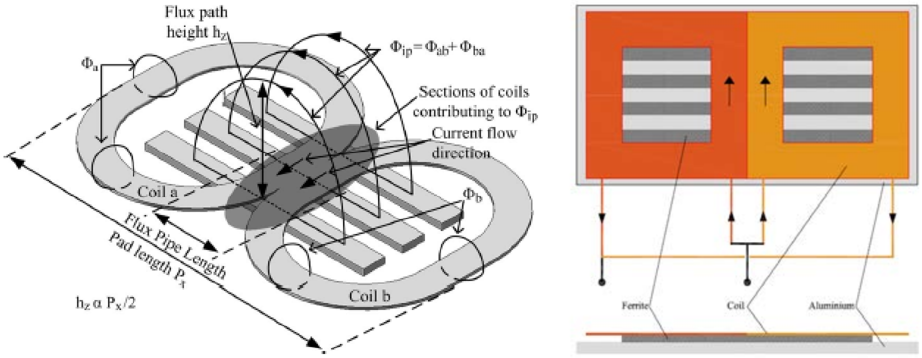

Fig. 1-18:DD pad

The height of flux may be controlled adjusting the width of the coils in the shaded area to create a flux pipe between the two coils. The fraction of this flux that couples to the receiver pad is mutual flux, therefore, the section of the coil forming the flux pipe should be made as long as possible, whereas, the remaining length of the coil should be minimized to save copper and lower the resistance. Doing so results in coil shaped like a D, and since there are two of such coils placed back to back, the pad is called double D (DD). The characteristics of a DD pad are the single sided flux paths, an average flux path height that is proportional to half of the length of the pad, insensitivity to aluminum shielding, and low leakage flux out of the back. All these characteristics are desirable in large air gap inductive couplers. A limit of these type of pads is that the performance of the coupling along the x axis is not as good as the y axis. This is due to a coupling null that occurs when the horizontal offset is about 34% of the pad length in the x axis. At this position the flux enters and exits the same coil, resulting in no induced voltage. The other coil is sufficiently far away from the transmitter, so it interests little flux. This impose a fundamental x axis tolerance limit for DD coils in a similar manner of circular pads.

1.2.12 Double D Quadrature Polarized Pad

DD receiver coils can only couple horizontal flux components, as such the tolerance of the receiver pad to horizontal offsets in the x direction can be significantly improved if a second receiver coil is added [12]. This coil is designed to capture only vertical flux and is in spatial quadrature to the DD. The additional coil requires lengthened ferrite strips to enhance flux capture and the combined structure is called DD Quadrature (DDQ). There is no mutual flux between the DD coils and quadrature coil and when the receiver pad is horizontally offset, the quadrature coil is positioned to capture the field and able to supply the output power.

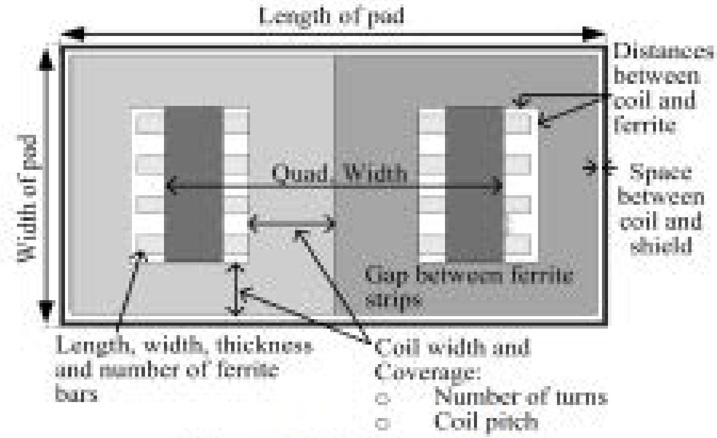

Fig. 1-19: DDQ pad

1.2.13 Bipolar Polarized Pad

The Bipolar Polarized pad (BP), consists of two identical, partially overlapped and mutually decoupled coils with one side of the coils sitting immediately next to a ferrite structure followed by an aluminum back plate, while the other side facing the transmitter [13]. The coils are arranged to have a mutual coefficient null so the coils are magnetically independent. In fact, the magnetic field produced by a coil crosses the coil plane in one direction inside the coil and cross the same plane in the opposite direction outside the coil [14].

The mutual decoupling of the coils constituting the BPP is achieved by adjusting the overlap of the two coils in such a way that the net flux linkage between the two coils is zero. As shown in Fig. 1-20, current I_{c1} in coil 1 produces a flux φ_1. The area covered by coil 2 is divided into two parts: as overlapped area S_2 and a non-overlapped area S_1. The flux going through S_1 and S_2 are opposite in direction and the net flux linkage is zero if the two BPP coils do not share exactly the same plane as one is sitting right next to the ferrite structure while there is a gap between the ferrite structure and the other coil. This orientation causes a slight difference in the self-inductances and the track to coil mutual coupling of the two coils.

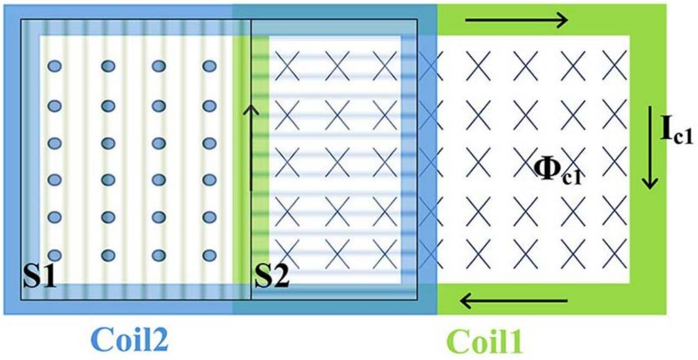

Fig. 1-20: mutual decoupling

A simple solution is to bend one of the coils only where it overlaps the other coil with the rest of the coil structure sharing exactly the same plane as the other coil.

Ferrite must be used in order to have channel flux to creating a single side flux pattern and improve coupling. When an aluminum back plate is used to block the leakage flux above the pad and limit the EMI, there is low loss. The BP pads are able to approximately replicate the performance of the DDQ pads using about 26% less copper than DDQ pads therefore are more efficient and lower cost.

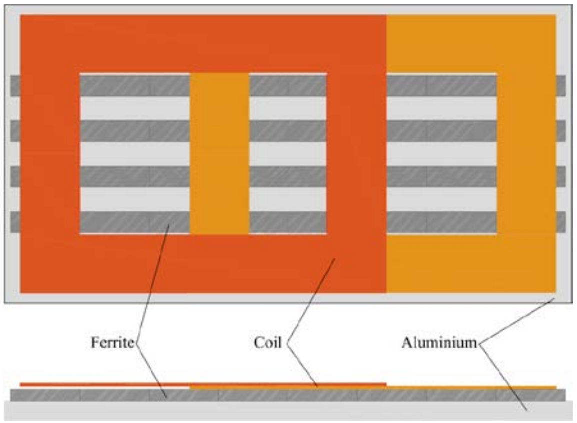

Fig. 1-21: BP pad

1.2.14 Comparison of EV pad combinations

In order to have a power transfer from the refill station to the vehicle, it is necessary use two of the above-mentioned pads, one operating as transmitter buried in the roadway and the other operating as receiver mounted on the chassis of the vehicle. In according to the pads chosen, may be various combinations and a larger coupling coefficient as well as better lateral and longitudinal tolerances compared with the circular coil may be obtained 0, [15]. Though, the multicoils polarized pads DDQ and BP can be used as the primary pads, we use they as the secondary pads. If, either DDQ or BP pads are used as the primary pad, this requires a second synchronized power supply to enable the independent coils to be driven separately. These pads use two completely independent windings to capture all of the available flux in the secondary ferrite, enabling much wider tolerance to lateral off sets than any other pad. The independent nature of the windings means they can be separately tuned and regulated as required to extract power. In Fig. 1-23 are shown the outputs of a matched pair of possible combinations of couplers having almost identical areas and inductances, compared under identical driving conditions.

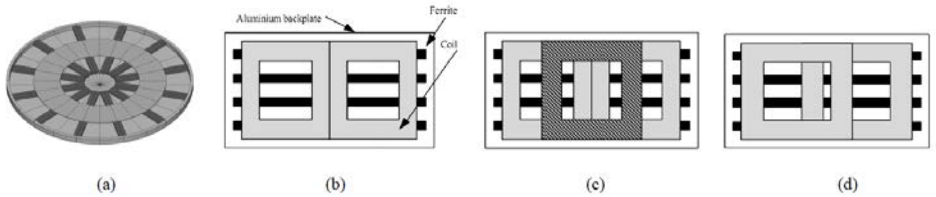

Fig. 1-22: Pad structure: a) Circular pad, b) DD pad, c) DDQ pad, d) BP pad

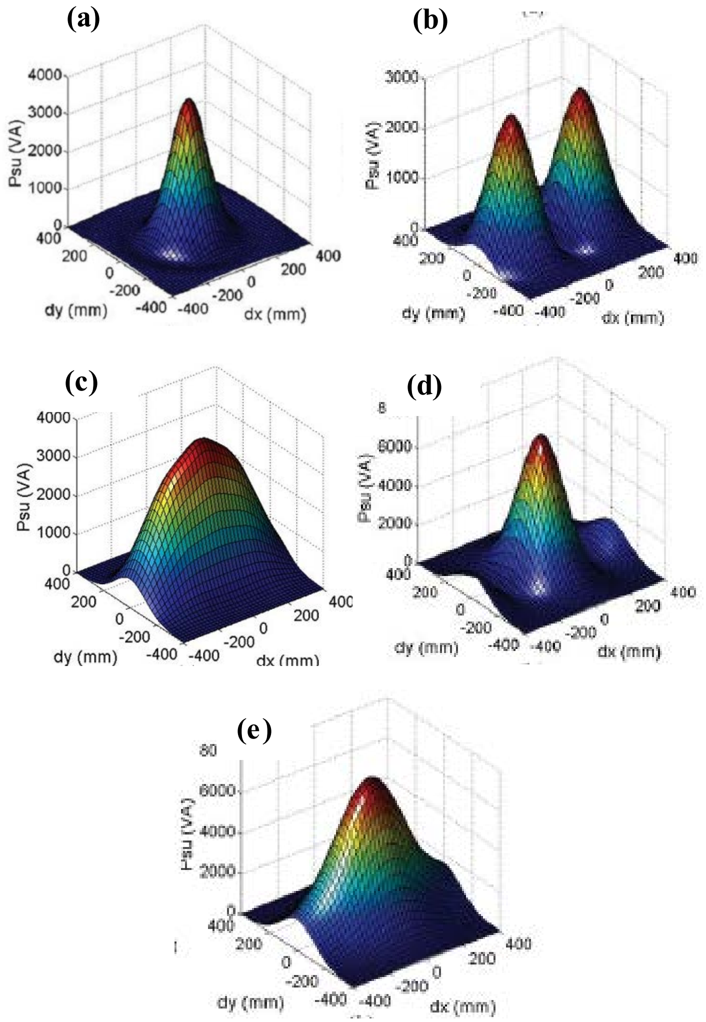

Fig. 1-23: a) Circular on circular pad, b) DD on circular pad, c) DDQ or BP on circular pad, d) DD on DD, e) DDQ or BP on DD

The Fig. 1-23 a), b), c), d) show the uncompensated power transfer when a circular pad is used as the primary pad with the various secondary pads such as Circular, DD, DDQ and BP. Instead the Fig. 1-23 e) and f) show the uncompensated power transfer when a DD pad is used as the primary pas with the various secondary pads as DD, DDQ and BP.

a) Circular-Circular: the maximum power transfer is obtained when they are centered but the power transfer band is very narrow to any misalignment;
b) DD-Circular: The DD secondary pad can be coupled only horizontal flux at its center. The non-polarized primary pad cannot transfer power to the DD pad when they are centered on each other and these needs to be offset from each other to capture flux. This means that a vehicle must be misaligned from the primary coil to transfer power;
c) DDQ or BP-Circular: the two independent coils of secondary pads are sensitive to both the horizontal and vertical flux components. This allows high power transfer to be achieved when centered on the primary pad. Furthermore, it shows wide lateral tolerance and better coupling despite misalignments;
d) DD-DD: As shown in the figure, the maximum power transfer is obtained when they are centered but the transfer band is very narrow to any misalignment. The value of transfer power is higher than the case a, this means that for the same of air gap and transfer power may be used smaller sized pads or for the same size and transfer power may be reached a higher airgap;
e) DDQ or BP-DD: the use DDQ or BP pad on a vehicle enables a power zone which is around three times larger in comparison with the other cases. Coupling and power transfers are better suited to large airgaps.

1.2.15 Dynamic EV charging

As already mentioned, an IPT system could be the fundamental key for a wide diffusion of EV, limited, essentially, to a high cost of batteries, a limited energy autonomy, a long charging time and a no large presence of refill stations [3]. Besides, to the classical stationary refill station, could be interesting the dynamic refill system. The vehicle autonomy can be extended reloading the battery during the trip if the road including an induction charging station. Different ways are possible to transfer energy wireless and dynamically avoiding any sliding contact.

Based on the previously concentrated pads, a sequence of primary pads can be placed in the road with dimension and the distance between them carefully set. While the vehicle flows on a dedicated path, by means of a detection system, only the pads covered of the vehicle are energized.

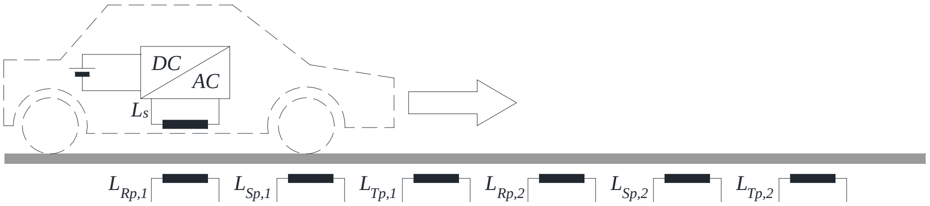

Fig. 1-24: dynamic charging

1.2.16 Compensation

The primary and secondary coils of the IPT system can be represented as a loosely coupled transformer as shown in Fig. 1-25. The analysis of the topology can be simplified by implementing the mutual inductance between the coils [15]. The self-inductance of each coil ($L_{prim,self}$, $L_{sec,self}$) in this case consists of the leakage inductance ($L_{prim,leak}$, $L_{sec,leak}$), which represents the flux that does not link to the other coil, and the mutual inductance (M), representing the part of the flux that is coupled between the two coils.

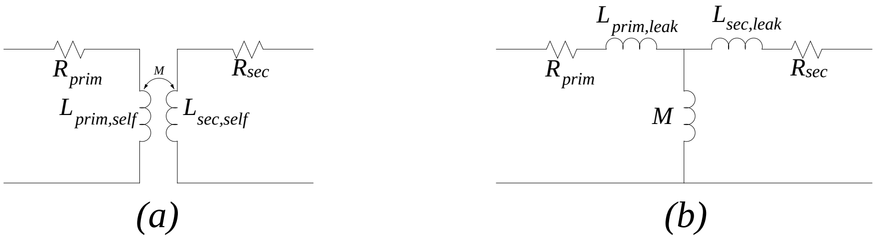

Fig. 1-25: IPT coil representation (a) self-inductance (b) leakage and mutual inductance

In each case the coils are represented as the respective coil inductances in series with an equivalent resistance. The lumped resistance models the resistance of the conductors, depending on the coil length, taking into account the frequency dependence, by skin and proximity effects.

The IPT system design has to have a relatively large air gap in order to account for the required clearance between the vehicle and the road. Especially in distributed systems, where only a small part of the primary track is linked with the secondary, the value of the primary and secondary leakage inductances can be relatively high. This imply the need to compensate the reactive power seen from the power supply connected to the primary side by using capacitors connected both at the primary and secondary coils, in order to ensure operation at power factor close to unity.

According to the connection of the capacitive compensation to the primary and secondary coil as shown in Fig. 1-26, the compensation techniques can be categorized as: in series with primary and in series with secondary coil SS; in series with primary and in parallel with secondary coil SP; in parallel with primary and in series with secondary coil PS; in parallel with primary and in parallel with secondary coil PP;

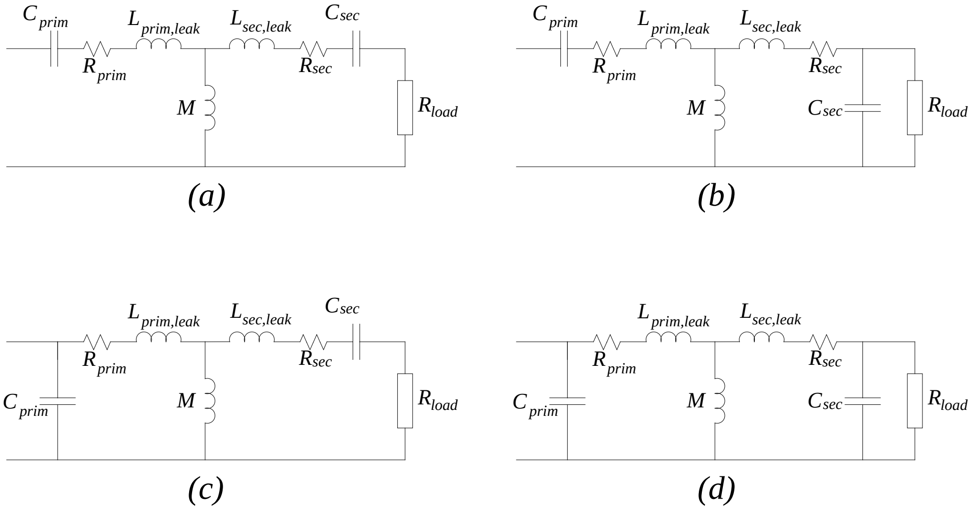

Fig. 1-26: Capacitive compensation topologies (a) SS (b) SP (c) PS (d) PP

1.2.16.1 Capacitive compensation – Secondary coil:

In each case, the secondary compensating capacitance is calculated accounting for the whole self-inductance of the secondary coil, defined as the sum of the secondary leakage inductance and the mutual inductance. To ensure resonant operation, the capacitive reactance $X_{sec,cap}$ must be equal to the total inductive reactance of the secondary, because of the mutual inductive reactance X_{mutual} and the secondary leakage inductive reactance $X_{sec,leak}$.

$$X_{\sec,leak} + X_{mutual} = X_{\sec,cap} \tag{1.6}$$

Expressing the reactance in terms of the resonant angular frequency ω_0 of the LC network generated, the secondary capacitance can be calculated for each different connection type of the secondary compensation as:

$$C_{\sec} = \frac{1}{\omega_0^2 L_{\sec,self}} = \frac{1}{\omega_0^2 \left(L_{\sec,self} + M\right)} \qquad (1.7)$$

The operating frequency of the system is set, according to the above equation, by the choice of capacitive compensation for a specific layout inductance value. The primary compensation is calculated in a similar manner, using the frequency value as defined from the secondary resonance.

1.2.16.2 Capacitive compensation – Primary coil:

The analytical equations, governing the calculation of the primary capacitive compensation, differ for each connection type. The frequency is set from the secondary LC network of the topology, as explained earlier. The primary capacitance is chosen so that the total impedance is only resistive, as seen from the source or the input terminals of the network. Equivalent circuit, shown in Fig. 1-26, representation of the topologies enables a straight-forward way to calculate the adequate compensation for each type. As a first step, the equivalent impedance as seen from the source is derived. The required value of capacitive compensation is then calculated, so that the imaginary part of the total impedance is equal to zero. Analytical derivation of the following expressions can be found in [16].

Tab. 1:: primary coil capacitive compensation relations to system parameters

Compensation topology	Primary compensation
SS	$C_{prim} = \frac{1}{\omega_0^2 L_{prim,self}}$
SP	$C_{\sec} = \frac{1}{\omega_0^2 L_{prim,self} - \frac{M^2}{L_{\sec,self}}}$

PS	$C_{\sec} = \dfrac{1}{\dfrac{\omega_0^2 M^2}{R_{load}} + \omega_0^2 L_{prim,self}^2}$
PP	$C_{\sec} = \dfrac{L_{prim,self} - M^2 / L_{\sec,self}}{\left(\dfrac{\omega_0^2 R_{load}}{L_{\sec,self}^2}\right)^2 + \omega_0^2 \left(L_{prim,self} - \dfrac{M^2}{L_{\sec,self}}\right)^2}$

As noted in the above table, the primary capacitive compensation for the SP, PS and PP topologies depends on the load of the system and the mutual inductance between primary and secondary windings. For the SS compensation both the primary and secondary winding compensating capacitor values are independent of the load. Different alignment conditions can influence the load and the mutual inductance as seen from the primary input terminals, thus for systems that alignment imperfections can occur between the primary and the secondary the SS compensation is preferable.

In order to choose the proper primary and secondary compensation topologies generally can be take in account as follow below. A series compensated secondary can supply a stable voltage, while a parallel compensated secondary is able to supply a stable current. A series compensated primary is normally required to reduce the primary voltage to manageable levels for long track applications, whereas a parallel compensated primary is usually used to give a large primary current.

1.2.17 Health Risks

Although wireless charging systems has many advantages for EV charging, the technology also poses potentially significant safety concerns such as electrical shock due to the high electrical power, high magnetic field exposure to the general public that may exceed standards. These concerns are primarily due to the presence of large power levels and large electromagnetic fields [6], [7], [17].

Electromagnetic field (EMF) exposure is a major concern for wireless charging for EVs. EMF exposure need to be rigorously analyzed to be within acceptable levels specified by safety standards, both under normal conditions as well as unusual conditions such as during abnormal operation, presence of human under the vehicle, potential abuse, etc. for the driver and passengers in the car, the radiation hazard may be less concerned due to the shielding of metal chassis of the car. Apparently, for the EVs, the most hazardous radiation zone is right between the two coils, and secondary hazardous zone is around the coils. These areas are the most hazardous but they are not directly exposed to human or animal.

There are two international groups that set standards guidelines for human exposure to electromagnetic field:

- The International Committee on Electromagnetic Safety (ICES) under the Institute of Electrical Electronic Engineers (IEEE);
- The International Commission on Non-Ionizing Radiation Protection (ICNIRP).

The radiation restrictions set differently for general public and occupationally exposed population consists of adults who are generally exposed under know conditions and are trained to be aware of potential risk and to take appropriate precautions.

According to the IEE Standard C95.1-2005, below 100 kHz only the electrostimulation limits apply, above 5 Mhz only the thermal limits apply and both sets of limits apply in the transition region between 100 kHz to 5 MHz. The two types of recommendations for IEEE are expressed in terms of basic restrictions and max permissible exposure values. The permissible exposures between 3 kHz and 5 MHz is 163 A/m for magnetic field strength and 0,205 mT for magnetic flux density.

For ICNIRP, the two type of recommendations are basic restrictions and reference levels. The reference level in ICNIRP is similar to the maximum permissible exposure values. In terms of basic restriction comparing with the IEEE standard, ICNIRP uses current density J [mA/m^2] as the unit. The relationship between the current density J and the internal electric field by Ohm’s law $J=\sigma E$, where σ is the electrical conductivity of the medium tissue.

The ICNIRP has only one general limit for basic restrictions but the ICES (IEEE) has multiple limits for different parts of body tissue. The ICNIRP recommendation for general public is much conservative between 10 to 100 kHz and for example, the exposure guideline specifies the maximum level for occupational exposure to be 100 μT and the maximum level for general public to be 27 μT.

Due to the large area of electromagnetic field exposure between the car and the primary coil and high electrical power involved in this application, the system needs to be designed accordingly in order to meet the safety standard.

Under such condition that safety is certified, efficiency and charging cycle are also required to meet the customer's expectation.

1.3 References

[1] Covic, G.A.; Boys, J.T., "Modern Trends in Inductive Power Transfer for Transportation Applications,"Emerging and Selected Topics in Power Electronics", IEEE Journal, vol.1, no.1, pp.28,41, March 2013 doi: 10.1109/JESTPE.2013.2264473.

[2] J. T. Boys and G. A. Covic, "The Inductive Power Transfer Story at the University of Auckland," in *IEEE Circuits and Systems Magazine*, vol. 15, no. 2, pp. 6-27, Second quarter 2015.

[3] G. Nagendra, L. Chen, G. Covic, J. Boys, "Detection of EVs on IPT Highways", IEEE Vol.2, NO.3, SEPTEMBER 2014.

[4] J. T. Boys, C. Y. Huang and G. A. Covic, "Single-phase unity power-factor inductive power transfer system," 2008 IEEE Power Electronics Specialists Conference, Rhodes, 2008, pp. 3701-3706.

[5] Boys, Covic, "IPT Fact Sheet Series: Magnetic Circuits for Powering Electric Vehicles".

[6] International Commission on Non-Ionizing Radiation Protection, "Guidelines for limiting exposure to time-varying electric and magnetic, fields (1 Hz to 100 kHz)," Health Phys., vol. 99, no. 6, pp. 818–836, Dec. 2010.

[7] International Commission on Non-Ionizing Radiation Protection, "Guidelines for limiting exposure to time-varying electric, magnetic, and electromagnetic fields (up to 300 Ghz)," Health Phys., vol. 74, no. 4, pp. 494–592, 1998.

[8] M. Budhia, G. Covic and J. Boys, "Design and Optimization of Circular Magnetic Structures for Lumped Inductive Power Transfer Systems," Power Electronics, IEEE Transactions on, 9, pp. 1-14, accepted for publication.

[9] M. Budhia, G. A. Covic and J. T. Boys, "Design and optimization of magnetic structures for lumped Inductive Power Transfer systems," in Energy Conversion Congress and Exposition, 2009. ECCE 2009. IEEE, 2009, pp. 2081-2088.

[10] Budhia, M.; Covic, G.; Boys, J., "A new IPT magnetic coupler for electric vehicle charging systems," IECON 2010 - 36th Annual Conference on IEEE Industrial Electronics Society, vol., no., pp.2487,2492, 7-10 Nov. 2010

[11] Budhia, M.; Boys, J.T.; Covic, G.A.; Chang-Yu Huang, "Development of a Single-Sided Flux Magnetic Coupler for Electric Vehicle IPT Charging Systems," Industrial Electronics, IEEE Transactions on, vol.60, no.1, pp.318,328, Jan. 2013

[12] Budhia, M.; Boys, J.T.; Covic, G.A.; Chang-Yu Huang, "Development and evaluation of single sided flux couplers for contactless electric vehicle charging," 2011 IEEE Energy Conversion Congress and Exposition, Phoenix, AZ, 2011, pp. 614-621

[13] A. Zaheer, D. Kacprzak and G. A. Covic, "A bipolar receiver pad in a lumped IPT system for electric vehicle charging applications," 2012 IEEE Energy Conversion Congress and Exposition (ECCE), Raleigh, NC, 2012, pp. 283-290.

[14] A. Zaheer, G. A. Covic and D. Kacprzak, "A Bipolar Pad in a 10-kHz 300-W Distributed IPT System for AGV Applications," in IEEE Transactions on Industrial Electronics, vol. 61, no. 7, pp. 3288-3301, July 2014.

[15] S. Y. Choi, B. W. Gu, S. Y. Jeong and C. T. Rim, "Advances in Wireless Power Transfer Systems for Roadway-Powered Electric Vehicles," in IEEE Journal of Emerging and Selected Topics in Power Electronics, vol. 3, no. 1, pp. 18-36, March 2015.

[16] S. Li and C. C. Mi, "Wireless Power Transfer for Electric Vehicle Applications," in IEEE Journal of Emerging and Selected Topics in Power Electronics, vol. 3, no. 1, pp. 4-17, March 2015.

[17] H. Jiang, P. Brazis, M. Tabaddor and J. Bablo, "Safety considerations of wireless charger for electric vehicles: A review paper," 2012 IEEE Symposium on Product Compliance Engineering Proceedings, Portland, OR, 2012, pp. 1-6.

Chapter 2

Proposed Induction Power Transfer System

2.1 Introduction

In this chapter, the proposed IPT system is analyzed. The system is designed in order to ensure a high coupling coefficient, not only under perfect alignment operation, but also when the secondary is misaligned with respect to the primary.

The dimensions of the chosen pads are fixed taking into account the physical constrictions, and the main parameters are computed using finite element analysis for different possible scenarios.

The design of the system is aimed for electric vehicle stationary charging, but the proposed system should be easily extendable for the dynamic charge. As a result, the dimensions of the layouts considered must be able to fit in the real constrains, essentially the chassis of an electric vehicle on a standard road lane. A clearance of vehicle to ground of 200 mm is considered, for real scale applications.

2.2 Proposed IPT

The proper IPT system has been chosen taking into account the considerations explained in precedent chapter. The secondary pad designed must be mountable on the chassis of the vehicles, thus they must fit at the low width and thickness of the electric vehicles. Therefore, is crucial for this application, use polarized pads, in particular the combination of double D pad for the primary and bipolar pad for the secondary, in order to achieve a good behavior respect to possible misalignment. In the following Fig. 2-1 is shown the proposed system 0.

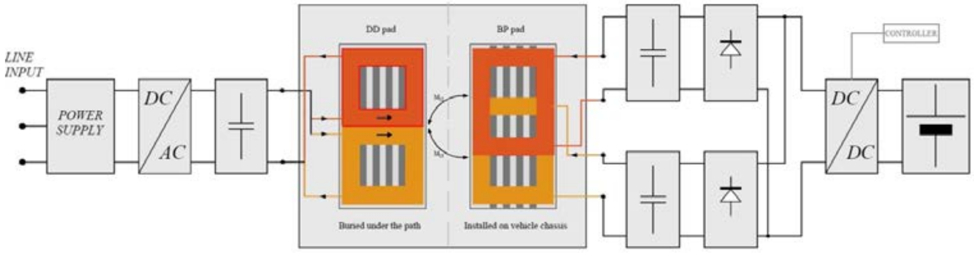

Fig. 2-1: Block diagram of DD (Double D primary PAD) – BP (Bipolar secondary) PADs

2.2.1 Power supply

The electrical power is transferred through a very low frequency magnetic field from a power supply to a pick up over some physical distance. The power supply is a resonant converter and takes power from a utility and converts it to a current at very low frequency (in the range 5-50 kHz) which is used to energize the transmitter pad tuned with power capacitors to resonate at the power supply operating frequency to boost power transfer. In the power ranges that are common today the input from the utility supply is conveniently 400 V 3-phase and the design of the power is then conceptually simple with a 3-phase rectifier, DC capacitor and an H bridge to produce the higher frequency output current constant in magnitude.

The power supply circuit is shown in Fig. 2-2. It shows a three-phase rectifier directly connected to a DC bus capacitor. An H bridge operates directly from this rectified voltage to produce a quasi-square wave output. The AC magnitude of this voltage follows the rectified mains power supply waveform and may be controlled electronically by varying the mark space ratio in the H bridge producing the waveform. Any DC offset is blocked by capacitor C_{dc} and this AC voltage is then the input voltage to an LCL circuit [2]. As, has been pointed out in [3], when operated at the resonant frequency, the LCL-T behaves like a current source.

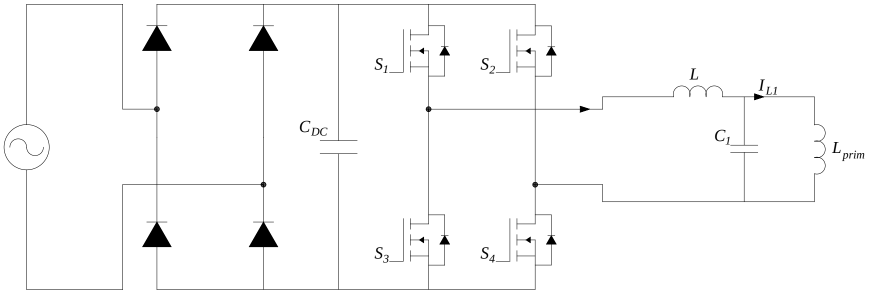

Fig. 2-2: IPT primary power supply

That is, under these conditions, the output current is constant irrespective of load variations. Therefore, for the next analysis, the power supply can be represented by means of a current generator.

2.2.2 Magnetic Coupler

Numerous variables need to be considered when designing a magnetic pad and correlating all of them is impractical and provides little insight into the overall design objectives. As such, usually a heuristic approach is used based on experience.

2.2.2.1 General consideration

As mentioned before, for the particular application, the magnetic pad chosen are the double D (DD) for the transmitter and the bipolar (BP) for the receiver.

Both the DD and the BP pad are made of ferrite. To simplify the design, readily available ferrite I core sets measuring 93 mm x 28 mm x 16 mm are used to make the strips as shown in Fig. 2-3: Ferrite I core.

Each strip is made up of an integer number of cores, therefore avoiding any difficulties associated with cutting ferrite. The thickness of the ferrite bars has the least effect on coupling because fundamental flux paths are unaffected.

Fig. 2-3: Ferrite I core

The flux density on the mutual flux path should be as high as possible to ensure maximum ferrite utilization. The ferrite material used is N87 and it has the lowest loss at 80 °C. Flux densities above 200 mT do increase core losses and the operating temperature. However, the saturation only occurs if the peak flux density reaches 400 mT.

One of the main effects of higher frequency operation is the increase in the resistance value of both the primary and the secondary coils. The increased resistance at high frequencies results in additional resistive losses. This phenomenon is mainly due to the skin effect present in the conductors of the layout that increases with the frequency of the alternating currents flowing in the topology. Skin effect is the distribution of the alternating electric current in a conductor in such a way that most of the current flow propagates near the surface of the conductor. This effect is caused by circulating eddy currents in the conductor, cancelling the current flow in the center of the wire and adding to the regular current flow in the area closer to the surface. Thus, the available conductor cross section decrease exponentially resulting in the increase of the effective resistance. In order for the skin effect to have a smaller influence on the resistance value, litz wire is used for the primary and secondary conductors. In Fig. 2-4, is shown an image of litz wire.

This wire consists of a large number of stranded low diameter conductors. According to the required operating frequency, the wire is chosen so that the skin depth has a value larger than the diameter of stranded conductors. With a frequency of the 25 kHz the skin depth is about 0.4126 mm.

Fig. 2-4: Example of Litz wire

A readily available 810 x 0.1 mm litz wire given a total cross sectional area of 6,36 mm^2 and with a diameter of 4 mm is used in the designs consideration. The diameter of the stranded conductors is smaller than the minimum skin depth, so the skin effect is limited. A current density of approximately 4 A/mm^2 provides a good balance between copper loss and utilization with any pad design, therefore the pad current in each coil is set to 23 A.

The length of the pad is governed by the length of the ferrite strips and the number of turns in the coils. Whereas, the with is primarily determined by the number of strips, the spacing between them and the number of turns.

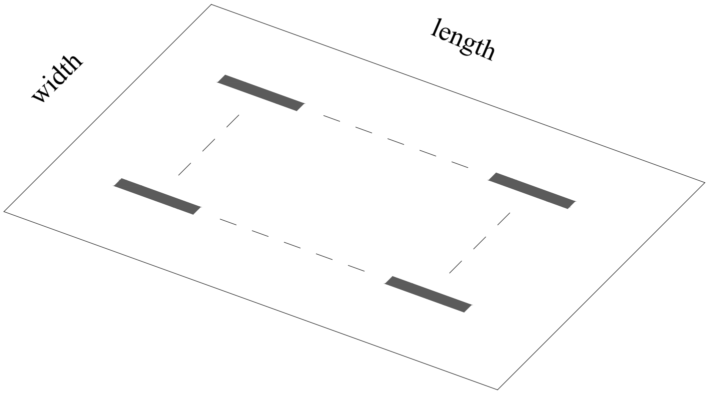

Fig. 2-5: Ferrite arrangement

Moreover, the length of the pad should be chosen in order to have a good coupling for an airgap of 200 mm. As mentioned in precedent chapter, with this type of polarized pad the height of the flux is almost half of the pad length, thus the length of pad will be higher of 400 mm. The pad width has been chosen to ensure that the area enclosed by each coil is sufficient to capture the desired flux over the intended gap.

The length of the flux pipe is governed by the coverage of the midsection. This is expressed as the percentage of ferrite strip covered by the coils forming the flux pipe and depends on the number of turns and pitch of the coil. Narrow coils with few turns closely spaced shorten the flux pipe, causing reduced coupling to a receiver at a given distance. Conversely, if the coils are wounded with an extremely large pitch, flux will leak out of the gaps between turns causing the air gap flux to collapse effectively, resulting in a short flux pipe [4]. Using a large number of turns has the desirable effect of increasing the length of the flux pipe but the inductance will be high making driving the pad difficult. Furthermore, the excessive amount of copper required adds weight and makes the pad expensive.

Taking into account all this consideration it is possible fix the dimension of DD and BP pads.

2.2.2.2 DD pad

In the following Fig. 2-6 is shown the DD pad whereas in the Tab. 2 are reported the dimensions.

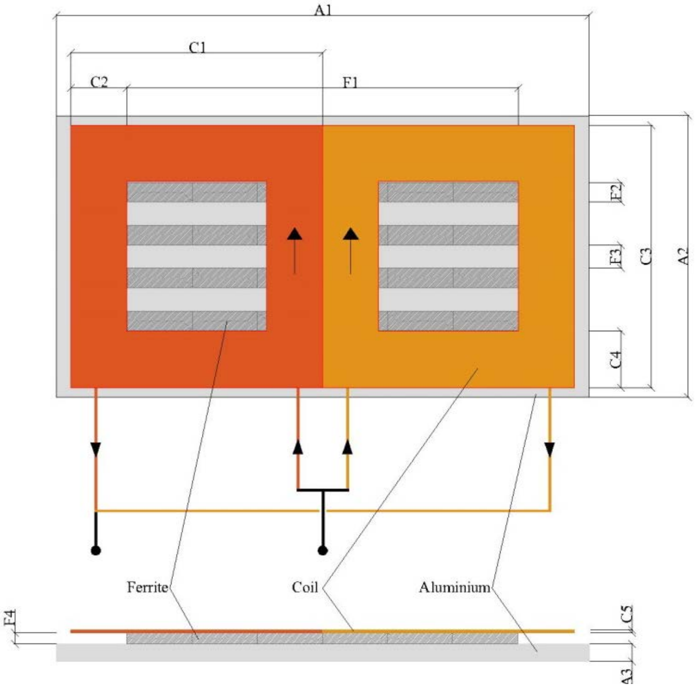

Fig. 2-6: DD pad dimensions

Tab. 2: DD dimensions

Label	Dimension [mm]
A1	760
A2	400
A3	25
Number of ferrite strips	6
Type of ferrite	N87 (93x28x16)
F1	558

F2	28
F3	33
F4	16
C1	359.5
C2	80
C3	373
C4	80
C5	4
Coils turns	20 each
Litz wire	810 x 0.1 mm – 6.36 mm^2

2.2.2.3 BP Pad

In the following Fig. 2-7 is shown the BP pad whereas in Tab. 3 are reported the dimensions.

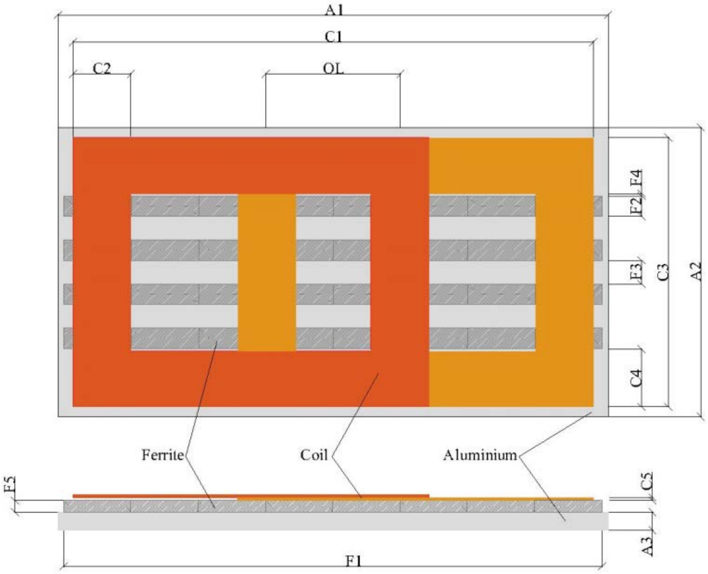

Fig. 2-7: BP pad dimensions

Tab. 3: BP dimensions

Label	Dimension [mm]
A1	775
A2	485
A3	25
Number of ferrite strips	8
Type of ferrite	N87 (93x28x16)
F1	744
F2	28
F3	33
F4	10
F5	16
C1	738
C2	80
C3	391
C4	80
C5	4
O1	157.5
Coils turns	20 each
Litz wire	810 x 0.1 mm – 6.36 mm^2

2.2.2.4 Finite Element Method Analysis

In order to simulate the magnetic field generation and calculate the main parameter of the proposed IPT system, the latter has been analyzed using finite element technique. This process involves designing the topology in a finite element software, creating a mesh of elements and solving the differential equations governing the problem at hand according to the set border limit conditions. The FEM software used (FLUX CEDRAT) generates a mesh and then the electromagnetic equations are imposed on the mesh and solved for each element. According to the border values set, in this case zero flux density value at a large distance from the layout, an error function, defining the accuracy of the solver is minimized. As a general rule, a finer mesh and lower error values would improve the accuracy of the output, but the solution would require a longer time. The magnetic properties of the materials used can be specified separately, for each frequency of interest. The most precise calculation of the magnetic field can be conducted using a three-dimensional layout. In the following Fig. 2-8 is shown the isovalue map of the magnetic flux density. The y-axis is the direction of moving of the vehicle whereas the x-axis is the direction of possible lateral misalignment of the vehicle.

The IPT system has been analyzed for different scenarios, that could occur in practical operating condition. They have been taking into account three different values of airgap. Furthermore, the system has been analyzed in different possible y and x misalignment. In the Tab. 4 are reported the case of study.

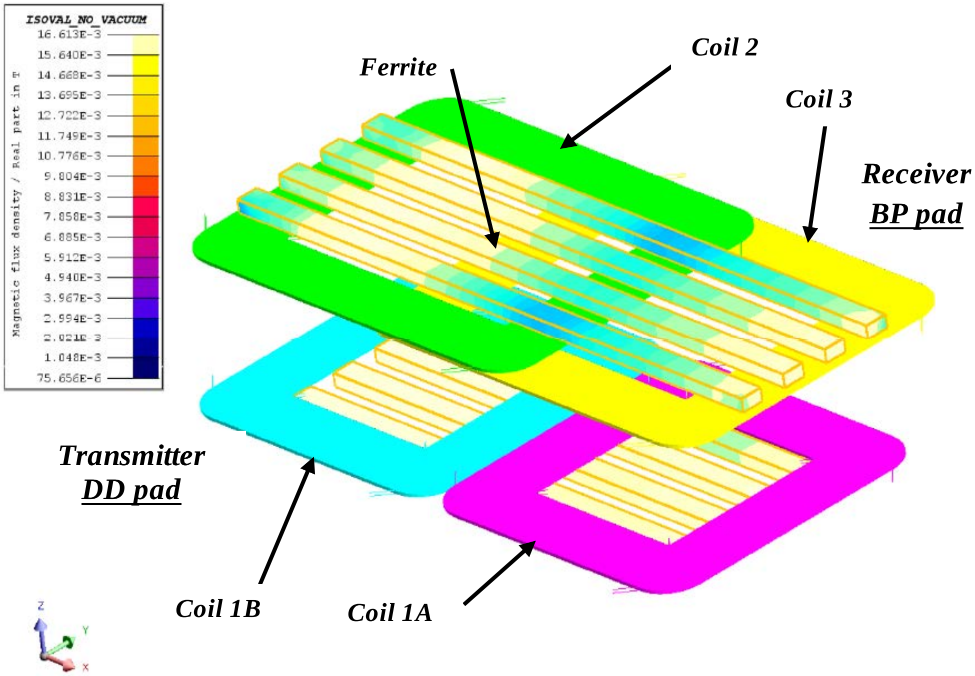

Fig. 2-8: Isovalues map of magnetic flux density: 3D view of DD-BP IPT system

Tab. 4: Case of study

z airgap [mm]	x misalignment [mm]	y misalignment [mm]
150	-186	-106
200	-139,5	-79,5
250	-93	-53
-	-46,5	-26,5
-	0	0
-	46,5	26,5
-	93	53
	139,5	79,5
	186	106

For each case of study, the analysis has been done with an imposed current before in the primary and then in the secondary coils. In this way, the self-inductance and the mutual inductance of the system have been calculated according to the follows expression:

$$L_i = \frac{\iint_{S_{Li}} B_{Li}\hat{n}dS}{I_{Li}} \tag{2.1}$$

$$M_{ij} = \frac{\iint_{S_{Li}} B_{Li}\hat{n}dS}{I_{Lj}} \tag{2.2}$$

where S_{Li} is the linkage surface, L_i is the self-inductance, M_{ij} is the mutual-inductance and the I_{Lj} are the imposed current in the primary and secondary windings for the calculations of inductances.

As mentioned in the previous, the DD pad is constituted by means of two coplanar coils, connected magnetically in series and electrically in parallel. In order to obtain the equivalent inductance of the pad has been used the expression:

$$L_1 = \frac{L_{1A} \cdot L_{1B} - L_{1AB}^2}{L_{1A} + L_{1B} - 2L_{1AB}} \tag{2.3}$$

where L_1 is the self-inductance of the DD pad, L_{1A} is the self-inductance of the first coil of the DD pad, L_{2A} is the self-inductance of the second coil of the DD pad and L_{1AB} is the mutual inductance between the two coils as showed in Fig. 2-8.

It is possible compute also the coupling factor by means of the following expression:

$$k_x = \frac{M_x}{\sqrt{L_1 \cdot L_x}} \tag{2.4}$$

where x is 2 for the first coil of the BP pad and 3 for the second coil of the BP pad.

In the Tab. 5 to Tab. 7, are reported the results of the FEM analysis for each case of study.

Tab. 5: Results of FEM analysis for airgap 150 mm

Position x [mm]	Position y [mm]	L_1 [mH]	L_2 [mH]	L_3 [mH]	M_{12} [µH]	M_{13} [µH]	M_{23} [µH]	k_2	k_3
-186	-106	179,07	368,58	332,51	137,20	56,08	21,34	0,534	0,230
-186	-79,5	178,76	360,37	325,36	145,33	55,92	23,81	0,573	0,232
-186	-53	188,52	346,04	323,32	160,02	55,82	29,72	0,627	0,226
-186	-26,5	178,66	402,16	334,99	160,29	73,49	8,35	0,598	0,300
-186	0	182,11	362,44	333,16	157,93	74,05	18,39	0,615	0,301
-186	26,5	223,96	380,98	356,07	162,06	60,24	29,84	0,555	0,213
-186	53	180,47	363,77	335,34	172,88	69,32	35,44	0,675	0,282
-186	79,5	175,72	352,63	329,96	151,23	63,69	28,42	0,608	0,264
-186	106	188,03	351,53	319,28	136,38	51,32	29,63	0,530	0,209
-139,5	-106	179,63	355,90	339,08	159,96	55,72	29,14	0,633	0,226
-139,5	-79,5	198,44	378,19	321,16	180,93	62,04	29,67	0,660	0,246
-139,5	-53	186,16	374,00	329,59	168,56	56,53	28,01	0,639	0,228
-139,5	-26,5	181,46	377,71	329,02	183,93	60,22	28,67	0,703	0,246

-139,5	0	186,93	369,96	344,52	184,82	67,04	19,60	0,703	0,264
-139,5	26,5	198,73	356,69	320,69	200,87	53,00	17,20	0,754	0,210
-139,5	53	189,29	356,70	323,67	171,74	57,59	19,61	0,661	0,233
-139,5	79,5	186,60	379,59	333,84	168,40	58,00	16,76	0,633	0,232
-139,5	106	178,01	370,87	348,90	163,29	53,29	23,83	0,636	0,214
-93	-106	183,66	346,56	324,80	167,37	53,92	21,11	0,663	0,221
-93	-79,5	186,41	367,84	334,93	183,71	56,63	24,05	0,702	0,227
-93	-53	195,44	370,39	324,09	202,50	62,12	10,27	0,753	0,247
-93	-26,5	190,43	369,97	321,46	202,36	68,17	21,07	0,762	0,276
-93	0	187,05	386,18	348,54	199,59	72,78	27,07	0,743	0,285
-93	26,5	196,18	353,41	327,82	211,68	59,35	15,42	0,804	0,234
-93	53	184,50	361,20	338,16	184,23	65,32	24,87	0,714	0,262
-93	79,5	187,16	367,13	328,41	182,93	54,09	22,21	0,698	0,218
-93	106	196,19	359,86	325,80	164,72	53,97	20,63	0,620	0,213
-46,5	-106	191,54	361,26	323,06	153,76	97,66	15,02	0,585	0,393
-46,5	-79,5	193,48	335,06	327,05	175,75	111,46	14,99	0,690	0,443
-46,5	-53	189,47	373,21	351,49	190,82	125,92	11,81	0,718	0,488
-46,5	-26,5	190,85	379,27	338,48	191,12	110,99	5,95	0,710	0,437
-46,5	0	183,97	371,40	359,49	195,39	117,24	14,81	0,747	0,456
-46,5	26,5	185,61	360,52	328,55	185,24	117,13	8,51	0,716	0,474
-46,5	53	184,26	365,91	352,73	180,77	117,67	22,39	0,696	0,462
-46,5	79,5	193,58	353,62	348,35	185,36	109,70	13,76	0,708	0,422
-46,5	106	179,49	363,92	341,63	155,84	103,85	23,18	0,610	0,419
0	-106	180,82	371,50	330,19	138,28	141,14	22,49	0,534	0,578
0	-79,5	191,78	347,50	357,86	149,90	151,09	15,89	0,581	0,577
0	-53	178,06	362,82	332,41	152,73	160,75	18,06	0,601	0,661
0	-26,5	184,86	351,28	335,50	160,08	174,71	13,44	0,628	0,702
0	0	180,46	363,97	331,27	174,57	165,48	16,19	0,681	0,677
0	26,5	176,25	373,49	311,40	157,85	167,79	9,30	0,615	0,716
0	53	190,80	349,78	335,06	159,00	152,84	14,36	0,615	0,604
0	79,5	196,80	400,46	394,43	141,61	167,91	47,49	0,504	0,603
0	106	184,94	346,05	317,18	128,71	134,40	16,70	0,509	0,555
46,5	-106	188,95	329,07	334,32	104,99	160,79	18,27	0,421	0,640
46,5	-79,5	183,50	340,59	339,65	106,74	181,15	19,73	0,427	0,726
46,5	-53	183,85	334,26	360,70	116,10	189,68	18,28	0,468	0,737
46,5	-26,5	182,27	364,23	368,38	120,95	188,98	15,98	0,469	0,729
46,5	0	187,98	368,86	361,45	110,33	193,12	9,76	0,419	0,741
46,5	26,5	183,46	356,52	336,97	118,99	189,05	14,25	0,465	0,760
46,5	53	185,22	354,58	336,06	114,69	204,93	12,67	0,448	0,821
46,5	79,5	187,08	368,46	343,47	109,75	187,59	14,68	0,418	0,740
46,5	106	174,29	358,41	348,29	101,32	154,97	10,88	0,405	0,629
93	-106	184,76	353,10	341,16	51,86	173,96	15,89	0,203	0,693
93	-79,5	180,53	350,96	349,91	62,46	186,61	25,53	0,248	0,742

93	-53	191,36	371,66	337,61	57,83	208,01	15,66	0,217	0,818
93	-26,5	185,57	343,88	340,48	59,87	199,48	12,31	0,237	0,794
93	0	189,02	349,06	349,52	69,16	201,50	23,38	0,269	0,784
93	26,5	183,25	348,95	355,38	66,14	201,48	12,85	0,262	0,790
93	53	190,11	346,30	344,95	64,27	200,33	21,10	0,250	0,782
93	79,5	200,62	350,74	358,66	49,20	186,44	28,92	0,185	0,695
93	106	176,76	349,39	353,61	52,46	183,87	18,41	0,211	0,735
139,5	-106	178,54	375,38	350,31	52,63	158,31	31,81	0,203	0,633
139,5	-79,5	193,92	352,60	375,05	62,87	176,77	16,49	0,240	0,655
139,5	-53	195,93	338,52	341,72	69,41	181,10	19,79	0,269	0,700
139,5	-26,5	179,84	349,81	353,52	67,47	195,06	16,79	0,269	0,774
139,5	0	180,57	336,50	331,57	69,36	190,59	22,86	0,281	0,779
139,5	26,5	180,36	339,34	354,77	64,10	184,30	18,14	0,259	0,729
139,5	53	188,24	371,40	351,40	57,37	177,63	30,16	0,217	0,691
139,5	79,5	176,54	349,29	351,91	66,83	181,04	25,52	0,269	0,726
139,5	106	178,29	365,93	329,64	40,80	155,39	23,56	0,160	0,641
186	-106	190,11	342,32	340,15	48,40	132,23	26,44	0,190	0,520
186	-79,5	187,80	343,90	347,47	54,62	152,85	27,03	0,215	0,598
186	-53	178,46	341,17	363,01	70,61	155,84	24,87	0,286	0,612
186	-26,5	191,55	374,26	348,21	74,71	174,36	15,45	0,279	0,675
186	0	190,99	348,14	346,56	68,72	162,13	21,44	0,266	0,630
186	26,5	182,58	340,99	354,10	74,18	172,84	19,60	0,297	0,680
186	53	180,59	337,25	353,30	63,88	152,96	25,88	0,259	0,606
186	79,5	198,16	337,58	340,25	67,21	156,46	24,62	0,260	0,603
186	106	178,21	364,78	361,98	58,40	132,72	35,46	0,229	0,523

Tab. 6: Results of FEM analysis for airgap 200 mm

Position		**L_1 [mH]**	**L_2 [mH]**	**L_3 [mH]**	**M_{12} [µH]**	**M_{13} [µH]**	**M_{23} [µH]**	**k_2**	**k_3**
x [mm]	**y [mm]**								
-186	-106	172,01	348,02	320,46	96,81	46,88	27,90	0,396	0,200
-186	-79,5	170,39	386,30	386,98	108,09	35,42	34,61	0,421	0,138
-186	-53	181,27	357,25	313,30	123,92	57,49	30,52	0,487	0,241
-186	-26,5	181,66	352,13	312,57	114,79	58,15	30,53	0,454	0,244
-186	0	179,19	333,73	308,79	123,25	55,99	18,48	0,504	0,238
-186	26,5	182,91	350,80	319,31	118,33	46,06	18,74	0,467	0,191
-186	53	192,50	329,68	320,44	123,55	44,42	19,84	0,490	0,179
-186	79,5	177,77	339,96	332,44	117,08	48,40	25,93	0,476	0,199
-186	106	171,65	336,66	332,46	101,69	36,62	21,60	0,423	0,153
-139,5	-106	177,37	340,12	328,85	105,48	39,25	33,48	0,429	0,163
-139,5	-79,5	171,69	347,47	334,20	117,83	45,00	23,18	0,482	0,188
-139,5	-53	178,83	416,58	323,22	130,28	53,15	23,11	0,477	0,221

-139,5	-26,5	185,05	328,31	325,89	128,70	44,51	20,37	0,522	0,181
-139,5	0	168,23	353,17	314,28	137,48	52,83	9,65	0,564	0,230
-139,5	26,5	181,08	330,51	345,25	135,82	50,97	12,41	0,555	0,204
-139,5	53	170,83	346,12	324,13	126,51	46,90	18,96	0,520	0,199
-139,5	79,5	178,79	345,45	345,83	114,55	38,37	30,94	0,461	0,154
-139,5	106	178,01	354,42	332,25	112,64	50,76	28,69	0,448	0,209
-93	-106	186,23	350,62	337,40	117,88	30,13	6,53	0,461	0,120
-93	-79,5	170,42	355,51	325,96	121,43	46,82	27,53	0,493	0,199
-93	-53	175,02	359,78	331,61	122,54	49,73	16,71	0,488	0,206
-93	-26,5	181,22	341,84	328,87	148,93	58,76	20,97	0,598	0,241
-93	0	176,59	353,33	356,16	133,55	55,33	30,70	0,535	0,221
-93	26,5	178,89	333,63	345,96	130,02	53,61	25,51	0,532	0,215
-93	53	183,38	357,01	312,84	122,38	45,81	27,25	0,478	0,191
-93	79,5	172,60	351,45	319,79	123,80	50,59	28,53	0,503	0,215
-93	106	180,93	333,76	321,33	119,05	38,61	20,87	0,484	0,160
-46,5	-106	179,65	355,38	349,76	115,40	62,84	22,54	0,457	0,251
-46,5	-79,5	176,74	356,24	326,91	119,94	72,03	24,61	0,478	0,300
-46,5	-53	173,14	344,37	326,77	129,69	80,42	23,77	0,531	0,338
-46,5	-26,5	182,41	335,12	326,03	124,60	83,83	10,24	0,504	0,344
-46,5	0	170,58	352,79	317,05	131,87	78,84	17,42	0,538	0,339
-46,5	26,5	176,57	373,10	322,70	130,34	76,18	8,28	0,508	0,319
-46,5	53	174,63	348,46	319,66	129,79	76,91	22,56	0,526	0,326
-46,5	79,5	173,43	352,70	331,70	121,19	77,25	23,20	0,490	0,322
-46,5	106	174,61	329,31	312,59	110,75	77,52	26,07	0,462	0,332
0	-106	183,11	356,49	333,10	98,38	98,03	27,88	0,385	0,397
0	-79,5	167,98	364,91	314,77	107,26	96,72	20,63	0,433	0,421
0	-53	169,75	364,98	326,85	106,06	111,61	27,46	0,426	0,474
0	-26,5	180,51	346,92	334,74	115,22	113,62	20,64	0,460	0,462
0	0	168,47	365,35	337,81	111,76	108,18	25,47	0,450	0,453
0	26,5	173,22	334,11	319,49	97,84	108,46	18,98	0,407	0,461
0	53	188,45	339,24	341,38	103,90	104,79	15,33	0,411	0,413
0	79,5	179,81	327,97	331,77	92,35	103,88	23,58	0,380	0,425
0	106	175,59	344,53	330,34	98,29	98,90	30,43	0,400	0,411
46,5	-106	178,95	351,78	316,52	70,22	116,41	20,35	0,280	0,489
46,5	-79,5	180,80	347,54	335,78	75,29	127,90	13,96	0,300	0,519
46,5	-53	173,76	363,44	359,58	77,35	115,54	23,65	0,308	0,462
46,5	-26,5	171,04	353,87	339,21	83,66	128,05	15,91	0,340	0,532
46,5	0	178,45	350,44	337,72	82,53	125,20	11,02	0,330	0,510
46,5	26,5	179,69	358,63	318,66	86,06	129,34	31,08	0,339	0,540
46,5	53	178,40	328,41	343,05	80,25	132,87	17,08	0,332	0,537
46,5	79,5	181,71	332,45	337,04	83,75	117,40	20,83	0,341	0,474
46,5	106	186,23	347,53	343,15	79,28	108,31	23,90	0,312	0,428
93	-106	181,79	339,78	320,98	30,63	120,89	19,28	0,123	0,500

93	-79,5	176,81	352,80	366,58	48,32	130,38	32,16	0,193	0,512
93	-53	168,15	355,40	347,63	49,43	130,39	23,70	0,202	0,539
93	-26,5	177,97	368,31	366,08	50,13	139,00	24,56	0,196	0,545
93	0	175,05	355,73	345,92	45,47	131,62	15,56	0,182	0,535
93	26,5	181,96	350,61	332,65	45,93	130,74	19,74	0,182	0,531
93	53	179,62	337,88	321,58	38,92	135,49	18,73	0,158	0,564
93	79,5	175,03	342,37	324,31	44,17	120,44	33,57	0,180	0,506
93	106	164,38	340,71	333,18	50,39	129,08	31,35	0,213	0,552
139,5	-106	176,58	347,88	317,07	41,83	114,74	23,11	0,169	0,485
139,5	-79,5	175,86	356,01	336,83	42,89	113,93	18,57	0,171	0,468
139,5	-53	176,91	372,00	341,50	43,22	119,79	22,99	0,168	0,487
139,5	-26,5	178,26	361,90	348,89	54,50	131,98	15,28	0,215	0,529
139,5	0	171,54	367,34	317,47	53,77	138,24	4,32	0,214	0,592
139,5	26,5	170,43	343,73	343,51	50,33	130,63	18,91	0,208	0,540
139,5	53	190,13	322,54	334,91	45,65	118,76	22,48	0,184	0,471
139,5	79,5	171,30	329,59	330,66	53,27	122,40	23,82	0,224	0,514
139,5	106	178,25	345,19	338,80	32,74	108,17	24,92	0,132	0,440
186	-106	176,94	368,98	348,71	43,33	94,29	30,51	0,170	0,380
186	-79,5	180,93	380,18	366,64	40,79	107,54	29,91	0,156	0,418
186	-53	177,88	354,55	311,07	55,31	117,76	23,95	0,220	0,501
186	-26,5	184,58	342,07	324,68	52,95	116,85	19,57	0,211	0,477
186	0	187,69	348,98	332,72	39,94	102,59	20,98	0,156	0,411
186	26,5	177,07	327,73	338,08	54,33	116,40	23,94	0,226	0,476
186	53	185,67	334,04	342,11	38,89	107,83	27,28	0,156	0,428
186	79,5	178,08	334,84	343,18	40,06	103,57	23,74	0,164	0,419
186	106	179,56	319,20	328,14	35,42	99,13	20,26	0,148	0,408

Tab. 7: Results of FEM analysis for airgap 250 mm

Position		**L_1 [mH]**	**L_2 [mH]**	**L_3 [mH]**	**M_{12} [µH]**	**M_{13} [µH]**	**M_{23} [µH]**	**k_2**	**k_3**
x [mm]	**y [mm]**								
-186	-106	181,06	340,92	312,87	75,85	30,21	26,82	0,305	0,127
-186	-79,5	179,95	349,04	316,70	89,39	43,72	31,90	0,357	0,183
-186	-53	174,10	338,13	306,43	93,05	40,99	21,79	0,384	0,177
-186	-26,5	172,23	351,78	331,83	80,35	32,39	34,05	0,326	0,135
-186	0	197,31	327,19	304,86	91,73	34,13	27,96	0,361	0,139
-186	26,5	176,73	365,30	319,64	80,61	38,95	25,19	0,317	0,164
-186	53	170,38	381,90	314,29	88,30	39,38	25,07	0,346	0,170
-186	79,5	184,85	345,01	306,71	87,84	38,86	23,28	0,348	0,163
-186	106	173,13	349,89	324,96	74,89	44,91	18,94	0,304	0,189
-139,5	-106	167,26	405,25	343,03	90,62	41,42	33,89	0,348	0,173
-139,5	-79,5	173,80	373,85	315,58	91,43	36,49	20,99	0,359	0,156

-139,5	-53	170,01	344,35	319,55	92,58	37,10	33,57	0,383	0,159
-139,5	-26,5	182,13	326,90	326,33	83,76	38,66	26,08	0,343	0,159
-139,5	0	174,37	344,74	316,90	95,03	36,08	21,29	0,388	0,154
-139,5	26,5	171,46	335,93	312,73	97,04	47,98	16,04	0,404	0,207
-139,5	53	182,99	347,36	326,53	98,93	48,99	21,63	0,392	0,200
-139,5	79,5	174,12	373,66	343,90	91,66	38,86	29,74	0,359	0,159
-139,5	106	178,33	376,71	342,57	76,85	31,08	35,60	0,296	0,126
-93	-106	181,74	339,82	312,77	84,69	37,49	21,87	0,341	0,157
-93	-79,5	182,68	358,17	340,78	91,79	30,68	34,32	0,359	0,123
-93	-53	173,62	361,98	323,15	99,53	38,67	42,87	0,397	0,163
-93	-26,5	174,06	344,39	314,24	86,89	39,24	30,49	0,355	0,168
-93	0	182,88	356,61	323,74	106,04	34,82	15,45	0,415	0,143
-93	26,5	169,28	346,84	316,16	104,49	39,33	29,47	0,431	0,170
-93	53	170,07	347,47	307,14	84,23	36,60	22,29	0,346	0,160
-93	79,5	171,51	339,22	323,47	84,94	36,80	27,19	0,352	0,156
-93	106	178,99	358,39	324,25	85,98	35,04	24,17	0,339	0,145
-46,5	-106	168,01	364,37	328,95	81,96	45,33	31,72	0,331	0,193
-46,5	-79,5	185,71	337,61	355,16	95,52	53,41	25,34	0,381	0,208
-46,5	-53	168,79	353,74	324,71	87,38	53,85	30,51	0,358	0,230
-46,5	-26,5	176,02	373,03	337,44	84,72	69,77	19,04	0,331	0,286
-46,5	0	164,81	347,36	351,03	92,52	50,79	18,03	0,387	0,211
-46,5	26,5	176,83	329,83	327,95	92,54	61,58	16,94	0,383	0,256
-46,5	53	190,47	353,76	314,72	92,50	57,60	20,82	0,356	0,235
-46,5	79,5	206,22	351,36	315,86	90,71	54,72	17,36	0,337	0,214
-46,5	106	170,06	344,95	320,33	72,08	47,45	31,38	0,298	0,203
0	-106	187,32	329,66	317,25	79,95	60,98	22,03	0,322	0,250
0	-79,5	174,20	327,47	313,67	76,41	66,54	16,77	0,320	0,285
0	-53	175,39	358,02	323,67	77,64	80,87	23,82	0,310	0,339
0	-26,5	178,39	375,62	306,84	62,97	83,35	18,47	0,243	0,356
0	0	185,16	345,53	332,41	71,97	76,02	20,79	0,285	0,306
0	26,5	171,18	350,30	314,38	76,88	79,96	29,02	0,314	0,345
0	53	178,43	343,18	332,45	69,09	70,80	25,98	0,279	0,291
0	79,5	172,55	354,94	330,81	68,14	71,01	28,89	0,275	0,297
0	106	175,36	339,79	317,22	65,81	69,28	21,99	0,270	0,294
46,5	-106	167,46	351,21	313,17	48,70	79,31	33,37	0,201	0,346
46,5	-79,5	171,36	352,34	327,58	55,20	81,52	35,08	0,225	0,344
46,5	-53	181,86	350,61	330,73	55,25	92,66	29,16	0,219	0,378
46,5	-26,5	179,80	328,07	333,33	55,05	94,44	36,48	0,227	0,386
46,5	0	186,09	335,03	325,82	45,77	88,44	19,19	0,183	0,359
46,5	26,5	171,14	335,17	309,82	52,49	87,54	13,87	0,219	0,380
46,5	53	165,43	326,65	320,98	57,33	84,98	19,48	0,247	0,369
46,5	79,5	182,25	331,47	308,01	57,12	76,44	17,99	0,232	0,323
46,5	106	175,43	330,53	316,29	52,64	79,68	22,12	0,219	0,338

93	-106	169,36	346,90	327,23	33,65	86,35	19,98	0,139	0,367
93	-79,5	175,11	333,16	335,81	35,90	85,32	21,81	0,149	0,352
93	-53	167,41	335,50	337,50	38,98	93,84	22,16	0,164	0,395
93	-26,5	171,25	334,33	315,40	41,23	100,84	28,23	0,172	0,434
93	0	183,44	343,05	333,01	38,29	94,44	26,10	0,153	0,382
93	26,5	178,68	354,77	334,75	37,23	99,48	22,79	0,148	0,407
93	53	180,53	360,11	336,90	30,56	85,99	22,21	0,120	0,349
93	79,5	173,98	330,95	326,90	27,33	93,39	20,39	0,114	0,392
93	106	171,97	339,94	316,84	37,53	82,37	23,37	0,155	0,353
139,5	-106	173,98	348,77	332,72	38,23	90,72	27,92	0,155	0,377
139,5	-79,5	179,41	339,45	335,17	32,84	87,79	20,83	0,133	0,358
139,5	-53	168,73	341,93	333,45	36,42	92,77	17,34	0,152	0,391
139,5	-26,5	185,55	329,84	322,01	41,25	92,91	15,55	0,167	0,380
139,5	0	171,25	335,13	333,44	40,90	95,99	19,00	0,171	0,402
139,5	26,5	187,41	331,99	340,73	29,76	87,11	26,62	0,119	0,345
139,5	53	184,27	341,24	326,22	37,05	96,24	27,54	0,148	0,393
139,5	79,5	171,58	343,72	344,06	41,45	99,49	28,70	0,171	0,409
139,5	106	180,33	335,18	324,69	35,80	85,58	21,95	0,146	0,354
186	-106	180,74	344,28	337,66	36,83	64,79	25,17	0,148	0,262
186	-79,5	171,65	336,38	323,98	42,76	86,74	21,19	0,178	0,368
186	-53	170,61	360,51	322,48	38,52	82,03	20,44	0,155	0,350
186	-26,5	169,29	359,52	333,21	39,68	80,45	20,44	0,161	0,339
186	0	197,32	339,48	357,63	36,36	85,06	33,67	0,140	0,320
186	26,5	199,04	330,64	316,34	46,33	87,38	25,05	0,181	0,348
186	53	176,48	331,70	305,40	38,43	90,90	19,02	0,159	0,392
186	79,5	177,62	370,90	322,20	33,45	87,80	22,09	0,130	0,367
186	106	178,62	342,85	351,89	34,68	74,68	39,45	0,140	0,298

From results of above shown tables, it can be easily noted that the magnetic coupling of the system is higher for low values of the air gap and that there is little difference between the parameters of coil 2 and 3 that constitute the BP pad, although the geometry of the coils seems to be the same, because as mentioned in previous chapter, the two coils are overlapped, therefore the air gap from the primary coil is not exactly the same for the two coils of the bipolar pad.

The following figures Fig. 2-9 to Fig. 2-13, show with an air gap of 200 mm, the trends of the self and mutual inductance of the IPT system (L_1, L_2, L_3, M_{12}, M_{13}) in function of the possible x, y misalignments. It can be noted that the primary self-inductance is almost half of the secondary self-inductance because, as reported in previous chapter, the DD coils are connected electrically in parallel. This allows to reduce the input reactive power.

In Fig. 2-9 to Fig. 2-11, it can be pointed out that the values of self-inductances L_1, L_2 and L_3, have little variations with respect to the lateral misalignments between PADs, because the leakage inductance is higher than the magnetic inductance.

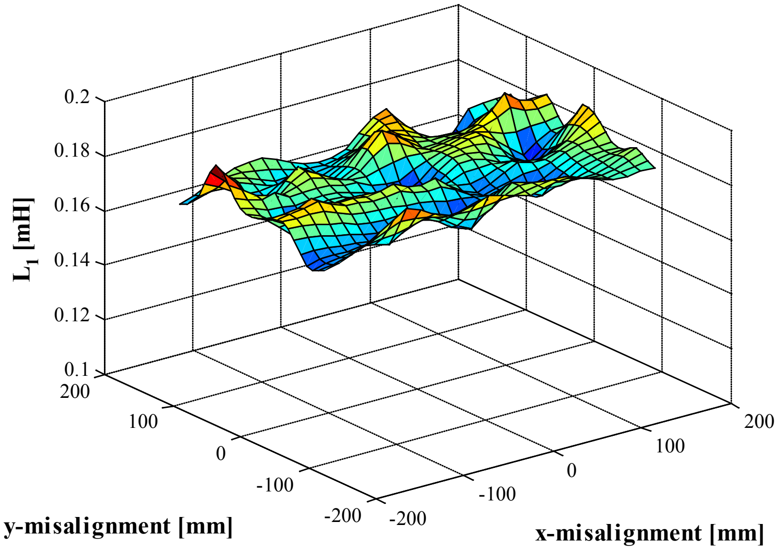

Fig. 2-9: Primary self-inductance L_1

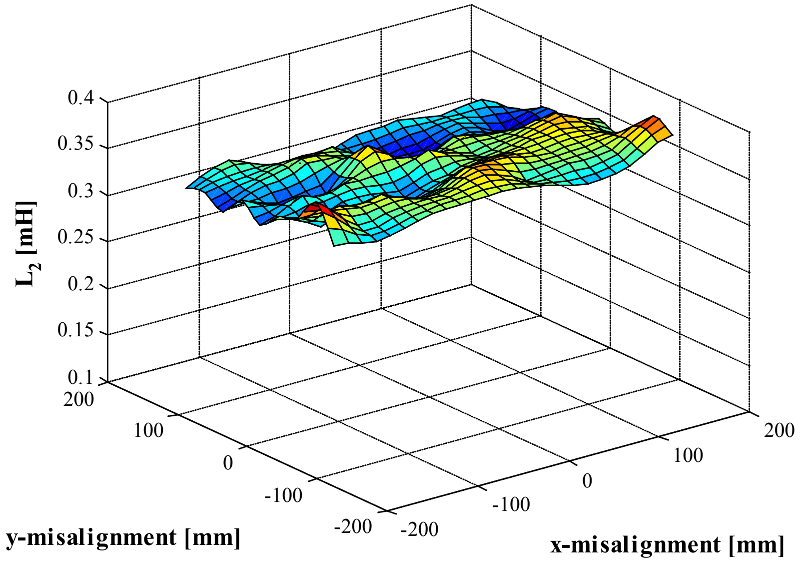

Fig. 2-10: Secondary self-inductance L_2

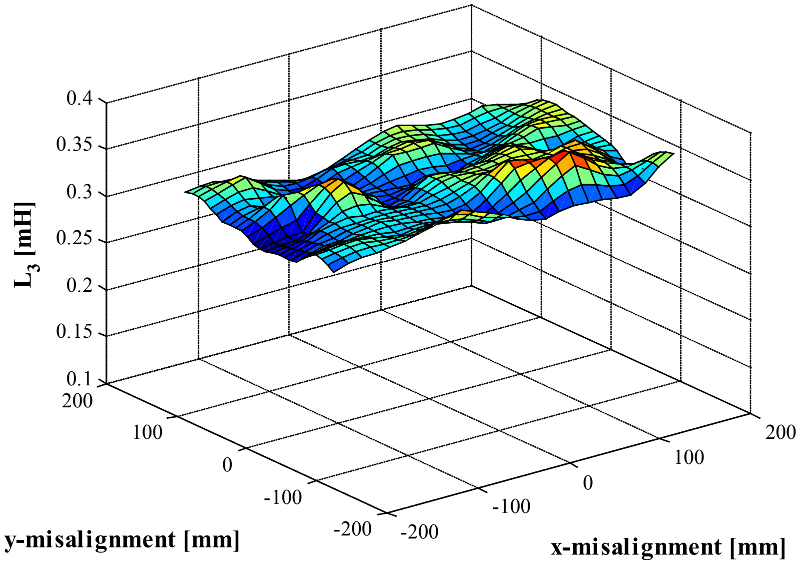

Fig. 2-11: Secondary self-inductance L_3

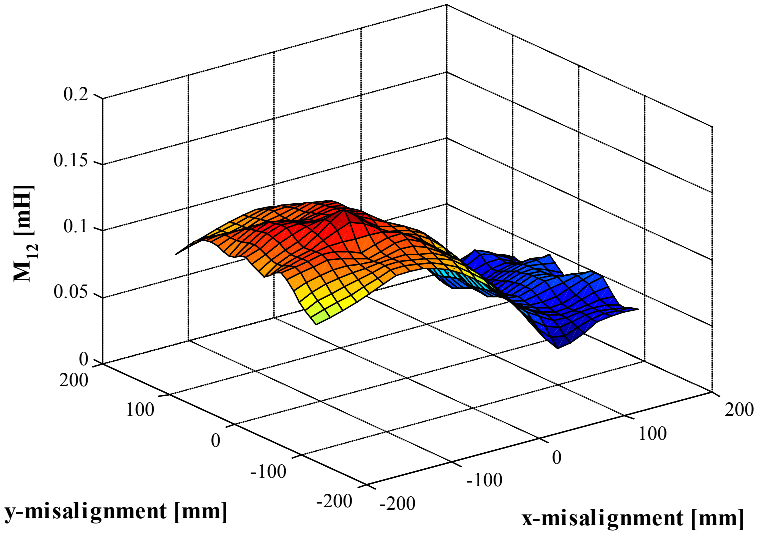

Fig. 2-12: Mutual inductance M_{12}

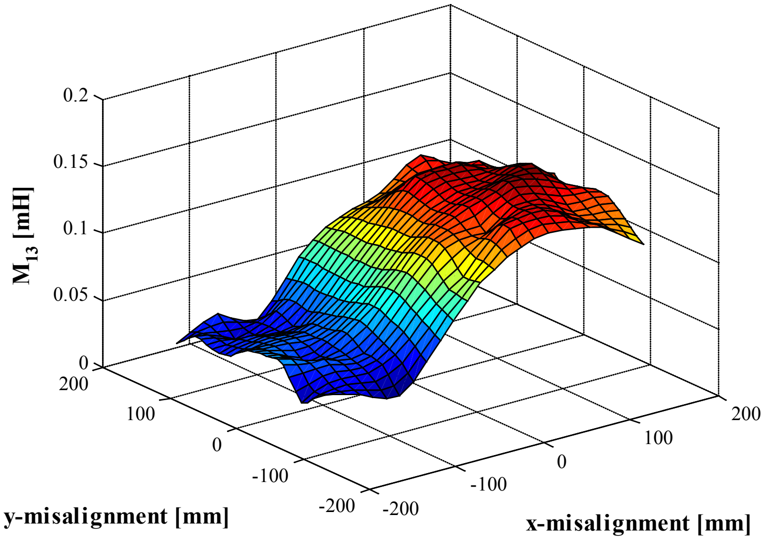

Fig. 2-13: Mutual inductance M_{13}

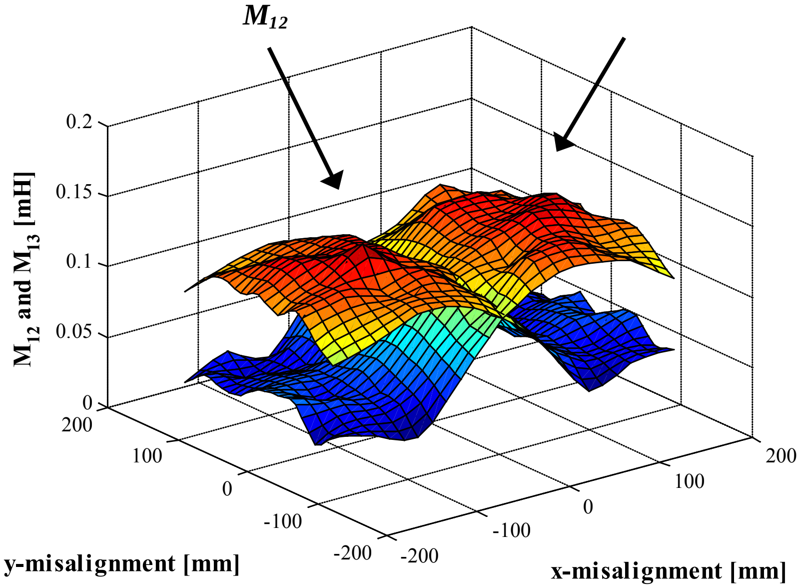

Fig. 2-14: Comparison between M_{12} and M_{13}

In Fig. 2-12 and Fig. 2-13, it can be pointed out that the values of single mutual inductance have high variations along x misalignments, but if the behavior of the overall coupled system is considered, it has low variation along x misalignments around the center position. In fact, as shown in Fig. 2-14, if the value of x misalignment increase from central position, at a reduction of mutual inductance M_{12} corresponds an increase of mutual inductance M_{13} and vice-versa. Instead they have symmetrical behaviors along y misalignments.

2.2.3 Compensation

As explained in previous chapter, in order to compensate leakage inductance and thus the reactive power seen from the power supply connected to the primary side, it is necessary to use capacitors connected both at the primary and secondary coils, in order to ensure operation at power factor close to unity. For the capacitive compensation design, it is important to follow a procedure. The magnetic coupler constituted by DD and BP pad can be represented through the electric circuit shown in Fig. 2-15. In the circuit, L_1-L_3 represent the self-inductance, R_1-R_3 represent the coil resistance, C_1-C_3 represent the parallel capacitor compensation and v_{ref}-v_2-v_3 represent the open circuit voltage.

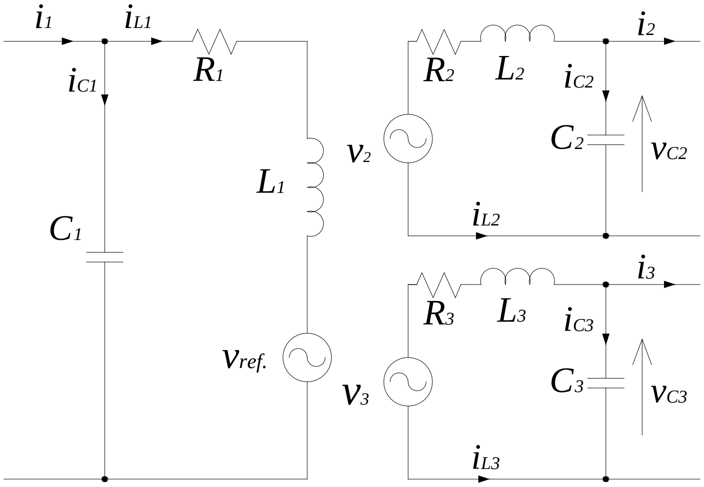

Fig. 2-15: electric circuit of magnetic coupler

2.2.3.1 Secondary coil

The first step of the compensation, is to calculate the value of capacitor for the secondary compensation C_2 (it is the same for C_3). From resonance theory, the secondary compensation will be established under the condition of follow equation:

$$j\omega_0 L_2 - j\frac{1}{\omega_0 C_2} = 0 \tag{2.5}$$

$$C_2 = \frac{1}{\omega_0^2 L_2} = \frac{1}{\omega_0^2 \left(L_{2\sigma} + M_{12}\right)} \tag{2.6}$$

where:

ω_0 is the resonant angular frequency

L_2 is the secondary coil 2 self inductance

C_2 is the secondary coil 2 capacitance

In practice, the value of L_2 is fixed, therefore, the value of C_2, depends on the resonant frequency. In our case, with an operating frequency of 20 kHz, designing the compensation at a airgap of 200 mm in condition of null misalignment, we obtain:

$$C_2 = \frac{1}{\omega_0^2 L_2} = \frac{1}{\left(2\pi \cdot 20e^3\right)^2 365.35e^{-6}} = 0.173e^{-6}[\mathrm{F}] \tag{2.7}$$

$$C_3 = \frac{1}{\omega_0^2 L_3} = \frac{1}{\left(2\pi \cdot 20e^3\right)^2 337.81e^{-6}} = 0.187e^{-6}[\mathrm{F}] \tag{2.8}$$

2.2.3.2 Primary coil

The second step in the capacitive compensation design is to calculate the value of the primary capacitance C_1. Depending on each compensation topology, the equation for C_1 will vary [5]. The value calculation of capacitor for the primary compensation, has been done following the consideration of [6], where the primary inductance observed at the terminals of the primary pad is given by:

$$L_{1-eff} = L_1\left(1 - k_2^2 - k_3^2\right) = 99.63e^{-6}[H] \tag{2.9}$$

$$C_1 = \frac{1}{\omega_0^2 L_{1-eff}} = \frac{1}{\left(2\pi \cdot 20e^3\right)^2 99.63e^{-6}} = 0.636e^{-6}[\mathrm{F}] \tag{2.10}$$

2.2.4 DC/DC Pick Up Converter

In order to supply the load on board of the pickup, generally a battery pack, it is necessary adapt the rectifier output voltage at the voltage value required by load. The rectifier output voltage depends from several factors, among these the coupling factor has a strong impact. Therefore, this value may be higher or lower of the value required by load. To overcome thus, we use a buck boost DC/DC converter topology as shown in Fig. 2-16.

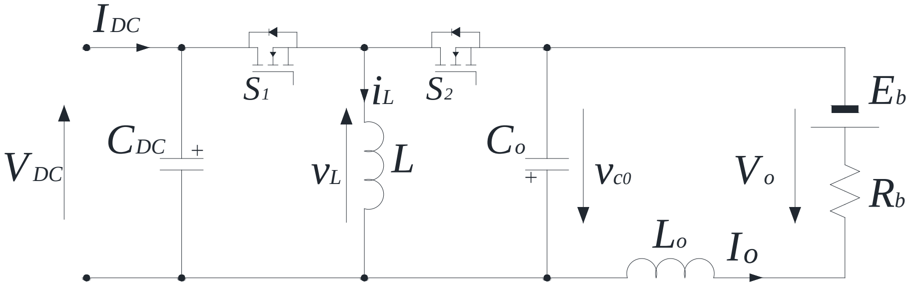

Fig. 2-16: buck boost converter

In order to have an output current with a low ripple has been added a L_oC_o filter tuned with frequency switching. The design of this filter will be into account in the chapter on the control.

2.3 Mathematical Model

After have chosen the electromagnetic configuration of the magnetic coupler, the circuit compensation and the power converters topology, the work has been focused on the developing of the mathematical model of the overall system. In particular, the goal is obtained a state space formulation representing the current, voltage and induction power transfer behavior for analysis and control purposes. In the development of a complex technology such as this it become impossible to design and work with a circuit constructed of wire, ferrite, airgap, and electronics components so an electric equivalent circuit have to be took in consideration. In the Fig. 2-17 is shown the electric circuit that represent the whole IPT system.

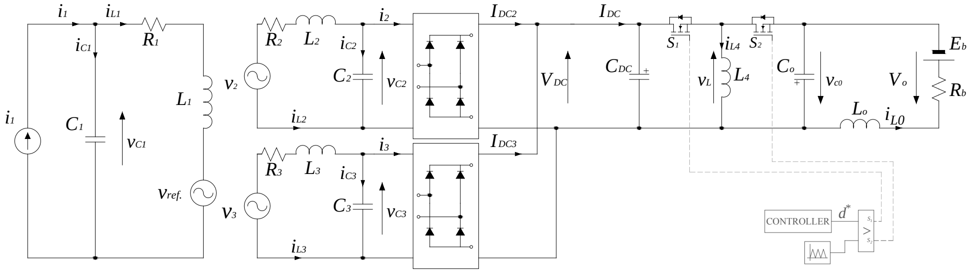

Fig. 2-17: IPT equivalent circuit

In this circuit the power supply it has been represented by a sinusoidal current generator that work at 20 kHz. The ac side of this circuit operates at 20 kHz, whereas the dc side operates at 1 kHz that is the switch frequency of the buck boost converter.

The power supply drives a sinusoidal current I_1 in the coil of the transmitter pad that is compensated by mean of the primary capacitor C_1. In the two independents coils of the receiver pad will be induced a voltage, respectively V_2 and V_3. These coils are compensated by means of the capacitors C_2 and C_3. The output current of the two coils of the receiver pad are connected at two different rectifiers, which have the output connected in parallel. The DC output of the two rectifiers is input of the buck boost DC/DC converter that supply the battery.

In order to write the mathematical model, the electrical circuit reported in Fig. 2-17, can be splitted into two parts, AC and DC side, as shown in the Fig. 2-18 and Fig. 2-19.

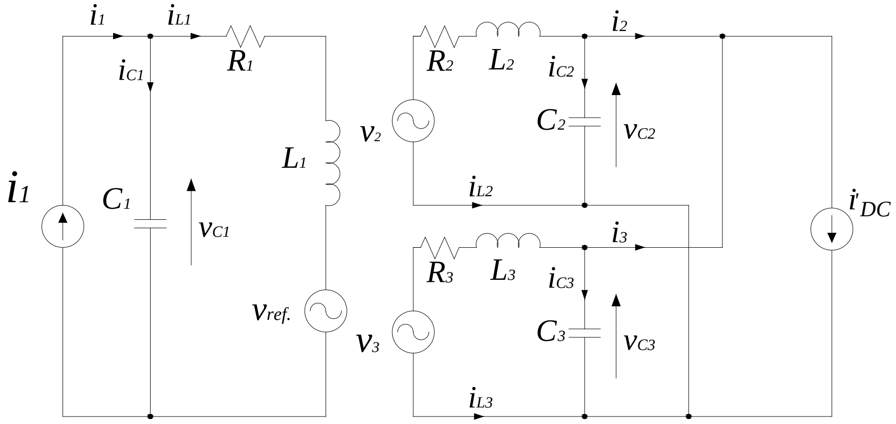

Fig. 2-18: AC side

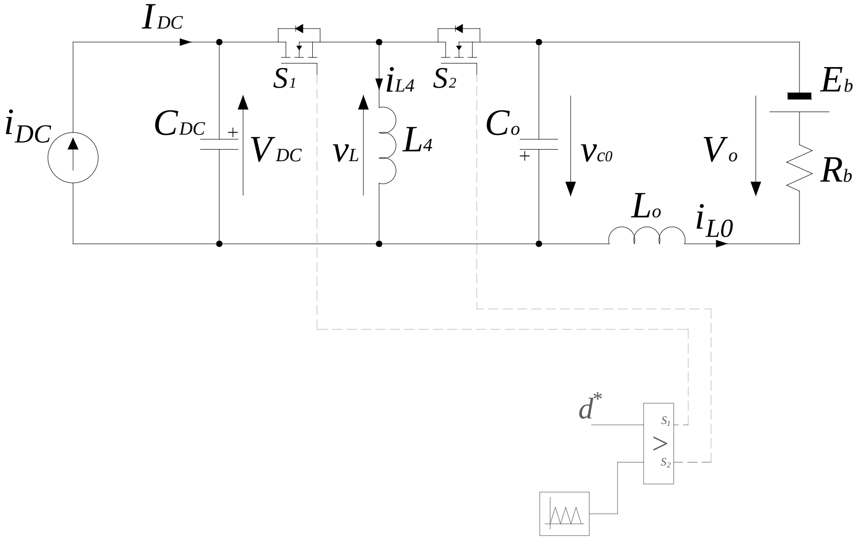

Fig. 2-19: DC side

The separation between AC and DC side it may possible because the operating frequency of two side is very different.

The link between the two circuit, or between i_{dc} and i'_{dc} is obtained by means of the following expression:

$$i_{DC} = \frac{\pi}{2\sqrt{2}} i'_{DC\_rms} = \frac{\pi}{2\sqrt{2}} \frac{i'_{DC\_\max}}{\sqrt{2}} = \frac{\pi}{4} i'_{DC\_\max} = f_{RI} i'_{DC\_\max} \qquad (2.11)$$

$$V_{DC} = \frac{2\sqrt{2}}{\pi} V_{AC\_rms} = \frac{2\sqrt{2}}{\pi} \frac{V_{AC\_\max}}{\sqrt{2}} = \frac{2}{\pi} V_{AC\_\max} = \frac{V_{AC\_\max}}{f_{RV}} \qquad (2.12)$$

These relations are valid if the DC currents to the load are considered continuous and the system frequency stays essentially constant at the resonance frequency, as explained in [7].

2.3.1 AC Side

The aim is to identify a set of equations which describes, with a good approximation, the system behavior of the electric circuit of Fig. 2-18. So, it is possible to write the equation in time domain as:

$$\begin{cases} -i_{L1} - C_1 \dfrac{dv_1}{dt} + i_1 = 0 \\ -R_1 i_{L1} - L_1 \dfrac{di_{L1}}{dt} - M_{21} \dfrac{di_{L2}}{dt} - M_{31} \dfrac{di_{L3}}{dt} + v_{C1} = 0 \\ M_{12} \dfrac{di_{L1}}{dt} + R_2 i_{L2} + L_2 \dfrac{di_{L2}}{dt} + M_{32} \dfrac{di_{L3}}{dt} - v_{C2} = 0 \\ M_{13} \dfrac{di_{L1}}{dt} + M_{23} \dfrac{di_{L2}}{dt} + R_3 i_{L3} + L_3 \dfrac{di_{L3}}{dt} - v_{C2} = 0 \\ i_{L2} + i_{L3} + \left(C_2 + C_3\right) \dfrac{dv_{C2}}{dt} + i_{DC}' = 0 \end{cases} \tag{2.13}$$

Deriving the last three equations can be write:

$$\begin{cases} \dot{v}_{C1} = -\dfrac{i_{L1}}{C_1} + \dfrac{i_1}{C_1} \\ \dot{v}_{C2} = -\dfrac{i_{L2}}{C_{23}} - \dfrac{i_{L3}}{C_{23}} - \dfrac{i_{DC}'}{C_{23}} \\ M_{13} \ddot{i}_{L1} + M_{23} \ddot{i}_{L2} + R_3 \dot{i}_{L3} + L_3 \ddot{i}_{L3} - \dot{v}_{C2} = 0 \\ M_{12} \ddot{i}_{L1} + R_2 \dot{i}_{L2} + L_2 \ddot{i}_{L2} + M_{32} \ddot{i}_{L3} - \dot{v}_{C2} = 0 \\ -R_1 \dot{i}_{L1} - L_1 \ddot{i}_{L1} - M_{21} \ddot{i}_{L2} - M_{31} \ddot{i}_{L3} + \dot{v}_{C1} = 0 \end{cases} \tag{2.14}$$

and substituting the first two in the last three can be written:

$$\begin{cases} M_{13}\ddot{i}_{L1} + M_{23}\ddot{i}_{L2} + R_3\dot{i}_{L3} + L_3\ddot{i}_{L3} + \dfrac{i_{L2}}{C_{23}} + \dfrac{i_{L3}}{C_{23}} + \dfrac{i'_{DC}}{C_{23}} = 0 \\ M_{12}\ddot{i}_{L1} + R_2\dot{i}_{L2} + L_2\ddot{i}_{L2} + M_{32}\ddot{i}_{L3} + \dfrac{i_{L2}}{C_{23}} + \dfrac{i_{L3}}{C_{23}} + \dfrac{i'_{DC}}{C_{23}} = 0 \\ -R_1\dot{i}_{L1} - L_1\ddot{i}_{L1} - M_{21}\ddot{i}_{L2} - M_{31}\ddot{i}_{L3} - \dfrac{i_{L1}}{C_1} + \dfrac{i_1}{C_1} = 0 \end{cases} \tag{2.15}$$

Now deriving all the equation can be written:

$$\begin{cases} M_{13}\dddot{i}_{L1} + M_{23}\dddot{i}_{L2} + R_3\ddot{i}_{L3} + L_3\dddot{i}_{L3} + \dfrac{\dot{i}_{L2}}{C_{23}} + \dfrac{\dot{i}_{L3}}{C_{23}} + \dfrac{\dot{i}'_{DC}}{C_{23}} = 0 \\ M_{12}\dddot{i}_{L1} + R_2\ddot{i}_{L2} + L_2\dddot{i}_{L2} + M_{32}\dddot{i}_{L3} + \dfrac{\dot{i}_{L2}}{C_{23}} + \dfrac{\dot{i}_{L3}}{C_{23}} + \dfrac{\dot{i}'_{DC}}{C_{23}} = 0 \\ -R_1\ddot{i}_{L1} - L_1\dddot{i}_{L1} - M_{21}\dddot{i}_{L2} - M_{31}\dddot{i}_{L3} - \dfrac{\dot{i}_{L1}}{C_1} + \dfrac{\dot{i}_1}{C_1} = 0 \end{cases} \tag{2.16}$$

The above equations can be written in matrix form:

$$P\dot{x} = Q \cdot x + R \cdot u \tag{2.17}$$

where:

$$x = \begin{bmatrix} \dot{i}_{L1} \\ \ddot{i}_{L1} \\ \dot{i}_{L2} \\ \ddot{i}_{L2} \\ \dot{i}_{L3} \\ \ddot{i}_{L3} \end{bmatrix} \tag{2.18}$$

$$\dot{x} = \begin{bmatrix} \ddot{i}_{L1} \\ \dddot{i}_{L1} \\ \ddot{i}_{L2} \\ \dddot{i}_{L2} \\ \ddot{i}_{L3} \\ \dddot{i}_{L3} \end{bmatrix} \tag{2.19}$$

$$u = \begin{bmatrix} \dot{i}_{1} \\ \dot{i}_{DC}^{'} \end{bmatrix} \tag{2.20}$$

$$P = \begin{bmatrix} 1 & 0 & 0 & 0 & 0 & 0 \\ 0 & M_{13} & 0 & M_{23} & R_3 & L_3 \\ 0 & 0 & 1 & 0 & 0 & 0 \\ 0 & M_{12} & R_2 & L_2 & 0 & M_{32} \\ 0 & 0 & 0 & 0 & 1 & 0 \\ -R_1 & -L_1 & 0 & -M_{21} & 0 & -M_{31} \end{bmatrix} \tag{2.21}$$

$$Q=\begin{bmatrix} 0 & 1 & 0 & 0 & 0 & 0 \\ 0 & 0 & -1/C_{23} & 0 & -1/C_{23} & 0 \\ 0 & 0 & 0 & 1 & 0 & 0 \\ 0 & 0 & -1/C_{23} & 0 & -1/C_{23} & 0 \\ 0 & 0 & 0 & 0 & 0 & 1 \\ 1/C_1 & 0 & 0 & 0 & 0 & 0 \end{bmatrix} \tag{2.22}$$

$$R=\begin{bmatrix} 0 & 0 \\ 0 & -\frac{1}{C_{23}} \\ 0 & 0 \\ 0 & -\frac{1}{C_{23}} \\ 0 & 0 \\ \frac{1}{C_1} & 0 \end{bmatrix} \tag{2.23}$$

The main parameters of the electric circuit shown in Fig. 2-18, are reported in Tab. 8.

Tab. 8: Circuit parameters for an airgap of 200 mm and null misalignment

L_1 [µH]	L2 [µH]	L_3 [µH]	K_2	K_3	M_2 [µH]	M_3 [µH]	$M_{23=32}$ [µH]	C_1 [µF]	C_2 [µF]	C_3 [µF]
168.47	365.35	337.81	0.450	0.453	111.76	108.18	25.47	0.636	0.173	0.187

2.3.2 DC Side

Since the electric circuit of Fig. 2-19, the equations of the DC side circuit, averaged in the period of commutation can be written as:

$$\begin{cases} i_{DC} - C_{DC}\dfrac{dv_{DC}}{dt} + i_{L4}\cdot d = 0 \\ L_4\dfrac{di_{L4}}{dt} - d\cdot v_{DC} + \left(1-d\right)v_{C0} = 0 \\ L_0\dfrac{di_{L0}}{dt} - v_{C0} + R_b i_{L0} + E_b = 0 \\ C_0\dfrac{dv_{C0}}{dt} + i_{L0} - \left(1-d\right)i_{L4} = 0 \end{cases} \tag{2.24}$$

Following the [8], to study the small signal behavior, the time varying system described in (2.24), can be linearized using small signal perturbation techniques. Using this technique, the inputs are assumed to vary around a steady-state operating point. Taking a first order Fourier series approximation, the inputs are represented by the sum of a DC or steady-state term and an AC variation or sinusoidal term. Introducing variations in the input current and duty cycle of DC-DC converter by the following substitutions

$$\begin{aligned} i_{DC} &= I_{DC} + \hat{i}_{DC} \\ d &= D + \hat{d} \end{aligned} \tag{2.25}$$

cause perturbations in the state and output, as shown below. In the above and following equations, the variables in capital letters represent the DC or steady-state term; and the variables with the symbol ^ above them represent the AC variation or sinusoidal term.

$$\begin{aligned} v_{DC} &= V_{DC} + \hat{v}_{DC} \\ v_{C0} &= V_{C0} + \hat{v}_{C0} \\ i_{L0} &= I_{L0} + \hat{i}_{L0} \\ i_{L4} &= I_{L4} + \hat{i}_{L4} \end{aligned} \tag{2.26}$$

The derivate of a DC term is zero, so can be written:

$$\begin{aligned} v_{DC} &= V_{DC} + \hat{v}_{DC} & \dot{v}_{DC} &= \dot{\hat{v}}_{DC} \\ v_{C0} &= V_{C0} + \hat{v}_{C0} & \dot{v}_{C0} &= \dot{\hat{v}}_{C0} \\ i_{L0} &= I_{L0} + \hat{i}_{L0} & \dot{i}_{L0} &= \dot{\hat{i}}_{L0} \\ i_{L4} &= I_{L4} + \hat{i}_{L4} & \dot{i}_{L4} &= \dot{\hat{i}}_{L4} \end{aligned} \tag{2.27}$$

Substituting these equations (2.24), and neglecting the second order ac terms because they are much smaller than the first order terms, results in the following:

$$\begin{cases} I_{DC} + \hat{i}_{DC} - C_{DC}\dfrac{d\hat{v}_{DC}}{dt} + I_{L4}d + \hat{i}_{L4}D + I_{L4}D = 0 \\ L_4\dfrac{d\hat{i}_{L4}}{dt} - \hat{d}\cdot V_{DC} - D\cdot\hat{v}_{C2} + \hat{v}_{C0} - \hat{d}\cdot V_{C0} - D\cdot\hat{v}_{C0} - D\cdot V_{DC} - D\cdot V_{C0} + V_{C0} = 0 \\ L_0\dfrac{d\hat{i}_{L0}}{dt} - \hat{v}_{C0} + R_b\hat{i}_{L0} - V_{C0} + E_b + R_b I_{L0} = 0 \\ C_0\dfrac{d\hat{v}_{C0}}{dt} + \hat{i}_{L0} - \hat{i}_{L4} - \hat{i}_{L4}\cdot D + \hat{d}\cdot I_{L4} + I_{L4} - I_{L4}\cdot D + I_{L0} = 0 \end{cases} \tag{2.28}$$

Separating the DC (steady-state) terms and the AC (sinusoidal) terms, results in the following:

$$\begin{cases} I_{DC} + I_{L4} D = 0 \\ -DV_{DC} - DV_{C0} + V_{C0} = 0 \\ -V_{C0} + E_b + R_b I_{L0} = 0 \\ I_{L4} - I_{L4} D + I_{L0} = 0 \end{cases} \tag{2.29}$$

$$\begin{cases} \hat{i}_{DC} - C_{DC} \dfrac{d\hat{v}_{DC}}{dt} + I_{L4} \cdot \hat{d} + \hat{i}_{L4} \cdot D = 0 \\ L_4 \dfrac{d\hat{i}_{L4}}{dt} - \hat{d} \cdot V_{DC} - D \cdot \hat{v}_{DC} + \hat{v}_{C0} - \hat{d} \cdot V_{C0} - D \cdot \hat{v}_{C0} = 0 \\ L_0 \dfrac{d\hat{i}_{L0}}{dt} - \hat{v}_{C0} + R_b \hat{i}_{L0} = 0 \\ C_0 \dfrac{d\hat{v}_{C0}}{dt} + \hat{i}_{L0} - \hat{i}_{L4} - \hat{i}_{L4} \cdot D + \hat{d} \cdot I_{L4} = 0 \end{cases} \tag{2.30}$$

In the (2.29), and (2.30), are reported the linearized small signal equation which describes the buck boost converter.

2.3.2.1 Steady State Analysis

Provided that the natural frequencies of the converter, as well as the frequencies of variations of the converter inputs, are much slower than the switching frequency, then the state space averaged model that describes the converter in equilibrium can be written as:

$$0 = A \cdot X + B \cdot U \tag{2.31}$$

where

$$X = \begin{bmatrix} V_{DC} \\ V_{Co} \\ I_{L4} \\ I_{Lo} \end{bmatrix} \tag{2.32}$$

$$A = \begin{bmatrix} 0 & 0 & D & 0 \\ -D & (1-D) & 0 & 0 \\ 0 & -1 & 0 & R_b \\ 0 & 0 & (1-D) & 1 \end{bmatrix} \tag{2.33}$$

$$B = \begin{bmatrix} 1 & 0 \\ 0 & 0 \\ 0 & 1 \\ 0 & 0 \end{bmatrix} \tag{2.34}$$

$$U = \begin{bmatrix} I_{DC} \\ E_b \end{bmatrix} \tag{2.35}$$

$$R = \begin{bmatrix} 1 & 0 \\ 0 & 0 \\ 0 & 0 \\ 0 & -1 \end{bmatrix} \tag{2.36}$$

$$u = \begin{bmatrix} i_{DC} \\ E_b \end{bmatrix} \tag{2.37}$$

2.3.2.2 Small Signal Analysis

The converter contains two inputs, the duty cycle $\hat{d}$ and the input current $\hat{i}_{DC}$ and one output $\hat{i}_0$. Hence, the ac output current variations can be expressed as the superposition of terms arising from two inputs:

$$\hat{i}_o(s) = G_d(s)\cdot\hat{d}(s) + G_{i_{dc}}(s)\cdot\hat{i}_{dc}(s) \tag{2.38}$$

The control to output and line to output transfer functions may be defined as:

$$G_d(s) = \left.\frac{\hat{i}_o}{\hat{d}(s)}\right|_{\hat{i}_{dc}(s)=0} \tag{2.39}$$

$$G_{i_{dc}}(s) = \left.\frac{\hat{i}_o}{\hat{i}_{dc}(s)}\right|_{\hat{d}(s)=0} \tag{2.40}$$

The continues current mode transfer functions are derived by applied the Laplace transform at the converter equations, letting initial conditions be zero:

$$\begin{cases} sC_{DC}\hat{v}_{DC} = \hat{i}_{DC}(s) + I_{L4}\cdot\hat{d}(s) + \hat{i}_{L4}(s)\cdot D \\ sL_4\hat{i}_{L4}(s) = (V_{DC}+V_{C0})\hat{d}(s) + D\cdot\hat{v}_{DC}(s) - (1-D)\hat{v}_{C0}(s) \\ sL_0\hat{i}_{L0}(s) = \hat{v}_{C0}(s) - R_b\hat{i}_{L0}(s) \\ sC_0\hat{v}_{C0}(s) = -\hat{i}_{L0}(s) + (1+D)\hat{i}_{L4}(s) - I_{L4}\cdot\hat{d}(s) \end{cases} \tag{2.41}$$

The system equations, may be written in the matrix form:

$$\begin{cases} s\hat{x} = A\cdot\hat{x} + B\cdot\hat{u} \\ \hat{y} = C\hat{x} \end{cases} \tag{2.42}$$

where:

$$\hat{x}=\begin{bmatrix}\hat{v}_{dc}\\ \hat{v}_{co}\\ \hat{i}_{L4}\\ \hat{i}_{Lo}\end{bmatrix} \tag{2.43}$$

$$A=\begin{bmatrix}0 & 0 & D & 0\\ D & -(1-D) & 0 & 0\\ 0 & 1 & 0 & -R_b\\ 0 & 0 & (1+D) & -1\end{bmatrix} \tag{2.44}$$

$$B=\begin{bmatrix}1 & I_{L4}\\ 0 & V_{DC}+V_{CO}\\ 0 & 0\\ 0 & -I_{L4}\end{bmatrix} \tag{2.45}$$

$$\hat{u}=\begin{bmatrix}\hat{i}_{dc}\\ \hat{d}\end{bmatrix} \tag{2.46}$$

$$C=\begin{bmatrix}0 & 0 & 0 & 1\end{bmatrix} \tag{2.47}$$

$$W(s)=C\left(sI-A\right)^{-1}B \tag{2.48}$$

Solving the system by means of symbolic function in MATLAB environment may be written:

$$G_d\left(s\right)=\frac{2D^2I_{L4}-s^3I_{L4}-s^2\left(I_{L4}-DI_{L4}\right)+s\left(V_{co}+V_{dc}+DV_{dc}+DV_{co}\right)+DI_{L4}}{R_b\left(s^2D-sD^2+s^2+s\right)-s^2D-sD^2-s^3D-D^2+s^2+2s^3+s^4} \tag{2.49}$$

$$G_{i_{dc}}\left(s\right)=\frac{D\left(D+1\right)}{D^2-s^2\left(R_b-D+DR_b+1\right)-s^4+s^3\left(D-2\right)+s\left(D^2R_b-R_b+D^2\right)} \tag{2.50}$$

2.4 References

[1] L.Ferraro, D. Iannuzzi, P. Maussion, S. Caux, “Magnetic Design of Inductive Polarized Couplers for IPT EV Charging System”.

[2] M. Borage, S. Tiwari and S. Kotaiah, "Analysis and design of an LCL-T resonant converter as a constant-current power supply," Industrial Electronics, IEEE Transactions on, vol. 52, no. 6, pp. 1547-1554, 2005.

[3] H. Pollock, “Simple constant frequency constant current load-resonant power supply under variable load conditions,” EE Electron. Lett., vol. 33, no. 18, pp. 1505–1506, Aug. 1997.

[4] M. Budhia, G. Covic, and J. Boys, “A new IPT magnetic coupler for electric vehicle charging systems,” in Proc. Annu. conf. IEEE Ind. Electron. Soc., Phoenix, AZ, 2010, pp. 2487–2492.

[5] B. Peschiera and S. S. Williamson, "Review and comparison of inductive charging power electronic converter topologies for electric and plug-in hybrid electric vehicles," Transportation Electrification Conference and Expo (ITEC), 2013 IEEE, Detroit, MI, 2013, pp. 1-6. doi: 10.1109/ITEC.2013.6573474.

[6] G. R. Nagendra, G. A. Covic and J. T. Boys, "Determining the Physical Size of Inductive Couplers for IPT EV Systems," in IEEE Journal of Emerging and Selected Topics in Power Electronics, vol. 2, no. 3, pp. 571-583, Sept. 2014.

[7] J. T. Boys, G. A. Covic and Yongxiang Xu, "DC analysis technique for inductive power transfer pick-ups," in IEEE Power Electronics Letters, vol. 1, no. 2, pp. 51-53, June 2003. doi: 10.1109/LPEL.2003.819909

[8] The power electronics handbook – Chapter 2: DC-DC converters

Chapter 3

Validation of Mathematical Model

3.1 Introduction

In this previous chapter, the mathematical model of the proposed IPT system has been developed, splitting the system into two parts: ac and dc side. The equations have been compute in MATLAB environment, and in order to validate the results of the two ac and dc models, the same systems have been developed in PSIM environment. The comparisons, between the analytical model and circuital model, have been done simulating the system in the same operative conditions.

3.2 Matlab Code

3.2.1 AC side matlab code

The AC mathematical model obtained in the previous chapter, has been implemented in MATLAB environment by means of the code (6.1.1).

In the following Fig. 3-1 to Fig. 3-3, has been shown the behavior of the transfer functions I_{L1}/I_1, I_{L2}/I_1 and I_{L3}/I_1 computed by means of the previous code matlab:

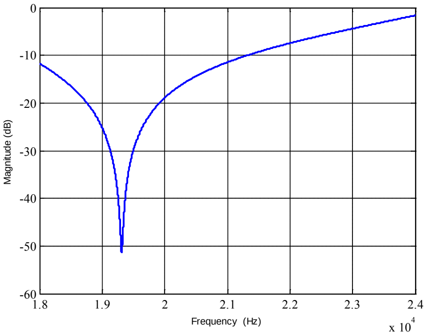

Fig. 3-1:Transfer function I_{L1}/I_1

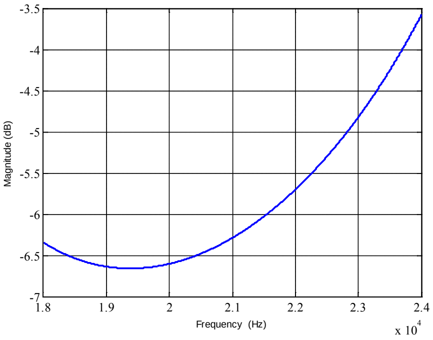

Fig. 3-2: Transfer function I_{L2}/I_1

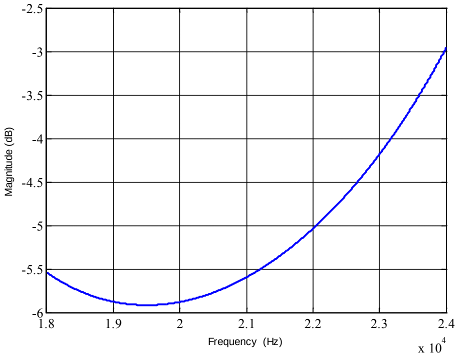

Fig. 3-3: Transfer function I_{L3}/I_1

3.2.2 DC side matlab code

The DC mathematical model obtained in the previous chapter, has been implemented in MATLAB environment by means of the code (6.1.2).

In the following Fig. 3-4, has been shown the behavior of the transfer function V_{dc}/I_{dc} computed by means of the previous code:

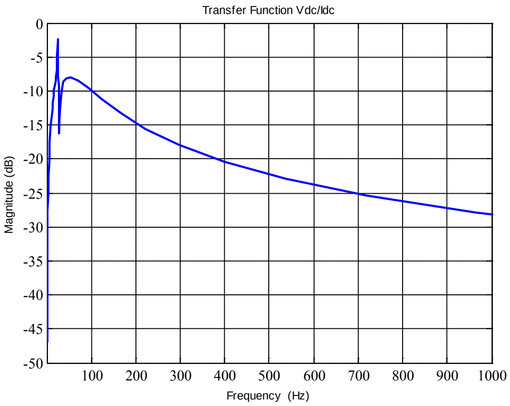

Fig. 3-4: Transfer function V_{dc}/I_{dc}

3.3 Simulated Performance

3.3.1 Overall PSIM circuit

In order to validate the mathematical model, the proposed IPT system has been built in PSIM environment that is a circuit oriented simulator model. In Fig. 3-5, is shown the PSIM circuit of the whole IPT system with a closed loop control of the charge battery current. The circuits of the components showed in Fig. 3-5 are reported in (Fig. 7-3: PSIM Coupler circuit Fig. 7-6). As mentioned in previous chapter, the power supply has been modeled by a sinusoidal current generator, that supply the primary coil of the magnetic coupler.

The latter has been modeled by means of a three windings transformer, where the first winding represents the DD primary coil and the other two windings represent the two independent windings of the BP secondary coils.

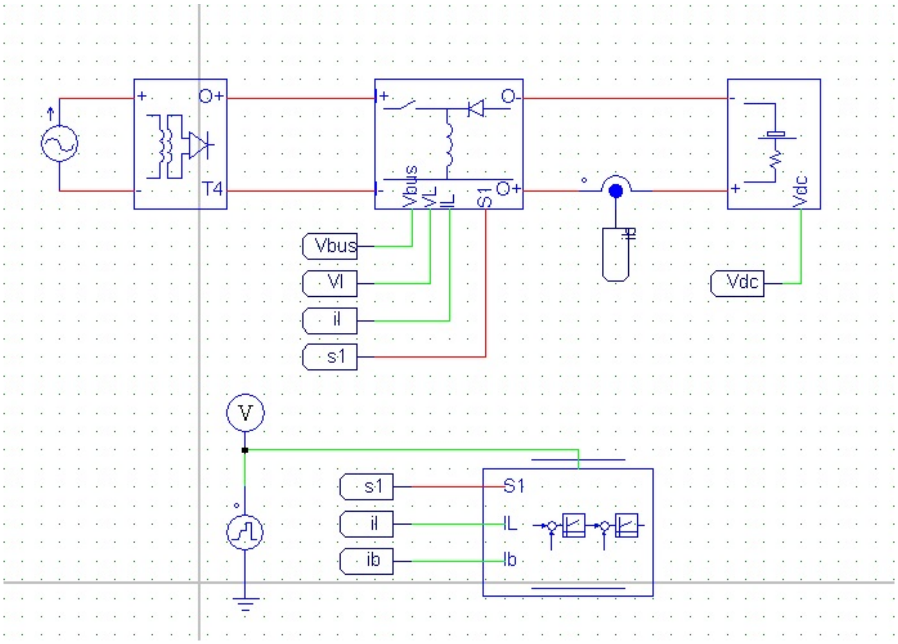

Fig. 3-5: Circuit of the whole IPT system

The outputs of the two secondary rectifiers are connected in parallel and connected at a buck boost converter, which supplies the battery. The buck boost present an output current control, better explained in the next chapter. Thus, the charge current of the battery may be controlled changing the reference value set.

Working with a fixed value of the current input, the value of the transfer power may be changed operating on the reference value of the charging current of the battery.

3.3.2 AC side PSIM circuit

In the circuit of Fig. 7-1, the AC side of the system has been represented by means of a sinusoidal current generator. The value of I'_{dc} current has been determined by means of the following relation that is true only in resonant frequency and when the dc currents are continues:

$$i_{DC} = \frac{\pi}{2\sqrt{2}} i'_{DC\_rms} = \frac{\pi}{2\sqrt{2}} \frac{i'_{DC\_\max}}{\sqrt{2}} = \frac{\pi}{4} i'_{DC\_\max} = f_{RI} i'_{DC\_\max} \qquad (3.1)$$

3.3.3 DC side PSIM circuit

In the circuit of Fig. 7-1, the DC side of the system has been represented by means of a direct current generator. The system operates with an open loop control that has a fixed value of duty cycle.

3.4 Comparison

The comparison between the MATLAB and PSIM model have been done in the same operative conditions. In particular, has been considered an airgap value of 200 mm with a perfect alignment between the transmitter and receiver pad.

3.4.1 AC comparison

In order to compare the PSIM and MATLAB models, some simulation of the AC PSIM circuit at different value of frequency have been done. The trends, at steady state of the voltages, currents and power of the system have been computed for different values of the input frequency at I_{1max}=28.28 A and I'_{dc}=19.43 A. The parameters of the equivalent circuit are reported in the Tab. 9.

Tab. 9: AC equivalent circuit parameters for an airgap of 200 mm and null misalignment

L_1 [μH]	L2 [μH]	L_3 [μH]	K_2	K_3	M_2 [μH]	M_3 [μH]	$M_{23=32}$ [μH]	C_1 [μF]	C_2 [μF]	C_3 [μF]
168.47	365.35	337.81	0.450	0.453	111.76	108.18	25.47	0.636	0.173	0.187

In the following Fig. 3-6 to Fig. 3-12, are shown the results of the AC mathematical model and the AC PSIM simulations.

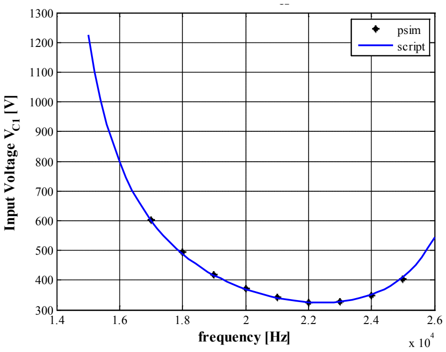

Fig. 3-6: Input voltage V_{C1}

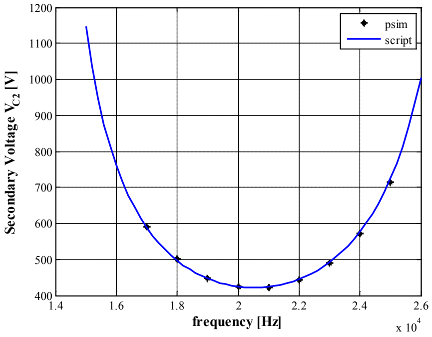

Fig. 3-7: Secondary voltage V_{C2}

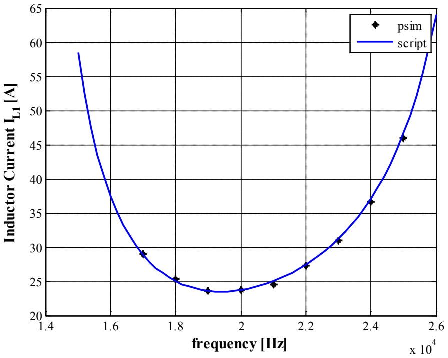

Fig. 3-8: Inductor current I_{L1}

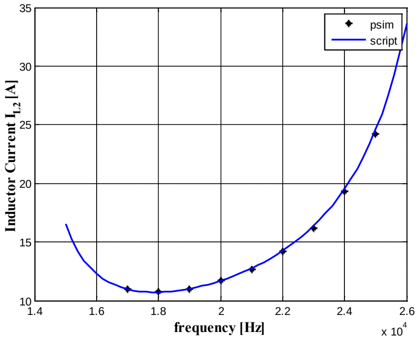

Fig. 3-9: Inductor current I_{L2}

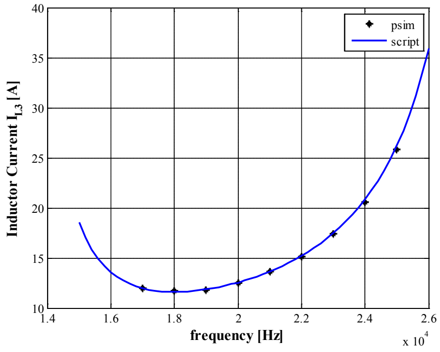

Fig. 3-10: Inductor current I_{L3}

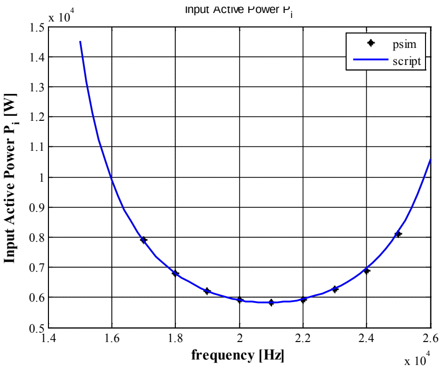

Fig. 3-11: Input active power P_i

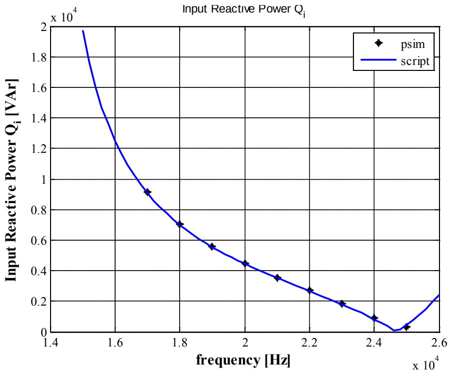

Fig. 3-12: Input reactive power Q_i

3.4.2 DC comparison

In order to compare the PSIM and MATLAB models, some simulation of the DC PSIM circuit at different value of input current have been done. The trends, at steady state of the voltages and currents have been computed for different values of input current I_{dc} ([5,30] A) with a fixed duty cycle (0,6). The parameters of the equivalent circuit are reported in the Tab. 10.

Tab. 10: DC equivalent circuit parameters ***(explained in chapter 4)**

C_{DC} [mF]	L_4 [mH]	C_o [mF]	L_o [mH]	R_b [Ω]	E_b [V]	f_c [kHz]
4.1	1	2.5	0.05	0.01	360	1

In the following Fig. 3-13 to Fig. 3-17, are shown the results of the DC mathematical and the DC PSIM simulations.

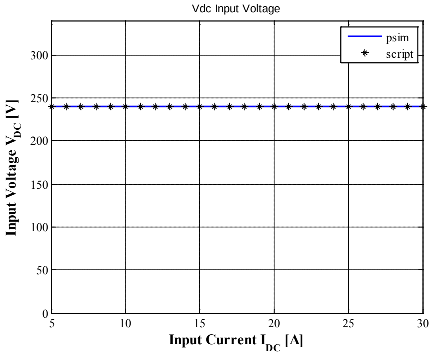

Fig. 3-13: Input Voltage

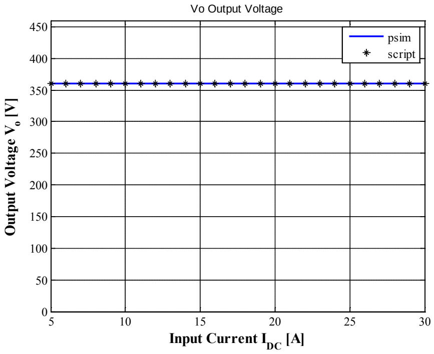

Fig. 3-14: Output Voltage

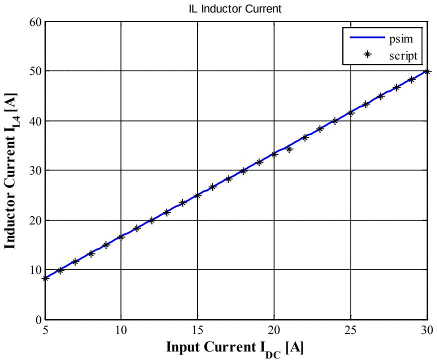

Fig. 3-15: Inductor Current

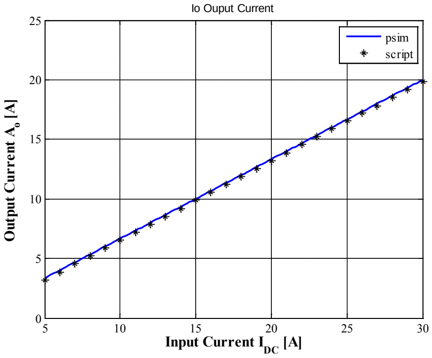

Fig. 3-16: Output Current

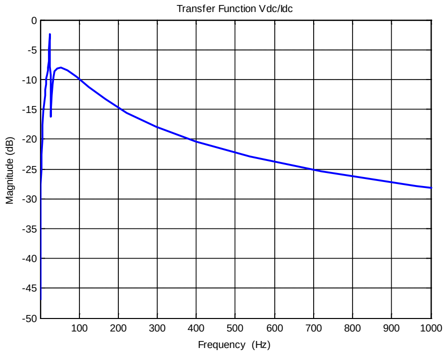

Fig. 3-17: Transfer Function V_{dc}/I_{dc}

3.5 Misalignment Analysis

To analyze the behavior of the system with misalignment, it has been taking into account the system for different values of misalignments along the x axis. For each misalignment, the trends, at steady state of the voltages, currents and power of the system have been computed for different values of the input frequency at I_{1max}=28.28 A and I'_{dc}=19.43 A. The values of the electric circuit parameters and the respective percental variations compared to the values at null misalignment are reported in Tab. 11.

Tab. 11: Electric circuit parameters

x [mm]	L_1 [mH]	L_2 [mH]	L_3 [mH]	M_{12} [mH]	M_{13} [mH]	M_{23} [mH]	K_2	K_3
0	0,168	0,365	0,338	0,112	0,108	0,025	0,450	0,453
46,5	0,178 [+5%]	0,350 [-4%]	0,338 [0%]	0,083 [-26%]	0,125 [+16%]	0,019 [-24%]	0,330 [-27%]	0,510 [+13%]
93	0,175 [+4%]	0,355 [-3%]	0,346 [+2%]	0,045 [-60%]	0,132 [+22%]	0,015 [-40%]	0,182 [-60%]	0,535 [+18%]
186	0,188 [+12%]	0,349 [-4%]	0,333 [-1%]	0,040 [-65%]	0,103 [-5%]	0,030 [+20%]	0,156 [-65%]	0,411 [-9%]

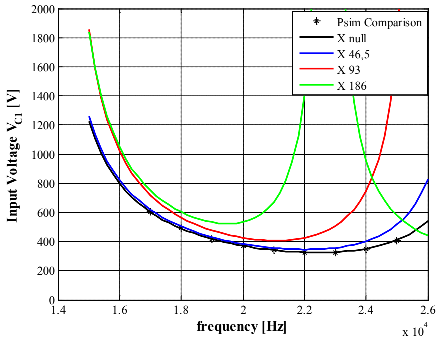

Fig. 3-18: Input Voltage V_{C1}

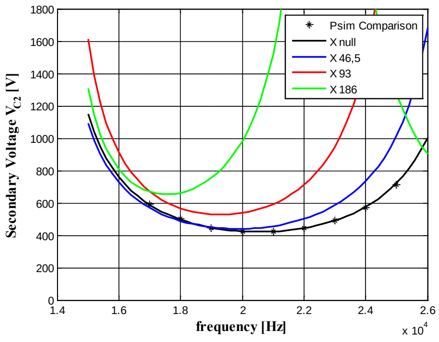

Fig. 3-19: Secondary Voltage V_{C2}

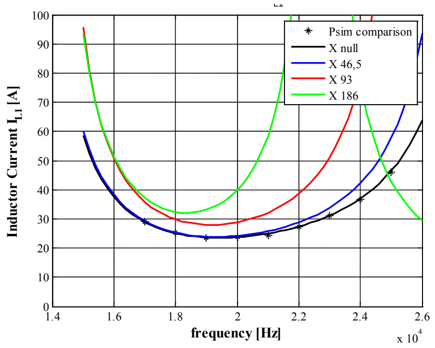

Fig. 3-20: Inductor Current I_{L1}

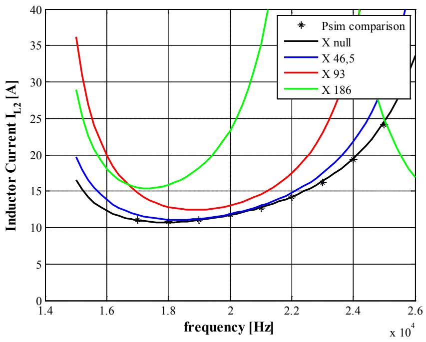

Fig. 3-21: Inductor Current I_{L2}

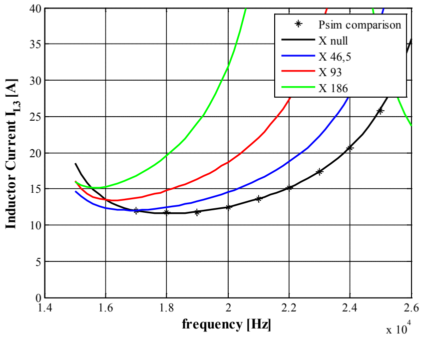

Fig. 3-22: Inductor Current I_{L3}

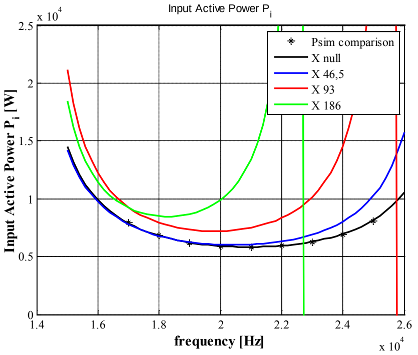

Fig. 3-23: Input Active Power P_i

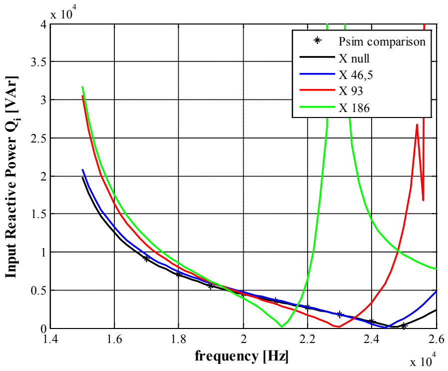

Fig. 3-24: Input Reactive Power Q_i

3.6 Conclusions

From the Fig. 3-6 to Fig. 3-12 for the AC model and from the Fig. 3-13 to Fig. 3-17 for the DC model, may be noted that the results of the mathematical model obtained and of the circuital model are matching.

In the case of different misalignment, only the AC model is affected of the parameters variations and from the result showed in Fig. 3-18 to Fig. 3-24, may be noted that the behavior of the system is closer to the results of perfect alignment only if the value of misalignment is not high and the value of frequency is lower of resonant frequency design.

The aim of this comparison has not been only to be sure that the mathematical models correspond to the circuits, but also allow the transfer functions extraction, necessary for the control analysis of the system explained in the next chapter.

Chapter 4

Control System Design

4.1 Controller Design

In order to have a wide diffusion on the market of no polluting vehicles, they have to present the characteristics of travel ranges and recharging times comparable to the traditional oil based fuel vehicles. For these reasons EVs require battery packs characterized by high values of both energy storage capacity and charging rates. From this point of view lithium based batteries 0 represent a very interesting solution, as they are showing a great potential, in recent years, to supply electric vehicles having good performance in terms of acceleration and driving range. As reported in [2], [3], there are different charging device, modes, architecture and control strategies to refill an EV battery. The lithium batteries, unlike capacitors or other kinds of batteries, cannot be charged by a regular supply. They need to be charged up to a specific voltage and with limited current, otherwise they can be damaged or age prematurely reducing their capacity

There are a lot of different types of lithium batteries, but they are only different in the materials used and architecture. Different types of batteries have different characters and limitations. The good thing is that most batteries are charged in the same way. A charge cycle involves two main stages: constant current or CC and voltage source or CV. During the CC stage the battery is basically connected to a current limited power supply, it lasts until the cell voltage reaches the max limit voltage. At the end of this stage, the battery charge is around 70-80 %. During the CV stage or saturation stage, when the battery reaches the max limit voltage, the charger acts as a voltage limited power supply. The battery voltage remains fixed while the charge current drops gradually. When the charge current is between 3 and 10% of the labeled capacity, the battery is considered fully charged. In Fig. 4-1, is shown a CC-CV battery charging profile.

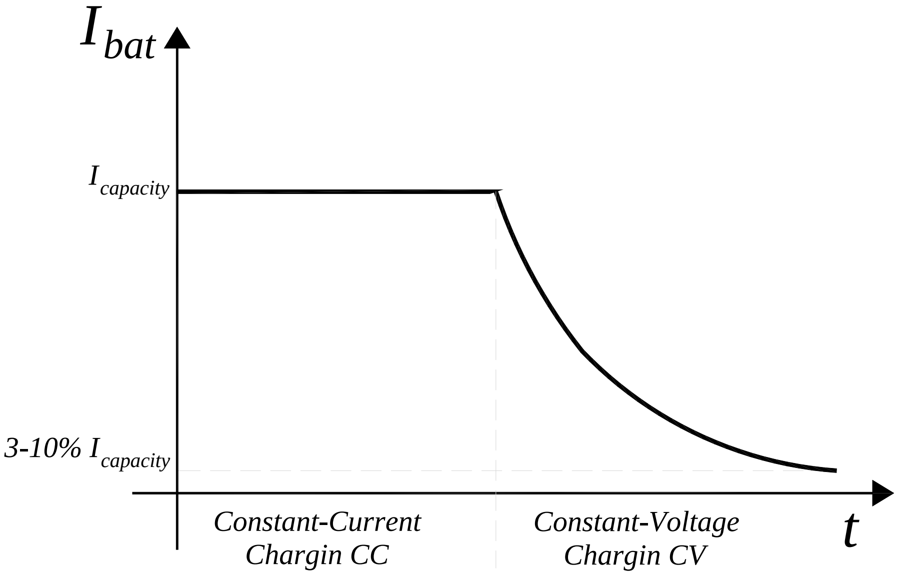

Fig. 4-1: CC-CV battery charging

The main goal is to obtain a constant value of the charge battery current Io. This current depend on duty cycle d and the input current i_{dc} of the buck boost DC/DC converter employed in the proposed IPT system Fig. 4-2. In order to satisfy thus, it is necessary operate on the value of duty cycle building a circuit that automatically adjust the duty cycle as necessary, to obtain the specified output current with high accuracy, regardless of disturbances or component tolerances.

4.2 Buck Boost Control

A schematic of the buck-boost converter circuit is shown in Fig. 4-2. As explain in the chapter 2, the main power switch it could be any device that could be turned on and off in a controlled fashion. This converter processes the power from a DC biased source to a DC output. The DC output voltage value can be chosen to be higher or lower than the input DC voltage. In a general sense, this circuit processes power from input to output with square wave technology, that is, the circuit produces waveforms that have sharp edges.

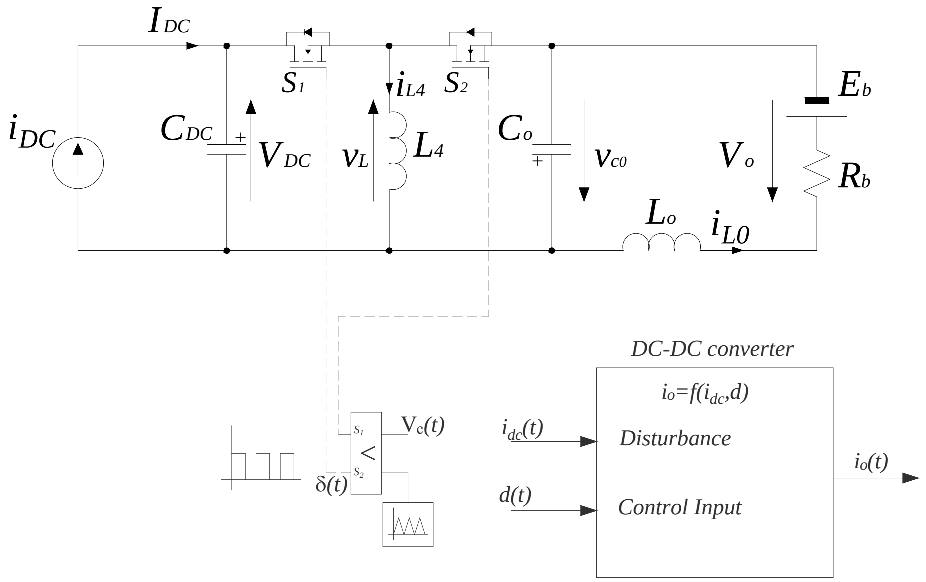

Fig. 4-2: Buck-boost circuit and control scheme

In the Fig. 4-3, is shown a negative feedback circuit of the converter. Utilizing the output transfer functions obtained in the chapter 2 for the small signal analysis, may be drawn the block diagram shown in Fig. 4-4.

A control scheme that is widely used for dc-dc converters is current mode control [4]. Current mode controlled dc-dc converters have two feedback loop:

- a current I_{L4} feedback loop;
- a current I_{LO} feedback loop.

A current mode controlled dc-dc buck boost converter circuit is shown in Fig. 4-3. An error signal is produced after comparing the output current i_{LO} with fixed reference i^*_{LO} and this error signal is used to generate control signal i^*_{L4}. The inductor current i_{L4} is compared with the control signal i^*_{L4} from the controller to generate the duty cycle of particular frequency and drive the switch of the converter.

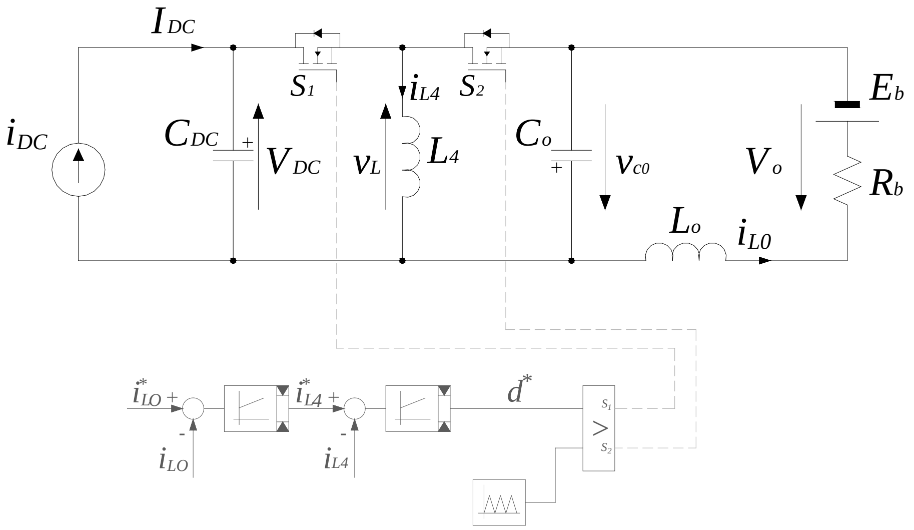

Fig. 4-3: Buck-boost circuit and cascade PI control

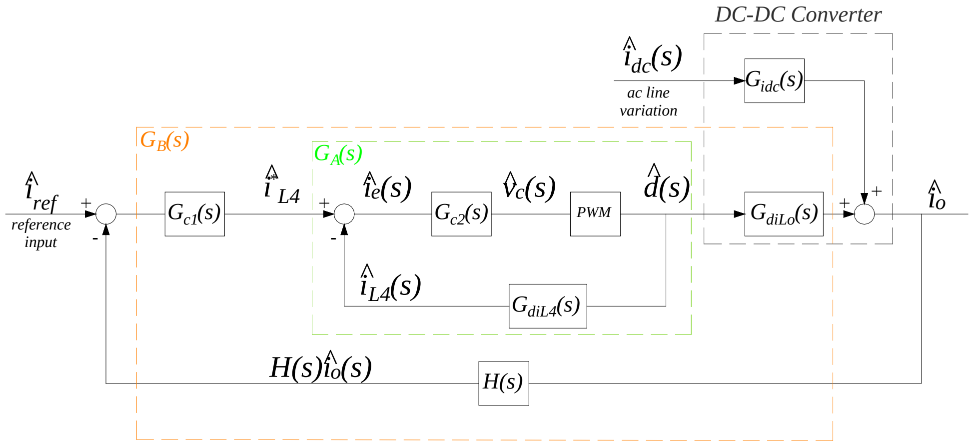

Fig. 4-4: Regulator system small signal block diagram

In the following are reported the transfer function of the block diagram Fig. 4-4:

$$G_{i_{dc}}(s) = \left.\frac{\hat{i}_o}{\hat{i}_{dc}(s)}\right|_{\hat{d}(s)=0} \tag{4.1}$$

$$G_{di_{Lo}}(s) = \left.\frac{\hat{i}_o}{\hat{i}_{Lo}(s)}\right|_{\hat{i}_{dc}(s)=0} \tag{4.2}$$

$$G_{di_{L4}}(s) = \frac{\hat{i}_{L4}}{\hat{d}(s)} \tag{4.3}$$

$$G_{C1}(s) = \frac{K_1}{1+sT_1} \tag{4.4}$$

$$G_{C2}(s) = \frac{K_2}{1+sT_2} \tag{4.5}$$

$$G_A(s) = \frac{G_{C2}}{1+G_{C2}G_{di_{L4}}} \tag{4.6}$$

$$G_B(s) = \frac{G_{C1}G_AG_{di_{Lo}}}{1+G_{C1}G_AG_{di_{Lo}}} \tag{4.7}$$

$$T(s) = G_{C1}G_AG_{di_{Lo}} \tag{4.8}$$

$$G_C(s) = \frac{G_{i_{dc}}}{1+T} \tag{4.9}$$

Manipulate block diagram to solve for i_o, result is:

$$\hat{i}_o = \hat{i}_{ref}\frac{T}{1+T} + \hat{i}_{dc}\frac{G_{i_{dc}}}{1+T} \tag{4.10}$$

The input duty cycle to output current transfer function:

$$G_{di_{Lo}}(s) = \left.\frac{\hat{i}_o}{\hat{i}_{Lo}(s)}\right|_{\hat{i}_{dc}(s)=0} \tag{4.11}$$

is shown in the following figure:

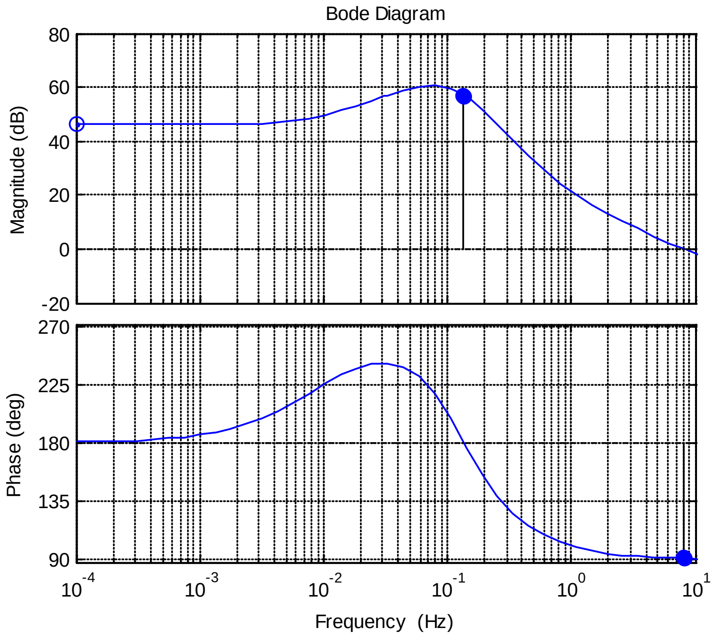

Fig. 4-5:Bode diagram of the transfer function G_{dilo}

The original open loop line to output transfer function

$$G_{i_{dc}}(s)=\left.\frac{\hat{i}_o}{\hat{i}_{dc}(s)}\right|_{\hat{d}(s)=0} \tag{4.12}$$

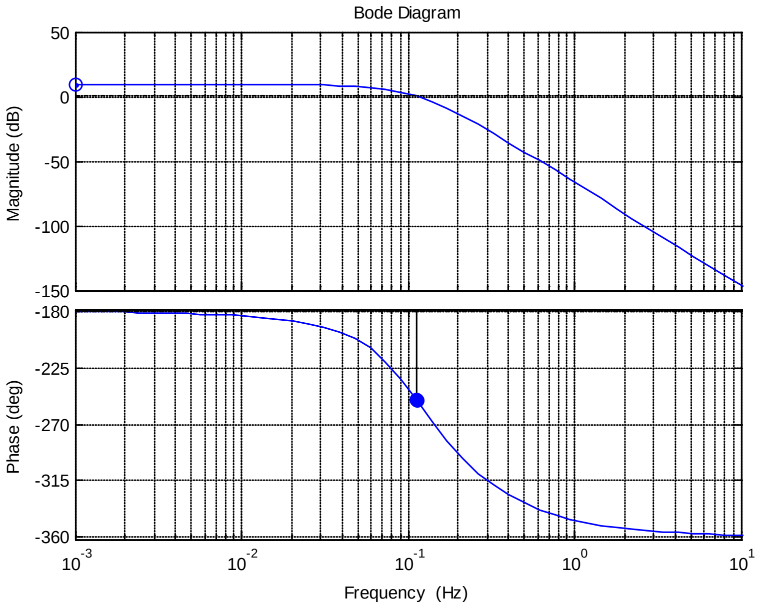

Fig. 4-6: Bode diagram of the transfer function Gi_{dc}

with addition of negative feedback, the line to output transfer function becomes:

$$\left.\frac{\hat{i}_o}{\hat{i}_{dc}}\right|_{\hat{d}(s)=0} = \frac{G_{i_{dc}}(s)}{1+T(s)} \tag{4.13}$$

The feedback reduces the line to output transfer function by a factor of:

$$\frac{1}{1+T(s)} \tag{4.14}$$

If T(s) is large in magnitude, then the line to output transfer function becomes small.

Closed loop transfer function is

$$\left.\frac{\hat{i}_o}{\hat{i}_{ref}}\right|_{\hat{i}_{dc}=0} = \frac{T(s)}{1+T(s)} \tag{4.15}$$

If the loop gain is large in magnitude, ||T||>>1, then (1+T)~T and the transfer function then becomes

$$\left.\frac{\hat{i}_o}{\hat{i}_{ref}}\right|_{\hat{i}_{dc}=0} \approx 1 \tag{4.16}$$

which is independent of the gains in the forward path of the loop

4.3 Stability

It is well known that adding a feedback loop can cause an otherwise stable system to become unstable. Even though the transfer functions of the original converter, as well as of the loop gain T(s), contain no right half plane poles, it is possible for the closed loop transfer functions to contain right half plane poles. The feedback loop then fails to regulate the system at the desired quiescent operating point, and oscillation are usually observed. It is important to avoid this situation. And even when the feedback system is stable, it is possible for the transient response to exhibit undesirable ringing and overshoot. When the feedback destabilizes the system, the denominator (1+T(s)) contain roots in the right half plane. If T(s) is a rational fraction, that is, the ratio N(s)/D(s) of two polynomial functions N(s) and D(s), then we can write

$$\frac{T(s)}{1+T(s)} = \frac{\frac{N(s)}{D(s)}}{1+\frac{N(s)}{D(s)}} = \frac{D(s)}{N(s)+D(s)} \tag{4.17}$$

A brute force test for stability is to evaluate N(s)+D(s), and factor the result to see whether any of the roots have positive real parts. However, for all but very simple loop gains, this involves a great deal of work. A simpler method is given by the Nyquist stability theorem, in which the number of right half plane roots of N(s)+D(s), can be determined by testing T(s).

4.4 Regulator Design

The design of the control system involves modifying the loop gain. As illustrated in Fig. 4-4, a compensator network is added for this purpose. The lag PI compensator is used to increase the low frequency loop gain, such that the output is better regulated at dc and at frequencies well below the loop crossover frequency. An inverted zero is added to the loop gain at frequency f_L.

$$G_c(s) = G_{c\infty}\left(1 + \frac{\omega_L}{s}\right) \tag{4.18}$$

This type of compensator is also called a proportional plus integral or PI controller at low frequencies, the inverted zero causes the compensator to integrate the error signal.

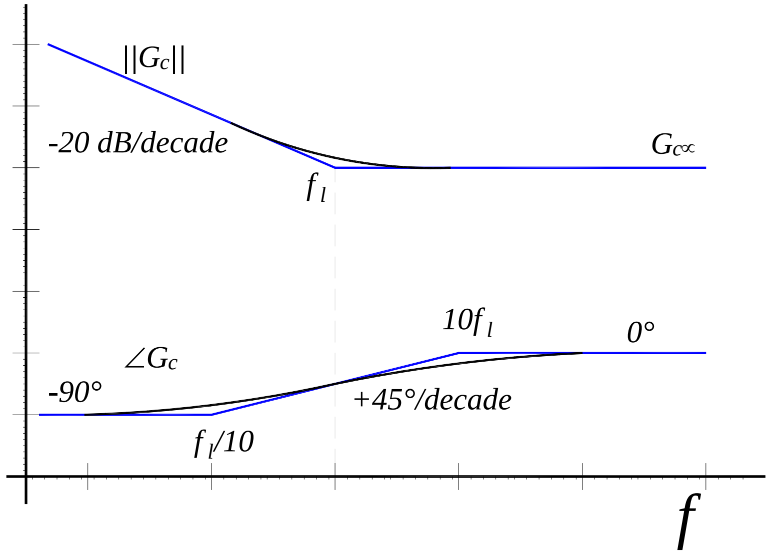

Fig. 4-7: Magnitude and phase asymptotes of the PI compensator transfer function Gc

4.5 PID Controller

A PID controller is feedback loop controlling mechanism. It corrects the error between a measured process value and a desired set point by calculating and then a corrective action adjusts the process as per the requirement. The PID controller calculation involves three separate parameters: the proportional value P determines the reaction to the current error; the integral value I determines the reaction based on the sum of recent errors; the derivative value D determines the reaction to the rate at which the error has been changing. The weighted sum of these actions is used to adjust the process via a control element. By tuning the three constants, the PID controller can provide control action designed for specific requirements.

4.5.1 Ziegler Nichols Method

The block diagram shown in Fig. 4-8, illustrates a closed loop system with a PID controller in the direct path, which is the usual connection [5]. The system's output should follow as closely as possible the reference signal:

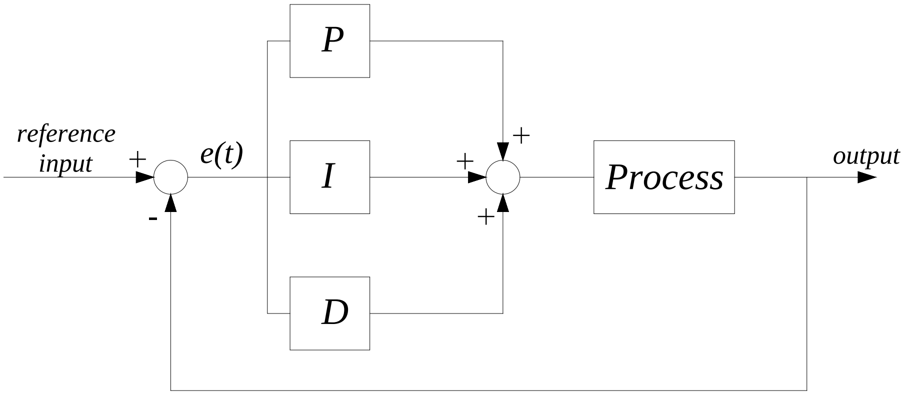

Fig. 4-8: Block diagram of PID controller

The control output is obtained as follows:

$$U(t) = K_p e(t) + K_i \int_0^t e(\tau) d\tau + k_d \frac{de(t)}{dt} \tag{4.19}$$

whereas the transfer function is given as

$$w(s) = K_p + \frac{K_i}{S} + K_d S \tag{4.20}$$

There are several methods for tuning a PID loop. The most effective methods usually involve the development of some form of process model, then choosing P, I, and D based on dynamic model parameters. Manual tuning methods can be relatively insufficient, particularly if the loops have response times on the order of minutes or longer.

The best tuning method for the PID controller was given by Ziegler and Nichols, which was now accepted as standard technique in control systems practice. Both techniques make prior assumptions on the system model, but do not require that these models are specifically known. Ziegler-Nichols formulae for specifying the controllers are based on plant step responses.

The method targets plants that can be rendered unstable under the proportional control. The technique is designed to result in a closed loop with 25% peak overshoot. This is rarely achieved as Ziegler and Nichols determined the adjustments based on a specific plant model. The steps for tuning a PID controller are as follows:

Using only proportional feedback control:

1. Reduce the integrator and derivative gains to 0;
2. Increase K_p from 0 to some critical value $K_p=K_{cr}$ at which oscillations occur. If it does not occur, then other method has to be applied;
3. Note the value K_{cr} and the corresponding period of sustained oscillation, T_{cr}.

The controller gain is specified as follows:

Tab. 12: PID parameters

PID TYPE	K_P	$T_I= K_P/ K_I$	$T_D= K_D/ K_I$
P	0.5Kcr	∞	0
PI	0.45Kcr	Tcr/1.2	0
PID	0.6Kcr	Tcr/2	Tcr/2

4.5.2 Design of Buck Boost

Designing of buck boost converter is always a challenging task with respect to proper design of electronic components: capacitors and inductor and obtaining the prescribed values of ripple factor of output voltage and current. Software packages, as PSIM environment, are always useful simulation tools which allow prediction of circuit behavior and its components. The buck boost circuit analyzed is shown in Fig. 4-3.

Input and output voltages are related to each other with relationship:

$$d = \frac{V_o}{V_o + V_{DC}} \tag{4.21}$$

where *d* is the duty cycle.

In order to choose the value of the inductor and capacitance may be followed the procedure shown in [6]. First step in building of buck boost converter is the proper problem definition. Input voltage of the buck boost is a function of the alignment, airgap, the rate of power transfer, whereas the output value is closer to the battery voltage value. May be considered an input voltage V_{dc} in the range [250-400] V and an output voltage V_o of 360 V. The switching frequency of main switch S_1 and S_2 is f_c 1 kHz, the desiderated output current I_{LO} is 25 A.

Minimal duty cycle is calculated from:

$$d_{\min} = \frac{V_{o\min}}{V_{o\min} + V_{DC\min}} = \frac{250}{250+360} = 0.41 \tag{4.22}$$

while maximum duty cycle is calculated from:

$$d_{\max} = \frac{V_{o\max}}{V_{o\max} + V_{DC\max}} = \frac{400}{400+360} = 0.53 \tag{4.23}$$

The inductor value has to be large enough to handle the output power, according to the energy transfer equation shown below [7]:

$$\frac{1}{2} L i_{peak}^2 = P T_p \tag{4.24}$$

where i_{peak} is the maximum value of the inductor current, P is the output power, and T_p is the time period of the switching cycle. If the desire for the current is to be continuous, then the inequality shown below must be satisfied:

$$\frac{2L}{R_L} > \frac{T_p}{\left(\frac{V}{V_s} + 1\right)^2} \tag{4.25}$$

Satisfying the above two constraints, should provide an inductor that is minimal, but probably not optimal.

$$L_{\min} > \frac{T_p}{\left(\frac{V_O}{V_{dc\max}} + 1\right)^2} R_L = \frac{1 \cdot e^{-3}}{\left(\frac{360}{400} + 1\right)^2} \frac{360}{25} \approx 0.004 \quad [H] \tag{4.26}$$

The capacitor value is chosen based on the specified ripple voltage, V_{PP}, the switching frequency, and the allowable capacitor ripple current, $i_{allowable}$. The following inequality describes the relationship of the previously mentioned items:

$$C_o > \frac{i_{allowable}}{V_{pp}} T_{off} \qquad (4.27)$$

$$C_o > \frac{i_{allowable}}{V_{pp}} T_{off} = \frac{25}{10} 1 \cdot e^{-3} = 0.0025 \quad [F] \qquad (4.28)$$

As with the inductor value, this constraint provides a minimal capacitor value, but probably not an optimal one.

4.6 Circuit model

The proposed control IPT system has been built in PSIM environment. In Fig. 4-9, is shown the PSIM circuit of the whole system. In order to control the power flow, it has been chosen a secondary side control, in fact as shown in Fig. 7-4, the circuit of DC/DC converter consists of a controlled buck boost converter. The primary current and frequency of the system are held nominally constant and by means of a secondary side control it possible regulates the power as required by the current reference. In the Fig. 7-3 - Fig. 7-6, are shown the block subsystem used in the circuit shown in Fig. 4-9.

In order to analyze the performance of the control system respect to the possible misalignments, it has been taking into account the system for different values of misalignments along the x axis and y axis. Moreover, in order to test the performance of the PI control, it has been simulated for two different profile of the reference output current I_o as shown in Fig. 4-10, Fig. 4-18 , with a fixed input current (I_{1max}=28.28 A f=20 kHz) and voltage battery (E_b=360 V). So, there are four possible cases of study:

Case 1	one value of current reference (Fig. 4-10) with x misalignments;
Case 2	different values of current reference (Fig. 4-18) with x misalignments;
Case 3	one value of current reference with y misalignments;
Case 4	different values of current reference with y misalignments;

In each case, the profile of the output current I_o, output power P_o, inductor current I_L, bus voltage V_{bus}, input rms voltage V_1, secondary rms voltage V_2, input rms current I_1, have been reported in the Fig. 4-10-Fig. 4-49.

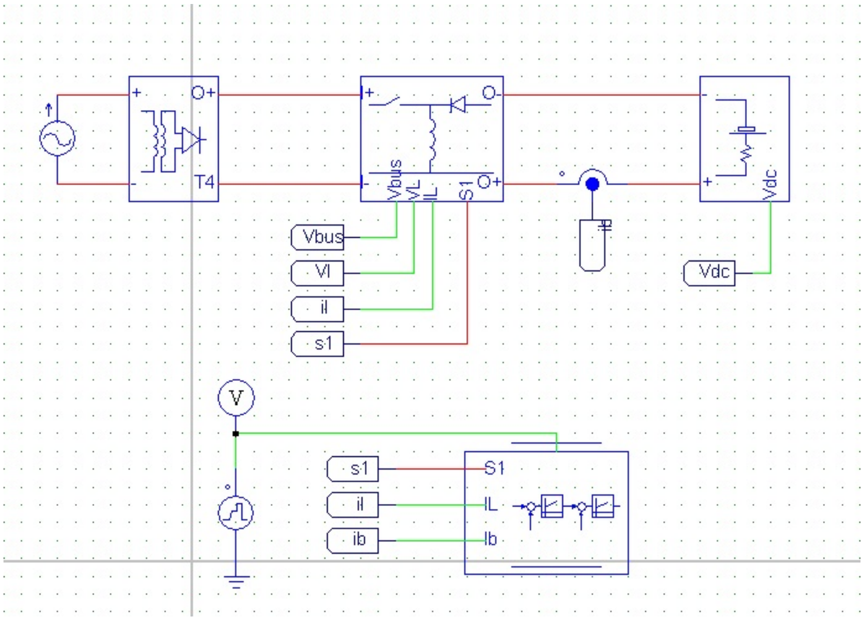

Fig. 4-9: PSIM Whole circuit

4.6.1 X axis misalignment analysis

In Tab. 11 are reported the electric circuit parameters for x axis misalignments.

Tab. 13: Electric circuit parameters for x misalignments

x [mm]	L_1 [mH]	L_2 [mH]	L_3 [mH]	M_{12} [mH]	M_{13} [mH]	M_{23} [mH]	K_2	K_3
0	0,168	0,365	0,338	0,112	0,108	0,025	0,450	0,453
46,5	0,178 [+5%]	0,350 [-4%]	0,338 [0%]	0,083 [-26%]	0,125 [+16%]	0,019 [-24%]	0,330 [-27%]	0,510 [+13%]
93	0,175 [+4%]	0,355 [-3%]	0,346 [+2%]	0,045 [-60%]	0,132 [+22%]	0,015 [-40%]	0,182 [-60%]	0,535 [+18%]
186	0,188 [+12%]	0,349 [-4%]	0,333 [-1%]	0,040 [-65%]	0,103 [-5%]	0,030 [+20%]	0,156 [-65%]	0,411 [-9%]

The system has been computed in different displacement conditions, substituting the values shown in Tab. 11, in the PSIM circuit reported in Fig. 7-3.

4.6.1.1 Results of case 1

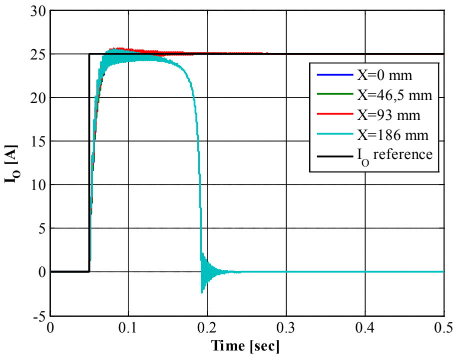

Fig. 4-10: Output current case 1

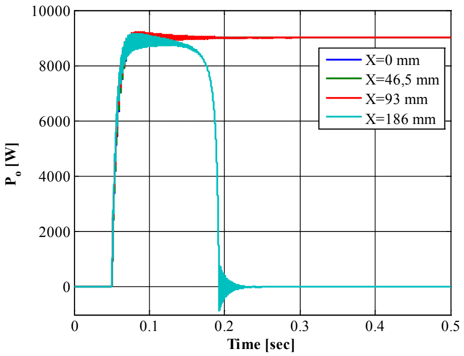

Fig. 4-11: Output power case 1

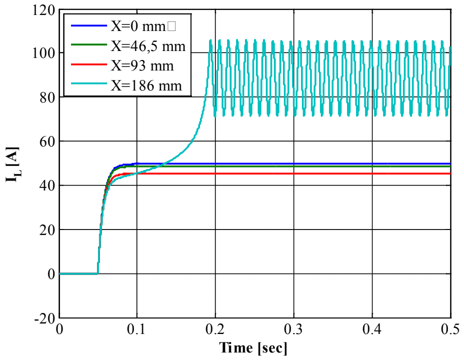

Fig. 4-12: Inductor current L4 case 1

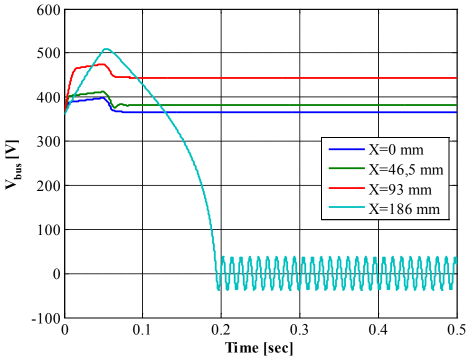

Fig. 4-13: DC Bus Voltage case 1

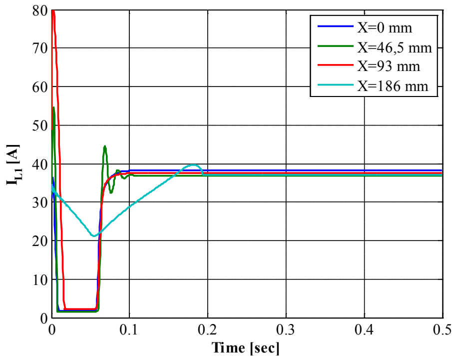

Fig. 4-14: Inductor current L1 case 1

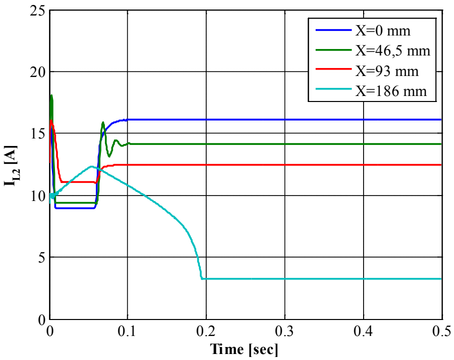

Fig. 4-15: Inductor current L2 case 1

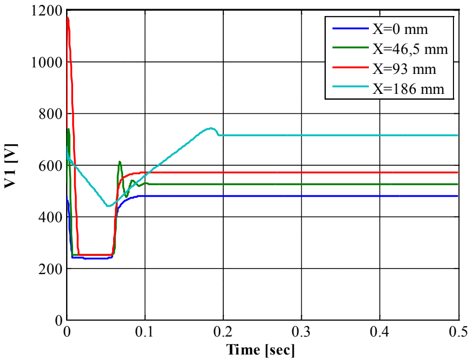

Fig. 4-16: Input voltage case 1

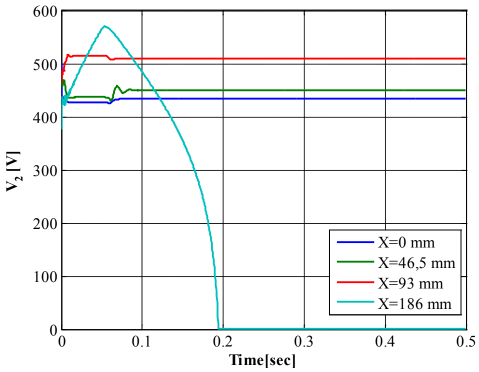

Fig. 4-17: Secondary voltage case 1

4.6.1.2 Results case 2

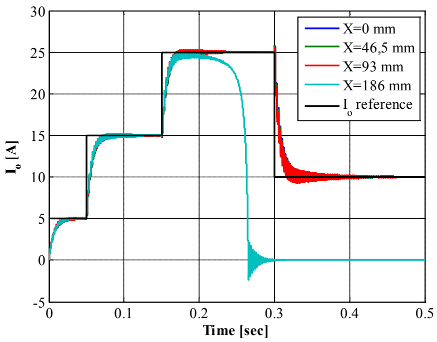

Fig. 4-18: Output current case 2

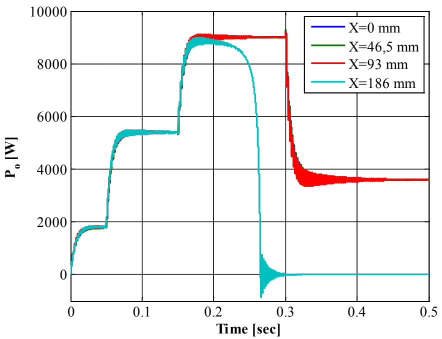

Fig. 4-19: Output power case 2

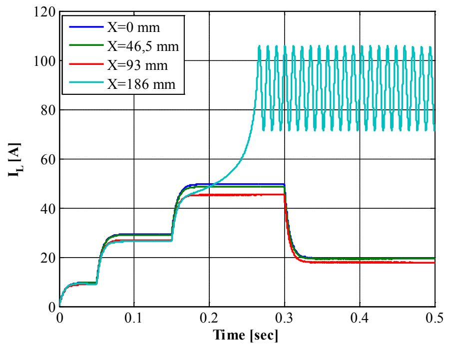

Fig. 4-20: Inductor current L4 case 2

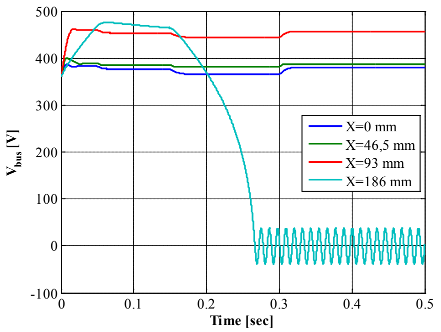

Fig. 4-21: DC Bus Voltage case 2

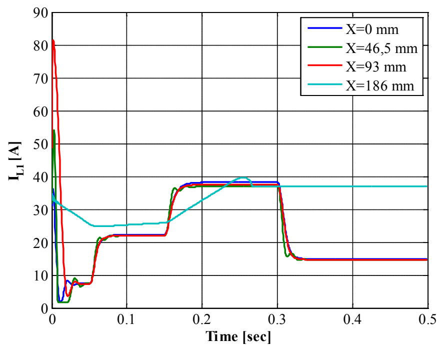

Fig. 4-22: Inductor current L1 case 2

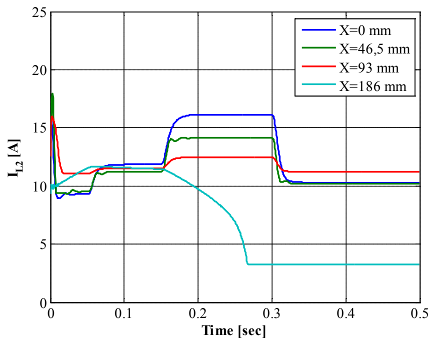

Fig. 4-23: Inductor current L2 case 2

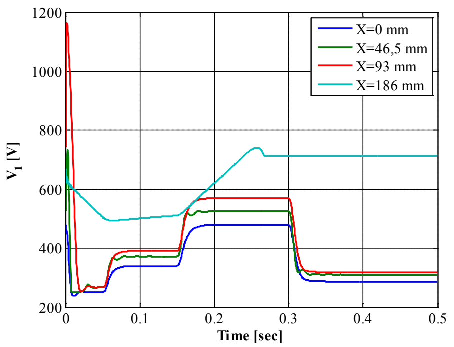

Fig. 4-24: Input voltage case 2

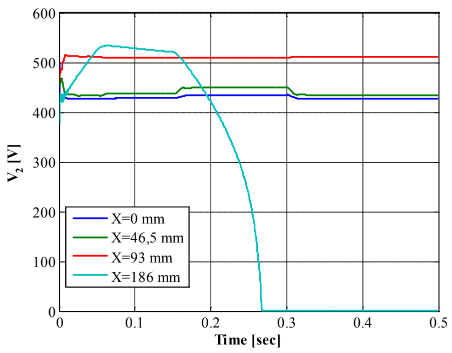

Fig. 4-25: Secondary voltage case 2

Observing the previous figures, it can be pointed out that until an x-axis misalignment of 93 mm, the control system is able to follow the reference value, allowing a transfer power of about 9 kW, whereas with an x-axis misalignment of 186 mm, the system became instable and the power transfer drops to zero.

Taking into account the Fig. 4-18 - Fig. 4-25, it may be noted that if the reference power transfer is not to high the control system is able to follow the reference also with an x-axis misalignment of 186 mm.

In order to analyze the limit of the reference power transfer, it has been done some simulation of the system with an x-axis misalignment of 186 mm, and different values of the reference output current. The results of this analysis are shown in the Fig. 4-26 - Fig. 4-33.

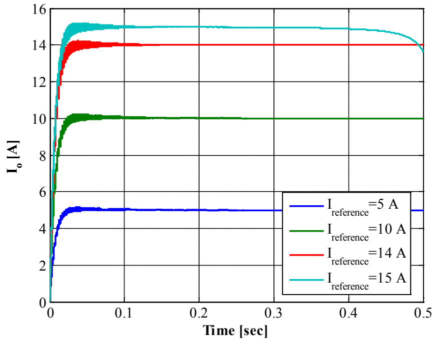

Fig. 4-26: Output current with a misalignment x=186 mm

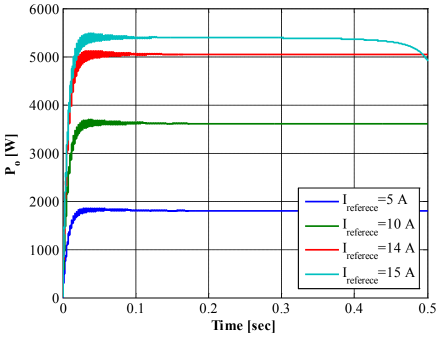

Fig. 4-27: Output power with a misalignment x=186 mm

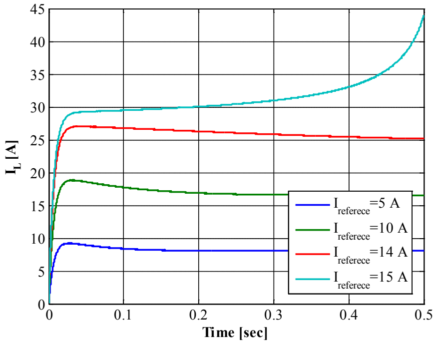

Fig. 4-28:Inductor current I_{L4} with a misalignment x=186 mm

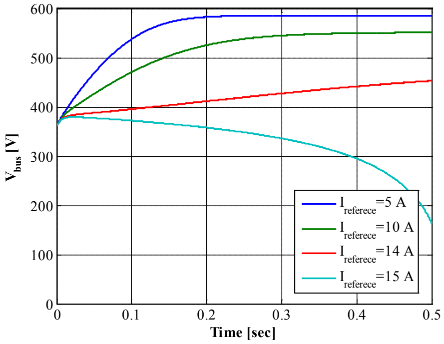

Fig. 4-29: DC Bus Voltage with a misalignment x=186 mm

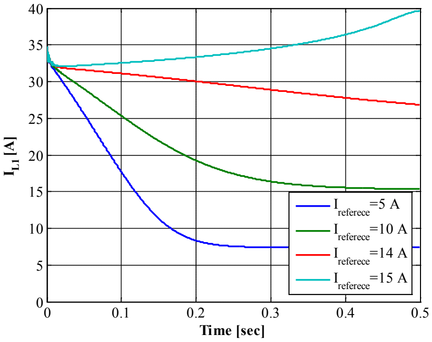

Fig. 4-30: Inductor current I_{L1} with a misalignment x=186 mm

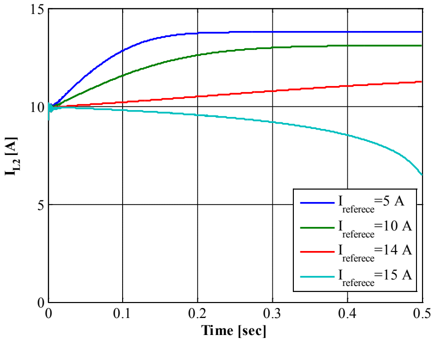

Fig. 4-31: Inductor current IL2 with a misalignment x=186 mm

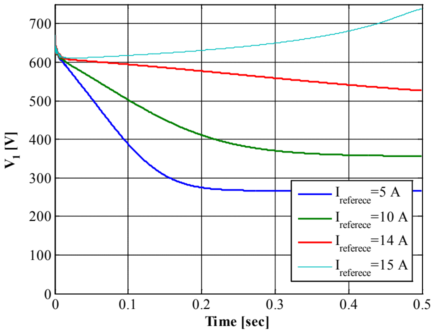

Fig. 4-32: Input voltage with a misalignment x=186 mm

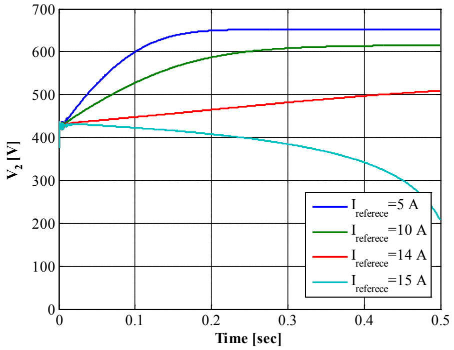

Fig. 4-33: Secondary voltage with a misalignment x=186 mm

The previous figures Fig. 4-26 - Fig. 4-33, shown that the system, in this condition, become instable when the reference current value is higher than 14 A.

Therefore, the control of the proposed IPT system allows a power transfer also in presence of the misalignment, but the value of the power transfer has to be reduced, in order to keep the stability. In our simulation conditions, the power transfer has to kept lower than 5 kW as shown in Fig. 4-27.

4.6.2 Y axis misalignment analysis

In Tab. 14 are reported the electric circuit parameters for y axis misalignments.

Tab. 14: Electric circuit parameters for y misalignments

y [mm]	L_1 [mH]	L_2 [mH]	L_3 [mH]	M_{12} [mH]	M_{13} [mH]	M_{23} [mH]	K_2	K_3
0	0,168	0,365	0,338	0,112	0,108	0,025	0,450	0,453
26,5	0,173 [+3%]	0,334 [-9%]	0,320 [-6%]	0,098 [-14%]	0,108 [0%]	0,019 [-30%]	0,407 [-10%]	0,461 [+2%]
53	0,188 [+11%]	0,339 [-8%]	0,341 [+1%]	0,104 [-8%]	0,105 [-3%]	0,015 [-60%]	0,411 [-9%]	0,413 [-9%]
106	0,176 [+4%]	0,344 [-6%]	0,330 [-2%]	0,098 [-14%]	0,099 [-9%]	0,030 [+17%]	0,400 [-13%]	0,411 [-10%]

The system has been computed in different displacement conditions, substituting the values shown in Tab. 14, in the PSIM circuit reported in Fig. 7-3.

4.6.2.1 Results of case 3

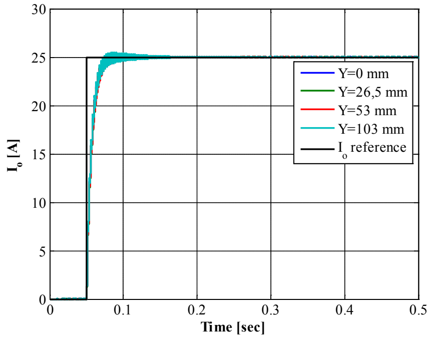

Fig. 4-34: Output current case 3

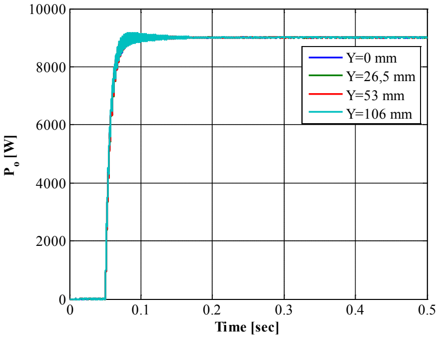

Fig. 4-35: Output power case 3

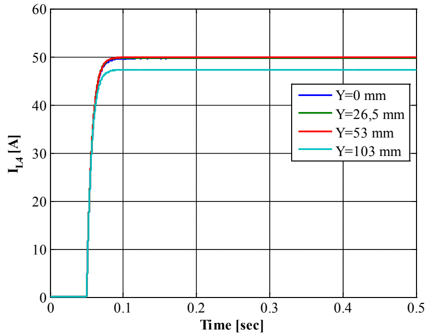

Fig. 4-36: Inductor current L4 case 3

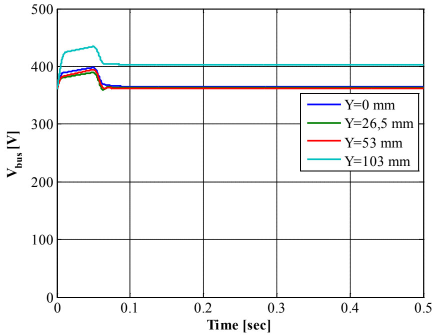

Fig. 4-37: DC Bus Voltage case 3

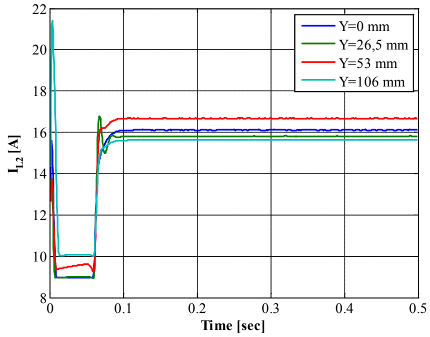

Fig. 4-38: Inductor current L1 case 3

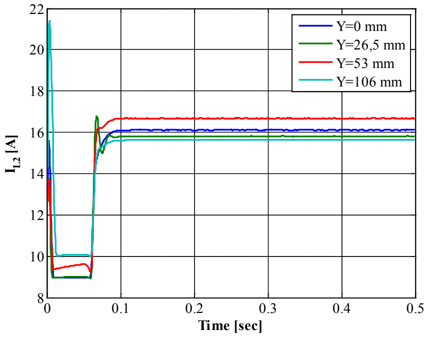

Fig. 4-39: Inductor current L2 case 3

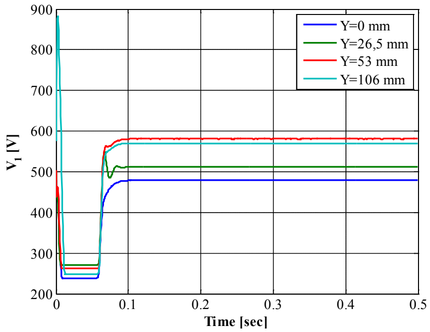

Fig. 4-40: Primary Voltage case 3

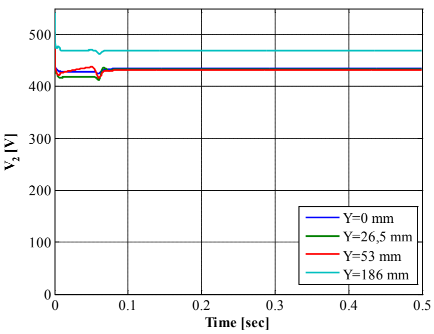

Fig. 4-41: Secondary Voltage case3

4.6.2.2 Results of case 3

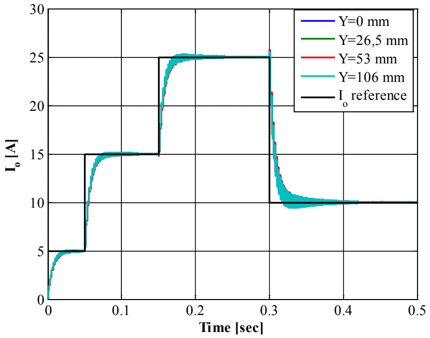

Fig. 4-42: Output current case 4

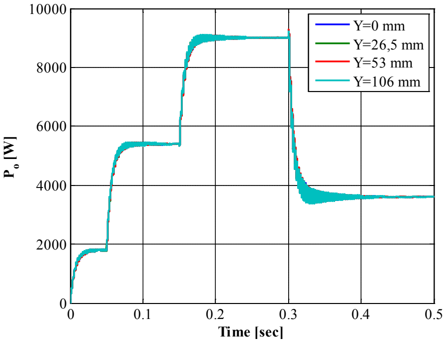

Fig. 4-43: Output power case 4

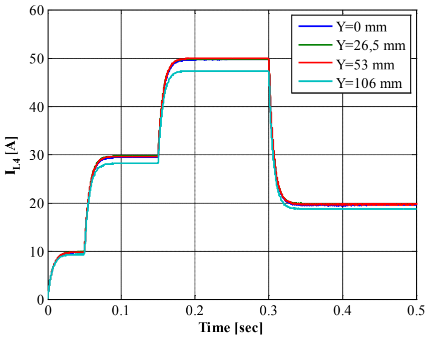

Fig. 4-44: Inductor current L4 case 4

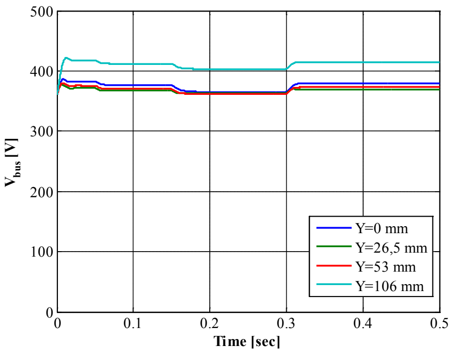

Fig. 4-45: DC Bus Voltage case 4

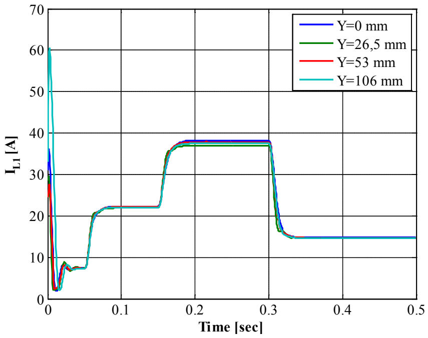

Fig. 4-46: Inductor current L1 case 4

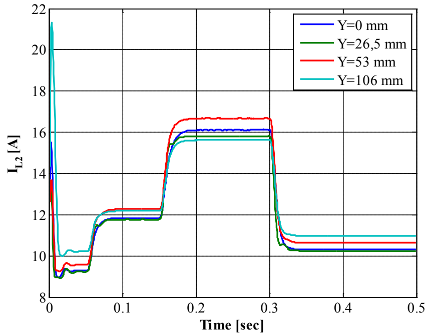

Fig. 4-47: Inductor current L2 case 4

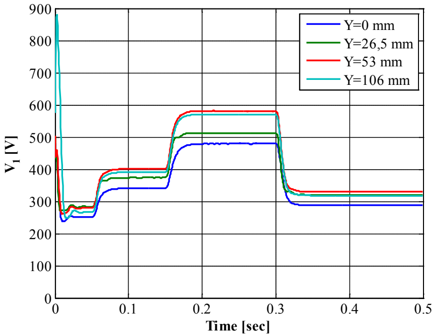

Fig. 4-48: Primary voltage case 4

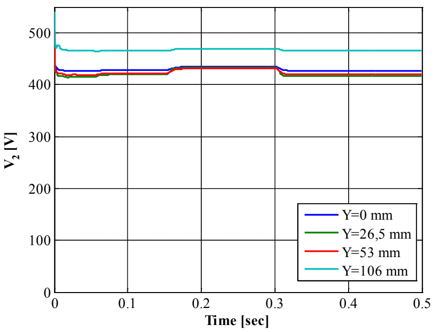

Fig. 4-49: Secondary voltage case 4

Observing the figures Fig. 4-34 -Fig. 4-49 , it can be pointed out that for different values of y misalignments the control system is able to follow the reference value, allowing a transfer power of about 9 kW. The behavior of the system to y misalignments it is in according to the FEM analysis reported in chapter 2 (Fig. 2-14).

4.7 References

[1] Dannier, A.; Ferraro, L.; Miceli, R.; Piegari, L.; Rizzo, R., "Numerical and experimental validation of a LiFePO4 battery model at steady state and transient operations, “in Ecological Vehicles and Renewable Energies (EVER), 2013 8th International Conference and Exhibition on, vol., no., pp.1-6, 27-30 March 2013

[2] Veneri, O.; Ferraro, L.; Capasso, C.; Iannuzzi, D., "Charging infrastructures for EV: Overview of technologies and issues, “in Electrical Systems for Aircraft, Railway and Ship Propulsion (ESARS), 2012, vol., no., pp.1-6, 16-18 Oct. 2012

[3] Veneri, O.; Capasso, C.; Ferraro, L.; Del Pizzo, A., "Performance analysis on a power architecture for EV ultra-fast charging stations, “in Clean Electrical Power (ICCEP), 2013 International Conference on, vol., no., pp.183-188, 11-13 June 2013

[4] C. Capasso, D. Iannuzzi, L. Ferraro, O. Veneri, “Experimental Study on a Laboratory Test Bench for Sea Wave Generation Systems”, Energy Procedia, Volume 61, 2014, Pages 1107-1110, ISSN 1876-6102, May 2014

[5] Tuning of PID Controller by Ziegler-Nichols Algorithm for Position Control of DC Motor

[6] The power electronics handbook – Chapter 2: DC-DC converters

[7] Sarac, Vasilija and Minovski, Dragan and Cogelja, Goran (2015) Computer aided design of simulation and experimental model of buck-boost converter. International Journal on Information Technologies & Security, 7 (1). pp. 25-32. ISSN 1313-8251

Chapter 5

Conclusion

During the last decades, public awareness of the environmental, economic and social consequences of using fossil fuels has considerably grown. Moreover, not only the supply of fossil resources is limited, but also the environmental impact represents a relevant issue, so leading to an increased consideration of clean and renewable alternatives to traditional technologies. During recent years, the automotive industry has shown a growing interest in electric and hybrid electric vehicles. However, the transition to all-electric transportation is now limited by the high cost of the vehicles, the limited range and the long recharging time. Distributed IPT systems can be the solution to the range restrictions of EVs by charging the vehicle while driving thanks to, a set of loosely coupled coils, so also reducing required battery size as well as overall cost of the vehicle.

The concept of wireless power transfer via magnetic induction was introduced two decades ago. Nowadays, this technology is becoming more efficient and more suitable for new applications. This dissertation made an effort to address the requirements of IPT EV battery charging system with high efficiency and good tolerance to misalignment.

A survey of a typical IPT for EV application has been reported, while a concentrated DD-BP solution has been proposed in order to enhance the IPT charging system capability of transferring power to a stationary EV with good efficiency and good tolerance to movement.

The current trend in EV battery charging application is represented by the lamped coil system, whose different structures have been reviewed.

On the contrary, this thesis presented the design of a charging pad magnetic structure, called Double D pad combined with a Bipolar secondary pad, in order to enhance coupling performance. A finite element magnetic analysis has been performed in order to obtain the electric parameters of the proposed magnetic coupler. Furthermore, a mathematical model has been developed by considering the different sides of the system. The mathematical model allows to accurately predict the behavior of inductive coils and coreless transformer. A set of simulation has been carried out in order to compare the analytical and simulated results.

The proposed EV IPT system has shown the feasibility of using fixed frequency, single pick up system to transfer power efficiently across a large air gap, with variable coupling. This result has been reached by means of proper design of the charging pad magnetics, of tuning network and of a pick-control based on a buck boost converter topology.

The research presented in this work was an attempt to address the problems related to the design and control of an IPT system, in order to achieve the power transfer with good efficiency, also having a wider tolerance to physical movement and changes in the coupling with respect to conventional loosely coupled systems.

The IPT system presented in this thesis are directly connected to voltage supplies. However, it could be possible to implement a system which allows to control the current generated into the primary coil by dynamically adapting the input voltage level, thus obtaining a real-time regulation of the transferred power.

The realization of laboratory prototype of the proposed IPT system will be useful to make a comparison between the experiments and analytical results.

The development of a lumped coil system to minimize the need for onboard storage and the battery depth of discharged allows to extend the stationary charge to dynamic charge. This latter can be obtained by installing the Double D pads along a highway. In this case, the coils can be selectively energized underneath an EV to couple the power, as required, in order to achieve a similar coupling performance of stationary lumped coil system both for vertical and lateral movement. The goal is to supply continuous power to a vehicle along the highway with a coupled uncompensated power as wide and smooth as possible.

Appendix A

6.1 Matlab Codes

6.1.1 AC side matlab code

```
clear all
clc
close all
format long
global  L1  L2  L3  M2  M3  C1  C2  C3  I1  w  R1  R2  R3  Mb  D
%% PROJECT  FREQUENCY
fo = 20000;
wo = fo*2*pi;
%% MODEL  PARAMETERS
k2  = 0.450;
k3  = 0.453;
R1  = 0.119;
R2  = 0.0745;
R3  = 0.0745;
L1  = 0.168e-3;
Leff = L1*(1-(k2^2)-(k3^2));
L2  = 0.365e-3;
L3  = 0.337e-3;
C1  = 1/(Leff*wo^2);
C2  = 1/(L2*wo^2);
C3  = 1/(L3*wo^2);
Ct= C2+C3;
% M21=M12=M2  M31=M13=M3  M23=M32=Mb
M2 = 0.112e-3;
M3 = 0.108e-3;
Mb = 25.47e-6;
% Rectifier
fri=pi/4;
frv=pi/2;
%% MODEL  IN  MATRIX  FORM
% states = I'l1  I"L1  I'l2  I"L2  I'l3  I"L3
% control u= I'l,  I'dc reported
% form  PX°=QX+RU
```

```
P=[ 1   0  0  0   0  0
   0  M3  0  Mb  R3  L3
   0   0  1  0   0  0
   0  M2  R2  L2  0  Mb
   0   0  0  0   1  0
  -R1  -L1  0 -M2  0 -M3] ;

Q=[ 0    1    0    0    0   0
   0    0 -1/Ct  0  -1/Ct  0
   0    0    0    1    0   0
   0    0 -1/Ct  0  -1/Ct  0
   0    0    0    0    0   1
   1/C1  0    0    0    0   0 ];

R=[ 0    0
   0 -1/Ct
   0    0
   0 -1/Ct
   0    0
   1/C1  0];

U=[ i1
   i'dc];
%% MODEL WRITTEN  IN THE FORM  X°=AX+BU   Y=CX+DU
A=inv(P)*Q;
B=inv(P)*R;
C=[ 1 0 0 0 0 0
   0 1 0 0 0 0
   0 0 1 0 0 0
   0 0 0 1 0 0
   0 0 0 0 1 0
   0 0 0 0 0 1 ];
D=zeros(6,2);
%%  CREATES  AN  OBJECT  SYS  REPRESENTING  THE  CONTINUOUS-TIME
STATE-SPACE  MODEL
SYS=ss(A,B,C,D);
% Convert state-space filter parameters to transfer function form
[n1,m1]=ss2tf(A,B,C,D,1);
[n2,m2]=ss2tf(A,B,C,D,2);
%% transfer function IL1  I1
f1=tf(SYS(1,1));
%% transfer function IL2  I1
```

```
f2=tf(SYS(3,1));
%% transfer function IL3 I1
f3=tf(SYS(5,1));
%% Plot the magnitude of frequency response for frequency between 18e3-24e3
% Hz
PP = bodeoptions;
PP.FreqUnits = 'Hz';
PP.Freqscale='linear';
w=(18000:0.5:24000)*2*pi;
figure (1)
bodemag(f1,w,PP)
grid on
title('Transfer Function IL1/I1')
figure (2)
bodemag(f2,w,PP)
grid on
title('Transfer Function IL2/I1')
figure (3)
bodemag(f3,w,PP)
grid on
title('Transfer Function IL3/I1')
```

6.1.2 DC side matlab code

```
clc
clear all
close all
format long
global L4 Lo Cdc Co Rb Eb d
%% MODEL PARAMETERS
L4=1e-3;
Cdc=4.1e-3;
Co=2.5e-3;
Lo=0.5e-4;
%% INPUT PARAMETERS
d=0.6;
Eb=360;
Rb=0.01;
IDC=5:0.2:30;
%% MODEL IN MATRIX FORM
% states Vdc Vco IL4 ILo
% control Idc Eb
% form PX°=QX+RU
```

```
P=[ Cdc 0  0  0
    0   Co 0  0
    0   0  L4  0
    0   0  0  Lo ];

Q=[ 0  0   d   0
    0  0 (1-d)  -1
    d (d-1) 0   0
    0  1    0   Rb];

R=[ 1  0
    0  0
    0  0
    0 -1  ];

U=[ Idc
    Eb ];
%% Model DC written in the form X°=AX+BU
A=inv(P)*Q;
B=inv(P)*R;
C=[ 1 0 0 0
    0 1 0 0
    0 0 1 0
    0 0 0 1];
D=zeros(4,2);
%%  Creates an object SYS  representing the continuos-time state space model
SYS=  ss(A,B,C,D);
% Convert state-space filter parameters to transfer function form
[n1,m1]=ss2tf(A,B,C,D,1);
[n2,m2]=ss2tf(A,B,C,D,2);
%% transfer function Vdc Idc
f1=tf(SYS(1,1));
%% transfer function Vo Idc
f2=tf(SYS(2,1));
%% transfer function IL4 Idc
f3=tf(SYS(3,1));
%% Plot the magnitude of frequency response
PP = bodeoptions;
PP.FreqUnits  = 'Hz';
PP.Freqscale='linear';
bode(f1,PP)
w=(1000:0.5:25000)*2*pi;
```

```
figure(1)
bodemag(f1,PP)
grid on
title('Transfer Function Vdc/Idc')
```

Appendix B

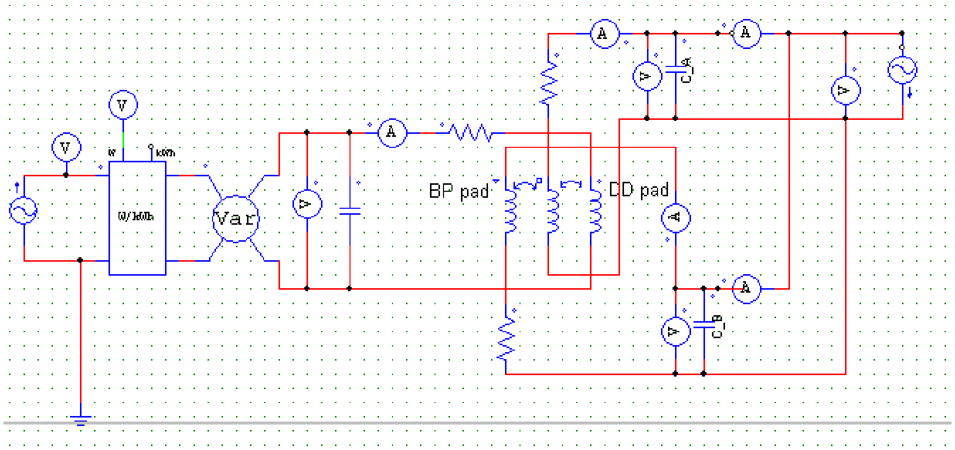

Fig. 7-1: Circuit of the AC side system

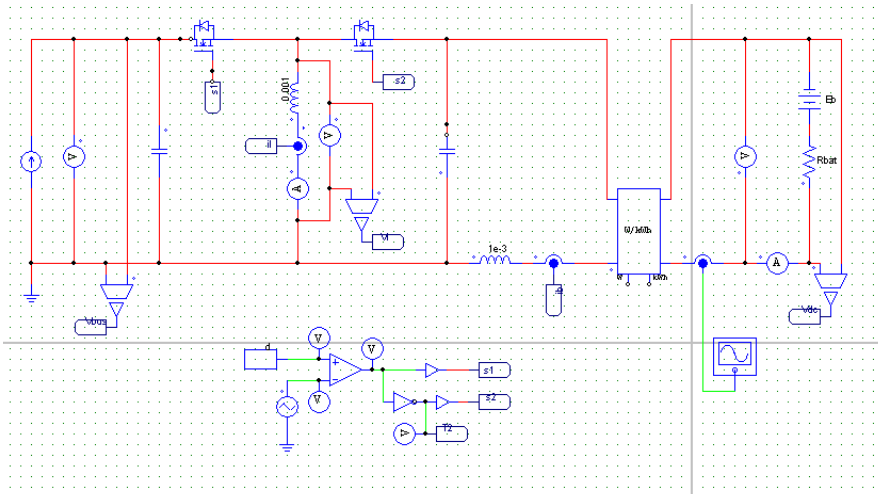

Fig. 7-2: Circuit of the DC side system

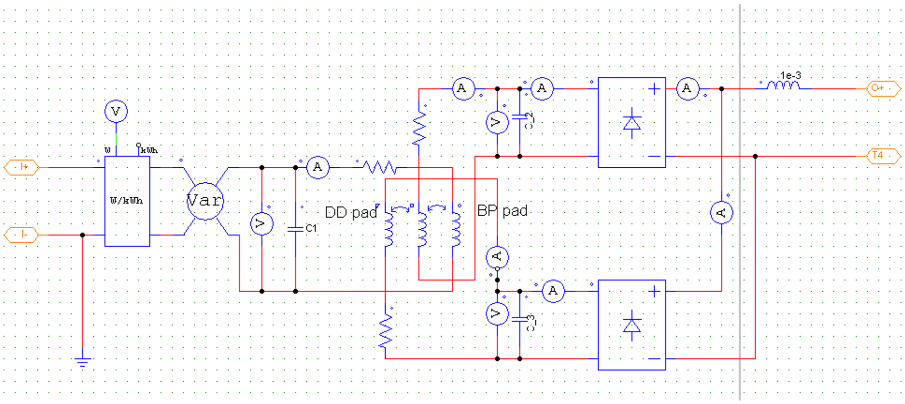

Fig. 7-3: PSIM Coupler circuit

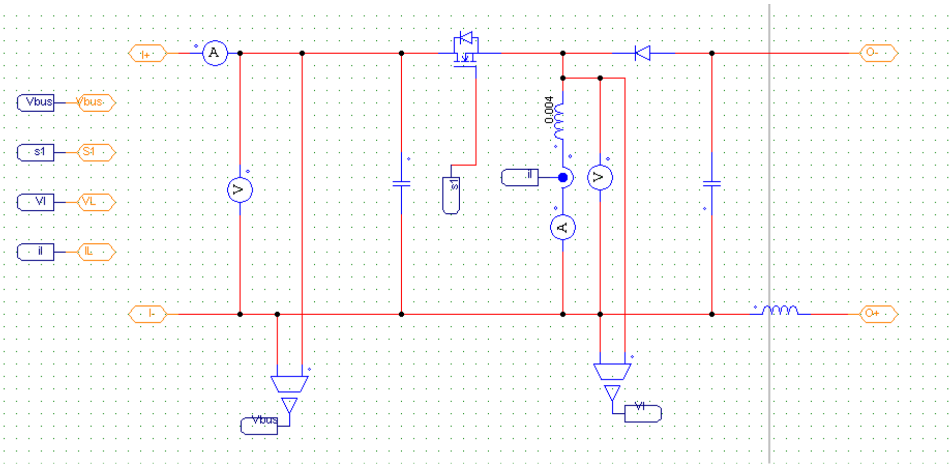

Fig. 7-4: PSIM Buck Boost circuit

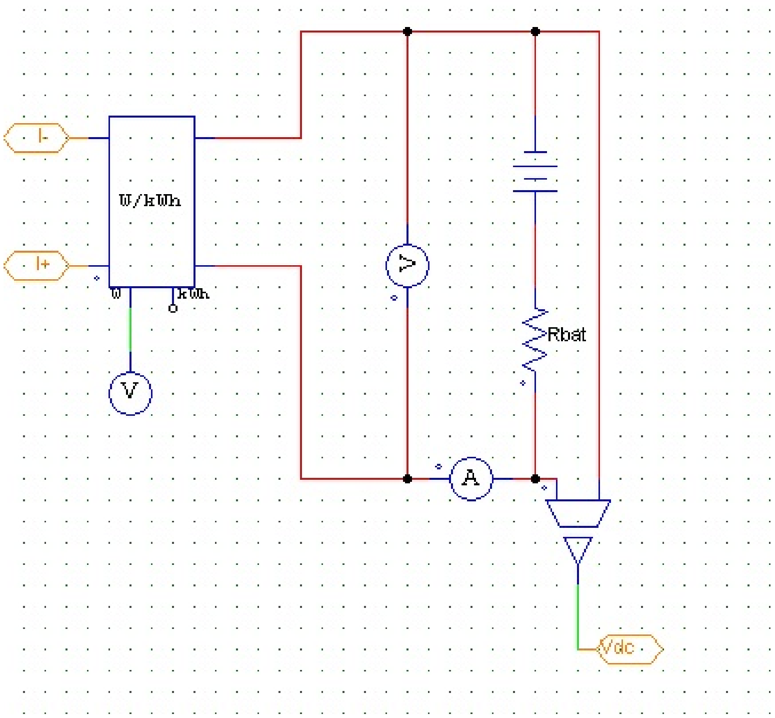

Fig. 7-5: PSIM Battery circuit

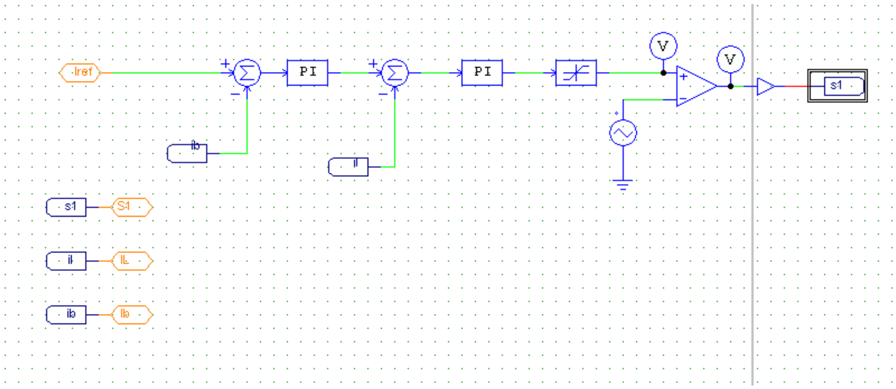

Fig. 7-6: PSIM Control circuit